TNO Physics and Electronics
Laboratory

TNO Defence Research

TNO-report	copy no.:	title:
EL-94-A094	8	Longterm Infrared Cloud Clutter Research

*Original contains color
plates: All DTIC reproduct-
ions will be in black and
white

19941214 061

DTIC QUALITY INSPECTED 1

DISCLAIMER NOTICE

TNO Defence Research

TD *94-0886*

Oude Waalsdorperweg 63
2597 AK The Hague
P.O. Box 96864
2509 JG The Hague
The Netherlands

Fax +31 70 328 09 61
Phone +31 70 326 42 21

DTIC
SELECTED
DEC 1 9 1994
F

TNO-report   copy no.:

FEL-94-A094   8

title:

Longterm Infrared Cloud Clutter Research

author(s):
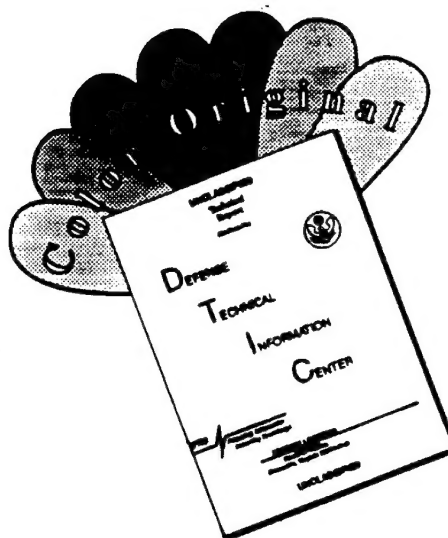
A.C. Kruseman

date:

October 1994

TDCK RAPPORTENCENTRALE
Frederikkazerne, gebouw 140
v/d Burchlaan 31   **MPC 16A**
TEL. : 070-3166394/6395
FAX. : (31) 070-3166202
Postbus 90701
2509 LS Den Haag

classification

classified by   : KLTZE H.R.E.V. van Westing

classification date : August 10, 1994

title   : Ongerubriceerd

managementuittreksel : Ongerubriceerd

abstract   : Ongerubriceerd

report text   : Ongerubriceerd

appendices A - D   : Ongerubriceerd

no. of copies   : 21

no. of pages   : 105 (incl. appendices,
                            excl. RDP & distribution list)

A-1

no. of appendices   : 4

All information which is classified according to Dutch regulations shall be treated
by the recipient in the same way as classified information of corresponding
value in his own country. No part of this information will be disclosed to any
party.
The classification designation Ongerubriceerd is equivalent to Unclassified.

"Original contains color
plates: All DTIC reproduct-
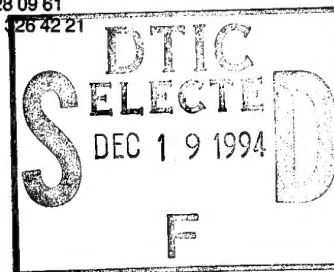ions will be in black and
white"

MANAGEMENTUITTREKSEL

titel   : Longterm Infrared Cloud Clutter Research
auteur(s)   : A.C. Kruseman
datum   : October 1994
opdrachtnr.   : A87KM174
IWP-nr.   : 766.1
rapportnr.   : FEL-94-A094

Sinds meerdere jaren heeft de Koninklijke Marine interesse in het onderwerp Infrared Search and Track (IRST). IRST systemen op schepen voorzien de commandant van een eerste waarschuwing tegen inkomende vijandige objecten. De nederlandse industrie heeft in de loop der jaren (1970-1993) gewerkt aan de IRSCAN rondzoeker, die gekoppeld aan Goalkeeper inkomende raketten kan uitschakelen. De industrie werd hierbij geassisteerd op verscheidene punten door TNO-FEL. Voor de toekomst staat SIRIUS op stapel, een IRST die een grotere detectie en track afstand moet halen dan IRSCAN, speciaal tegen supersone doelen.

In het algemeen moeten IRST systemen, waarvan IRSCAN en SIRIUS voorbeelden zijn, kleine puntdoelen kunnen detecteren op grote afstand. Dit probleem wordt gekenschetst door de straling van het doel, de atmosfeer, de achtergrond clutter en de sensor parameters. In dit rapport wordt vooral aandacht gegeven aan de achtergrond clutter. Deze achtergronden kunnen zijn lucht en wolken achtergronden. Door toevallige omstandigheden kunnen bepaalde aspecten van de wolken zich manifesteren als puntdoelen. Het is van groot belang om een adekwaat algoritme te ontwikkelen dat hier uitkomst biedt. Voor grotere detectie afstanden worden deze aspecten steeds belangrijker. Het aangeleverde rapport geeft inzicht in een aantal facetten, zoals elevatie afhankelijkheden, clutter metrieken, statistieken, en aspecten die samenhangen met wolkenhoogten, zoals deze van invloed kunnen zijn op de performance berekeningen. De resultaten uit dit rapport kunnen mogelijkerwijs worden gebruikt om bij IRST systemen de processing load te verlagen en de kans op valse tracks te verminderen.

Het onderzoek dat heeft geleid tot dit rapport is uitgevoerd met de TNO-FEL wolkenscanner Scorpio. Een overzicht van de werking van het systeem is gegeven in het rapport. De scanner heeft een veelheid aan all-sky beelden gegeven, die zijn gereduceerd ten behoeve van de clutter analyse.

Een grote database van beelden is opgebouwd, en een statistiek van deze beelden is gecreëerd. Vele verschillende situaties zijn bemeten. De atmosfeer is gemodeleerd met het programma LOWTRAN 7. Hierin is de radiantie bijdrage ten gevolge van een homogene wolkenlaag als parameter aanwezig, hetgeen de mogelijkheid openlaat om de wolkenhoogte te bepalen. Eveneens kan de bewolkingsgraad op bepaalde hemellocaties worden gemeten. Een clutter graad is in dit rapport gedefiniëerd die een objectieve maat vormt om de hoeveelheid clutter aan te geven die de IRST tegenkomt. Een optimalisatie van de clutter metriek geeft aan dat een locale methodiek de beste resultaten geeft. Naast de clutter metriek is ook de helling van de clutter curve van belang. Minimalisatie levert de beste resultaten als de locale berekeningen niet-lineair worden uitgevoerd (gemiddelde en een afgeleide van de variantie), om te voorkomen dat de randen van cellen teveel kunnen bijdragen. De eerste versie van de clutter metriek is met succes gebruikt in de referentie metingen tijdens de IRSCAN evaluatie metingen bij Fort Erfprins in 1991-1992. Eveneens bevat het rapport een samenvatting van de programmatuur die gebruikt is bij de analyse, alsmede de calibratie en mogelijke problemen van de wolkenscanner. Dit ten behoeve van eventueel gebruik en/of vereenvoudiging in de toekomst.

De conclusies zijn als volgt. Veel kennis op het gebied van wolkenclutter is vergaard. Een betrouwbare cluttermaat is gedefiniëerd, gebaseerd op locale statistieken en hellingen van deze statistieken. Er wordt aanbevolen om het onderzoek naar de verschillende clutter aspecten voortgang te laten vinden, zowel voor wolkenclutter bij lagere detectie drempels, clutter bij en onder de horizon, clutter ten gevolge van andere externe factoren als vogels en kustinvloeden.

1   INTRODUCTION

For the detection and tracking of point targets, Infrared Search and Track (IRST) systems have been developed by various companies in recent years. The point target detection process is hampered by the presence of cloud clutter. This cloud clutter may ultimately result in false alarms and should therefore be reduced in the processing. The performance of IRST systems should therefore at least be specified by the probability of detection in combination with the probability of detection probabilities at certain ranges and the accepted number of false threat declarations (i.e. false alarms). This limited behaviour is partly due to natural uncertainties, such as target signatures and background structure, and to technical functions as the limited amount of processing power. The performance of IRST systems should therefore be specified by the probability of detection in combination with probabilities of false threat declarations or false alarm rate.

The point target declaration process for the detection of incoming airborne targets is hampered by the presence of background clutter. This clutter can be cloud clutter or sunlit clouds for instance. The actual effects of cloud clutter depend on the objects present in the infrared scene, meteorological conditions, the target declaration system processing that is being used, etc. They therefore depend on the actual IRST system, hardware and software. For general background analysis, e.g. for comparing different processing methods and background scenes or scenarios, it is necessary to use a well defined objective clutter metric. With such a metric we are able to make a quantitative distinction between effects due to background structures and effects due to processing methods. In the case of statistical background analysis and for comparing the performance of detection systems (IRST, FLIR) such metrics have been developed in recent years (see Reynolds [1] and Schwering [2]). For the IRST processing background structures that are similar to a point target should be interpreted as clutter, hence clutter is of the size of the system's point spread function. Larger background structures may also be of interest for clutter rejection for instance by image segmentation or pattern recognition. With insufficient processing, cloud clutter may ultimately result in false alarms.

To obtain more information for the discrimination between targets and backgrounds the TNO-FEL cloud scanner was developed (figure 1.1). During our study with the cloud scanner we obtained nearly all-sky images at infrared wavelengths. Useful information of the sky's spatial clutter content and information for adaptive threshold setting is derived. A technical description of the cloud scanner is presented in chapter 2. Chapter 3 describes the measurements and data processing. LOW-TRAN is used in chapter 4 to predict infrared emission and propagation. The influence of the different parameters is also described in this chapter. During our measurements a large dataset of images is constructed. The analysis of this dataset for dependencies with meteorlogical data is presented in
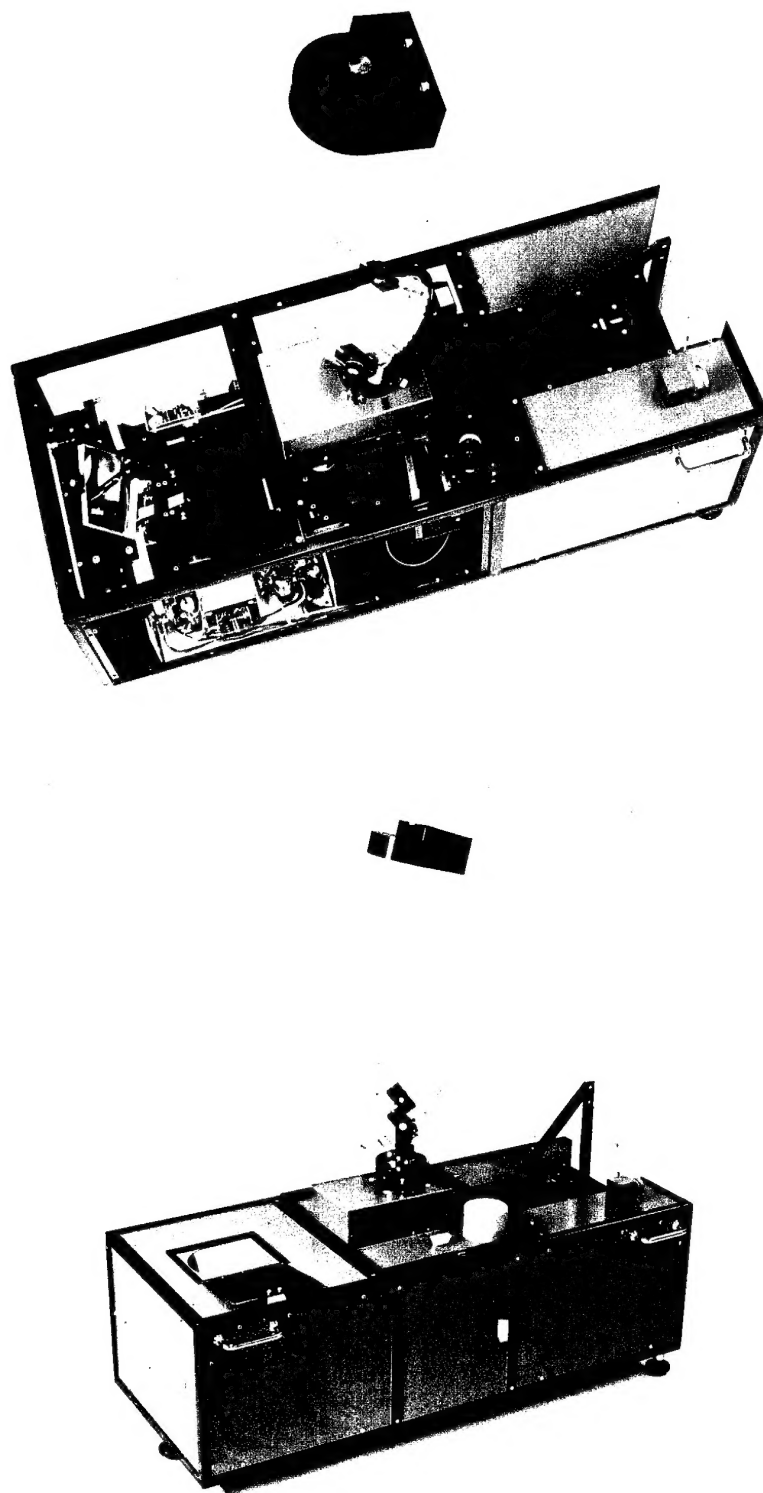
Figure 1.1:   The cloud scanner scorpio.

chapter 6. The conclusions are presented in chapter 7. This research program was performed under assignment A87KM174.

2   TECHNICAL DESCRIPTION OF THE CLOUD SCANNER

2.1   Scorpio Instrumentation

In order to study infrared clutter characteristics of cloud backgrounds TNO-FEL has constructed a device for calibrated acquisition of infrared sky and cloud data. The cloud scanner Scorpio was originally developed to have a large vertical Field-Of-Regard (FOR> 60°) and an IFOV between 0.5 and 1 mrad. Additional requirements were set by applicability in the infrared wavelength bands at 4 μm and 10 μm, possibility of exchange of detectors with the TNO-FEL DuDa scanner, a quick-look facility and a clamp calibration at each horizontal scan. A schematic overview of the Scorpio cloud scanner is presented in figure 2.1. In this section we describe the technical details of the system and discuss the electronic interface. A very detailed technical description can be found in Winkel [3].

Scorpio is a hemisphere line scanner with dimensions of 1_lx0.4_wx1_h m, and weighing 60 kg. The system operates (non-simultaneously) in the 3-5 μm and 8-13 μm infrared wavelength bands. The spectral sensitivity of the detectors is shown in figure 2.2. With the sensitivities of the detectors the radiance for a specific temperature can be calculated (figure 2.3). The band should be selected before use and can be set easily by a mirror switch at the front. The signal is transferred via a 5-mirror system to the chosen detector. The only collimating mirror of diameter 11 cm and focal length of 47 cm is placed in the main box of the system. Horizontal scanning is done by the central scan-mirror at 25 revolutions per second over an azimuth of 360 degrees. The system is calibrated during each revolution in an absolute way with the use of a temperature-controlled clamp-bar with a 20 degrees width. The vertical bar, which is filled with anti-freeze, is normally positioned to screen the solar radiation from entering the scanning system, and reduces the useful horizontal FOR to 340 degrees. A vertical scan is performed by the same scan-mirror in 80 seconds, covering an area from -18 degrees up to $+72$ degrees in elevation (1.125^o/sec). Hence instead of a perfect horizontal scan the lines are inclined by 0.785 mrad each, while the scan is spiraling upwards. The system makes use of reflective optics only, and can therefore be extended in the visual region of the spectrum. Synchronization pulses are created by a polychromal disk with 800 marks each revolution, together with line and frame synchronization pulses. The system produces two types of output. The most important one is the analogue data output, that is available via two channels (relative and absolute channel). In order to create a photographic picture, the beam of a built-in HeNe-laser is being modulated electronically by the signal from the infrared detectors. The analogue signals are used together with the synchronization pulses to create the images presented in this report.
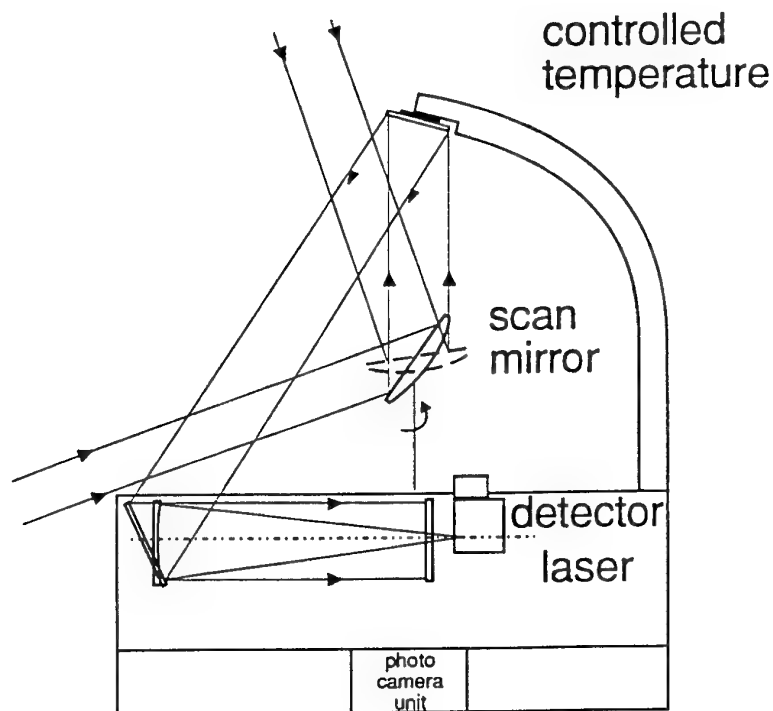
SCORPIO
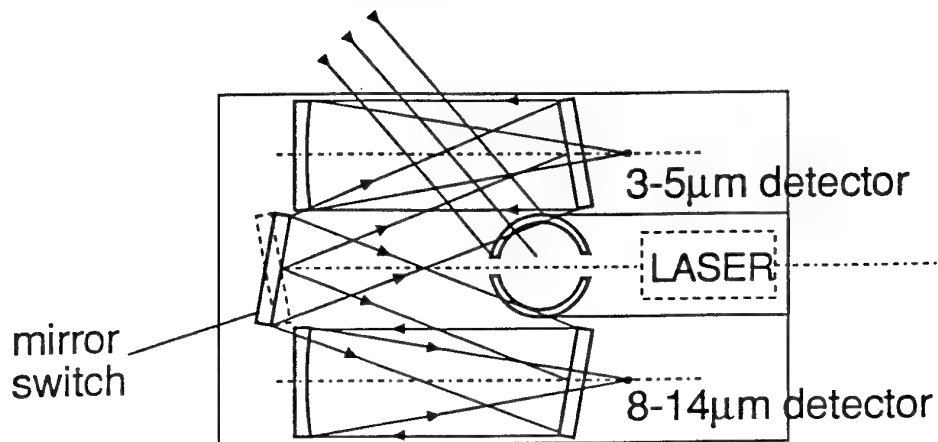

Figure 2.1:   Schematic overview of the TNO-FEL cloud scanner Scorpio.
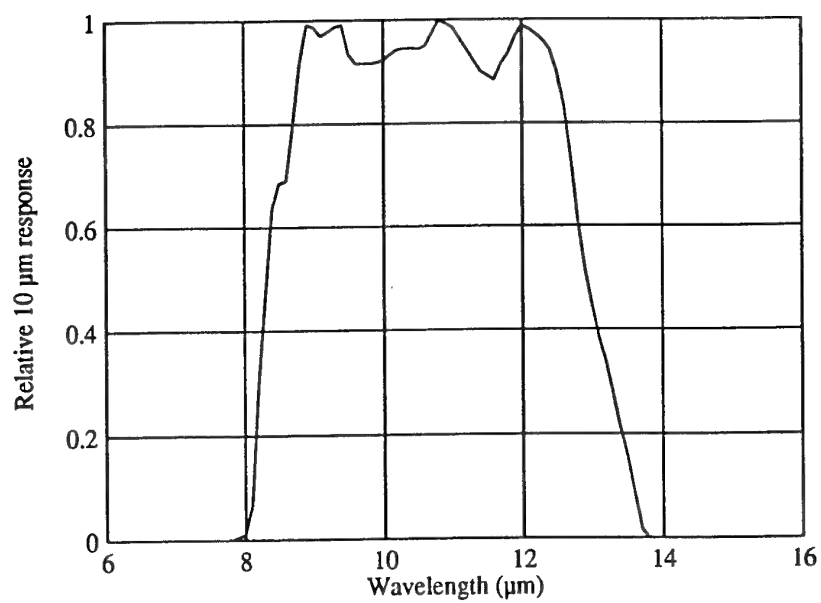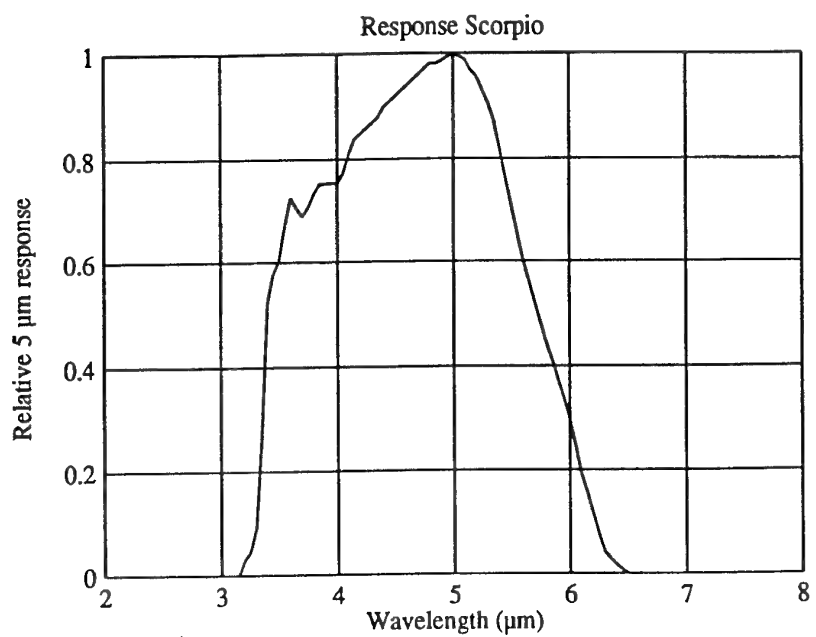
Figure 2.2:   The spectral sensitivity of the 4 μm and the 10 μm detectors.
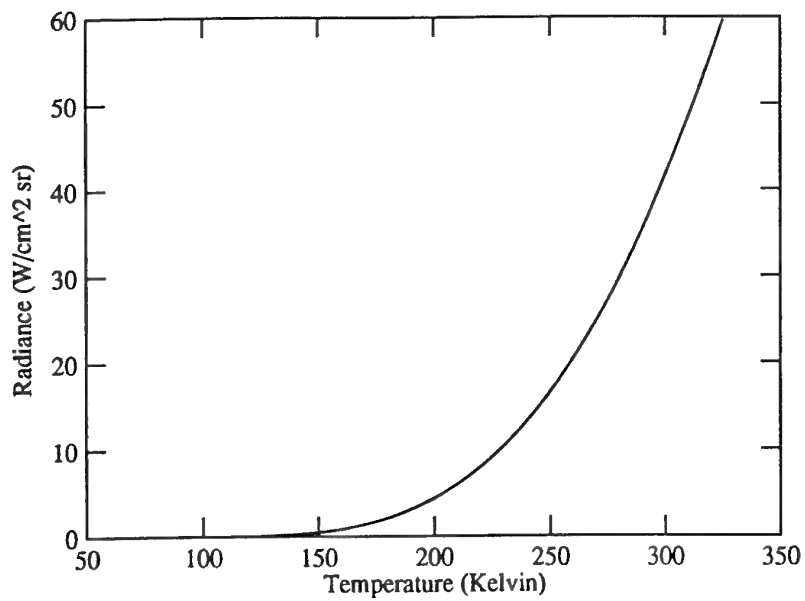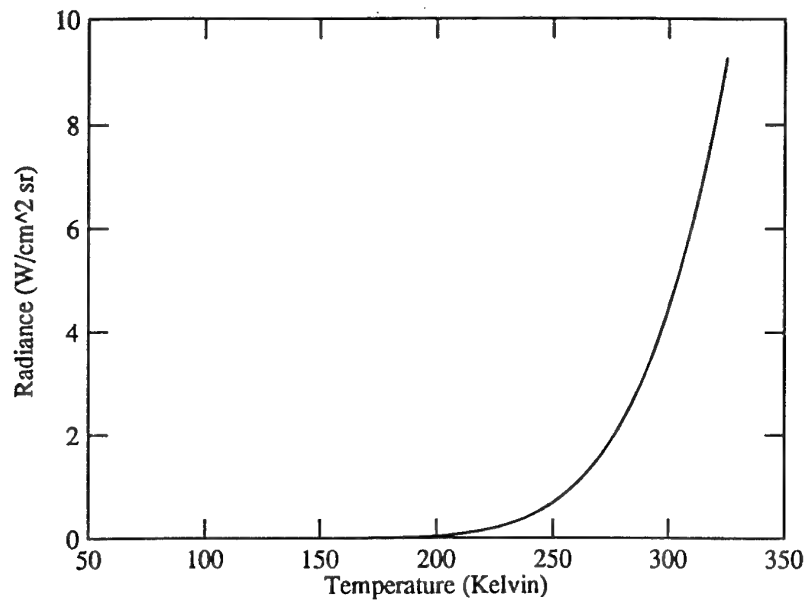
Figure 2.3:   The radiance as a function of the temperature for the 4 μm (top) and the 10 μm (bottom) detectors. Radiances values in $Wm^{-2}sr^{-1}$ refer to an apparant temperature as according to this figure.

2.2 Scorpio Calibration

The cloud scanner Scorpio is equipped with a temperature reference bar. An anti-freeze reservoir is connected with a pump to the bar. This system holds the bar at approximately the ambient temperature. A PT-100 platinum resistor measures the temperature of the reference bar. Via a clamp potentiometer the infrared signal is set to 'zero' (−0.5 Volt) when the mirror scans the reference bar. The system uses two sensitivities (absolute at 5 mV/°C and relative signal at 50 mV/°C). These gain sensitivities are calibrated at room temperature (290 K). The absolute signal is corrected for the ambient temperature and therefore has an absolute calibration. The dynamic range for the absolute calibration is from −100 to +300°C and for the relative calibration from $-10°C+T_{ambient}$ to $+30°C+T_{ambient}$. With the single element detectors the IFOV is 0.8 mrad (FWHM) and the NETD equals 0.06°C in the 10 μm band (CMT detector) and 0.2°C in the 4 μm band (InSb detector). The size of the liquid nitrogen cooled detectors is 0.1x0.1 mm.

The sensitivity calibration is performed three times in one year. Twice the sensitivity is determinated with the Electro Optical Indistries P41000 Differential Temperature Source and ones with two calibration sources developed at TNO-FEL. The Electro Optical Industries system has the advantage of a directly readable temperature display. Using the Electro Optical Industries system a difference of 5°C is created at an ambient temperature of 10.9°C. The response of the system is 0.05 ± 0.005 $Wm^{-2}sr^{-1}$ LSB. But this response has a temperature dependence. Appendix B describes the used method and the calibration measurements.

2.3 Scorpio data recording

Scorpio is placed on the roof of the TNO-FEL building, mounted on a manually rotatable platform. For long term use, it is installed in a weather-proof box, which can be opened only minutes before use, and where a heating systems avoids condensation. An interface is used to increase the number of synchronization pulses fourteen times, and to allow remote control of the photo-camera in Scorpio. It also displays the position of the mirror switch for the 4 μm or 10 μm channel, and buffers the analogue signal pulses. This interface is necessary for use of Scorpio with the computer ADC or the Airmec (quick-look) display. The connection between Scorpio and the interface box consists of a 40 m long 14-wire cable that was created especially for this instrument. The interface provides video, monitor and computer output with the voltage range needed for these devices. The computer output, range −1 V to +1 V, is also directly provided by the cloud scanner.

Scorpio is operated directly with a general-purpose computer. With a Masscomp 5500 Unix com-

puter equipped with a 12-bits ADC, images are created from the absolute calibrated analogue signal, which consist of 2000 lines in elevation of 5600 pixels on each line (16.8 MB of useful data). The analogue signal of Scorpio ranges from −1 to +1 Volt. The ADC input has a range from −5 to +5 Volt. The ADC has an internal gain control which can be set to 1, 2, 4 and 8 times. Generally the images are obtained using the low, absolute sensitivity with the gain of the ADC set to 8. Using these settings the images never exceed the range of the ADC (except for the sun). The other possibility is to use the high, relative sensitivity. The ADC gain is set at 4 times so the analogue signal is always between −5 and +5 Volt. But due to the effective dynamic range of 40°C with these settings, it can only be used in the summer. In the winter the difference between the apparent air temperature (at high elevations) and the ground temperature is too large and the analogue signal is clipped at −1 Volt by the cloud scanner.

We mainly used the 10 μm detector. The 4 μm detector signal contains noise of the motor which rotates the mirror. To check this we took a part of the sky with a uniform distribution. We made a FFT of this 512x512 images for both the 10 μm and the 4 μm. Figure 2.5 shows the amplitude of the FFT in the elevation direction. A sharp spike at 64 exists in the 4 μm FFT-image. This is caused by the motor which rotates the mirror. The motor uses a frequency of (25/8) Hz. The image can be corrected for this spike by smoothing the spike in the FFT and transform the image back. This gives some improvement but the image still consists of a lot of noise. Figure 2.6 is the amplitude of the FFT of a 10 μm image of the same part of the sky. In the 10 μm FFT there where no spikes caused by the motor and also fair less other spikes.

An off-line C-software package is created at TNO-FEL by mr. R.A.W. Kemp and by the author to analyze the images directly on the same computer system, in order to reduce the data. A description of the developed programs can be found in appendix C. Analysis takes place mainly on the Masscomp computer but the programs can also be used on other systems. Together with the computer software the system is an all-sky imager.

Cloud scanner
Scorpio

Manually
rotatable

Roof of TNO-FEL

Data cable

Masscomp 5500

Interface

Data &
frame, line and pixel puls
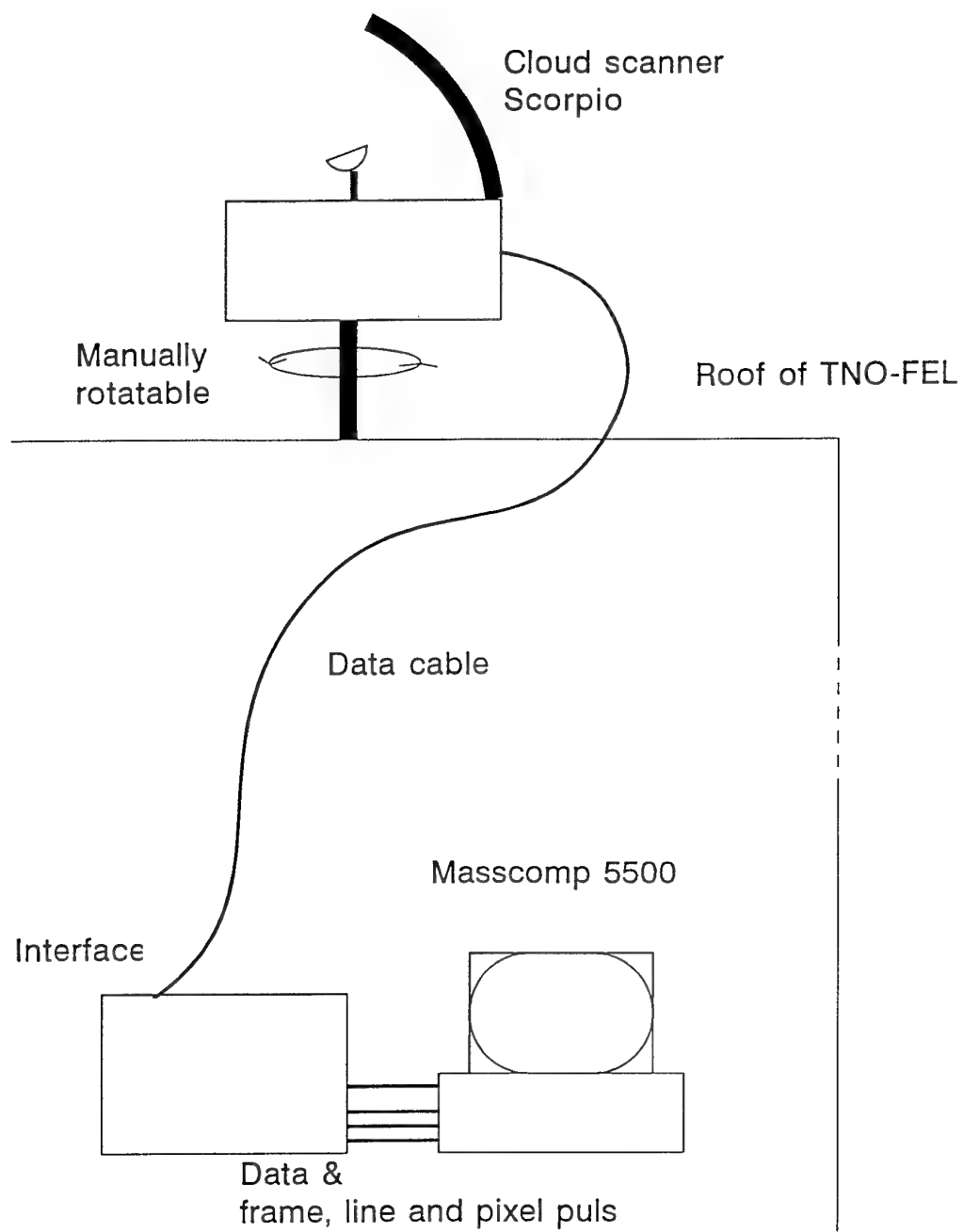
Figure 2.4:   Schematic overview of the TNO-FEL cloud scanner Scorpio setup.
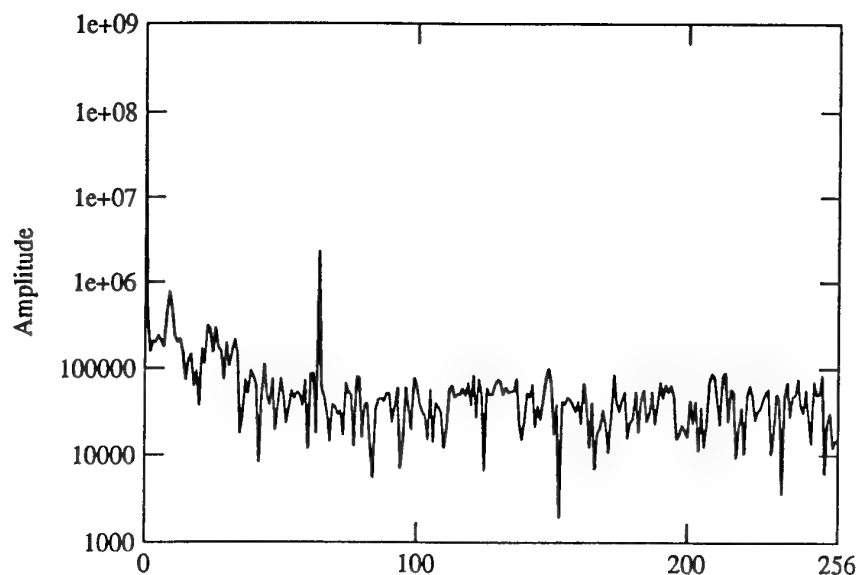
Figure 2.5:   The FFT of a 4 μm image (512x512 pixels), consisting of a part of the sky with no other objects on it. The amplitude of the FFT in the elevation direction is shown.
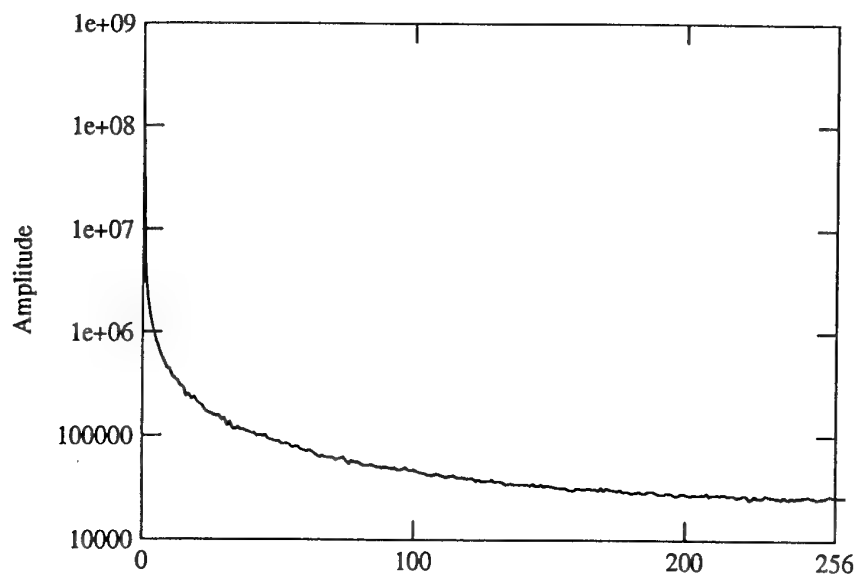
Figure 2.6:   The FFT of a 10 μm image (512x512 pixels), consisting of a part of the sky with no other objects on it. The amplitude of the FFT in the elevation direction is shown.

3   SCORPIO IMAGE PROCESSING

3.1   Image processing

The data that were used in this report were acquired using the Scorpio cloud scanner placed on
the roof ($\sim$15 m high) of the TNO-FEL building in The Hague (NL 52°06′41″N, 04°19′42″). The
lowest 18 degrees (below elevation 0°) of the images therefore show parts of buildings. All images
presented in this report have grey scales enhanced linearly to obtain a good quality figure, with
darker grey levels corresponding to warmer apparent temperatures. All images are recorded with
the 10 μm detector except when stated otherwise. Meteorological data were obtained from the
meteorological office of the Navy Airbase at Valkenburg (NL).

The images are normally displayed in two ways using polar or cartesian projections, with data
reduced 48 times to 500_vx467_h. Figure 3.1 shows an example of an image in this polar projection.
This image closely represents the geometric distribution on the sky, and directly shows the 360
degrees azimuth coverage. The projected image radius corresponds to elevation and the polar angle
corresponds to azimuth angle. The calibration reference bar is at the middle right of the image. The
gap in the centre of the image is the area with elevation beyond +72 degrees which is not covered by
Scorpio. Figure 3.2 shows the same image but represented in a cartesian projection. The elevation
is shown vertically and the azimuth angle is shown horizontally. In this representation it is easier
to see parts of the image that have the same elevation or azimuth angle. In this figure the reference
bar is at the left and right edges of the image.

For the study of infrared clutter and cloudiness we are only interested in the sky. It is therefore
necessary to blank the other parts of the image, such as the buildings and the reference bar. This
blanking is done by the computer program as the first step of the data processing of the image.
The blanking procedure consists of two blanking masks. One mask is used to blank the parts of
the mapper itself, such as the reference bar. The location of these objects in the image is fixed.
The second fixed shape mask is used to blank the buildings. Because the mapper is positioned on
a rotatable platform the position in an image differs for each different orientation of the mapper.
The computer program calculates the position for this mask and blanks that area of the image.
An example of the result of this blanking of the 10 μm image presented in figure 3.2 is shown in
figure 3.3.
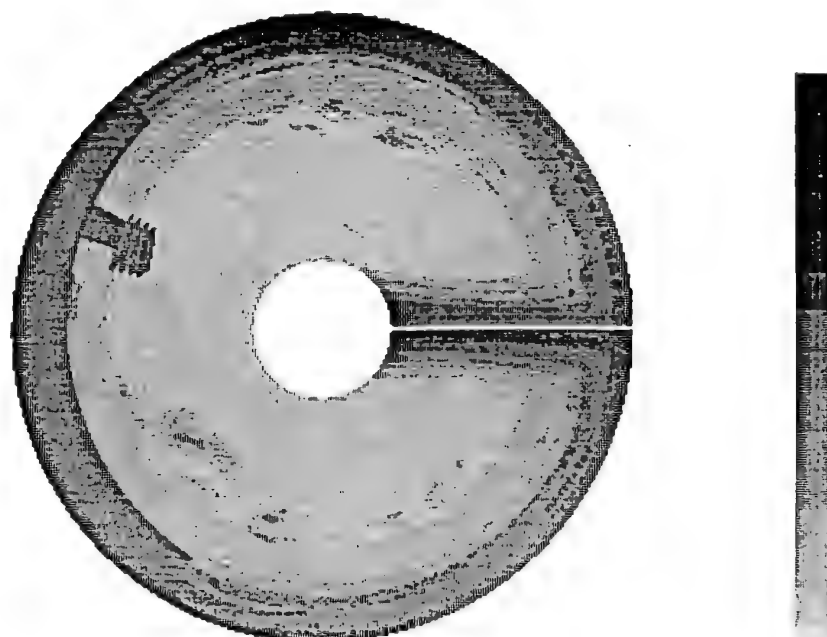
Figure 3.1:   Polar projection of a single 10 μm Scorpio image obtained at 3 March 1993 at 17:05 CET. Darker grey scales correspond to higher radiance values. The grey scale bar shows the used grey levels.

Figure 3.2:   The same image as in figure 3.1 using a cartesian projection.
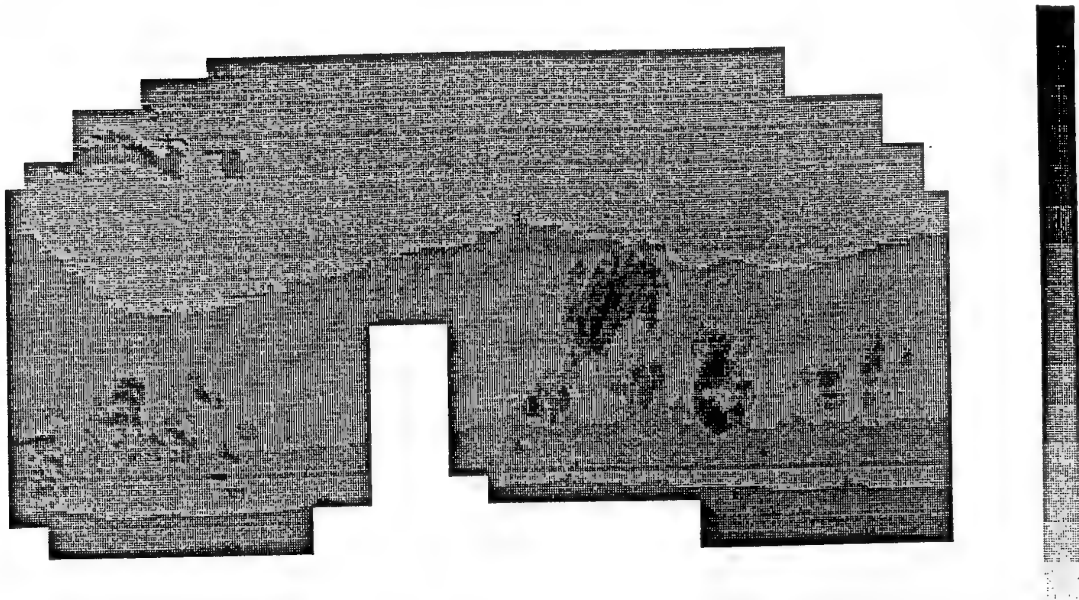
Figure 3.3: The image of figure 3.2 after blanking for removing non-sky parts (note that different grey levels are used compared to figure 3.2).
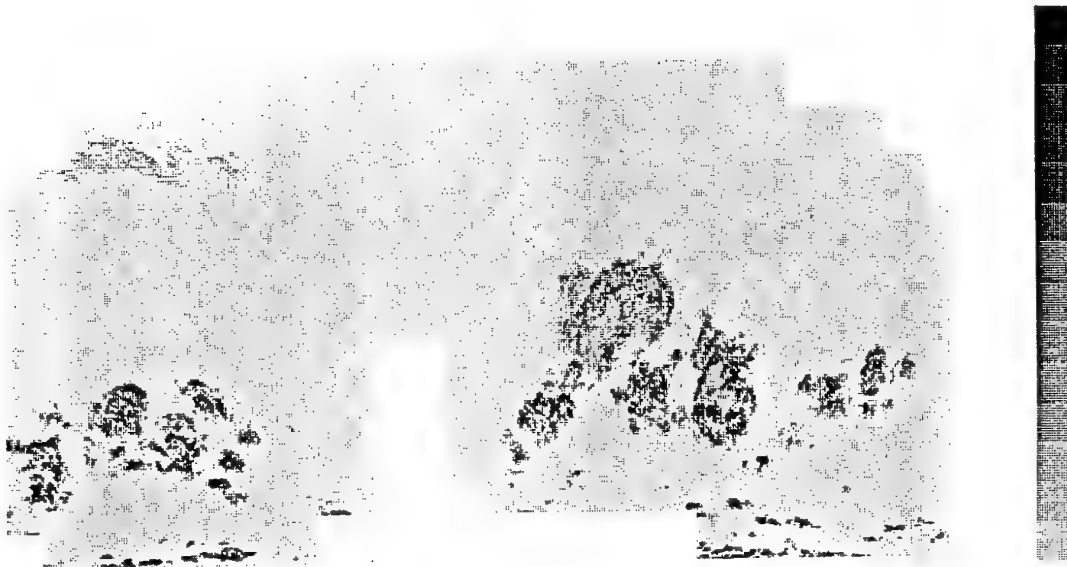
Figure 3.4: RMS cell calculations of the image of figure 3.3. White indicates low RMS values. Dark indicates high RMS values.

3.2 Clutter processing

Scorpio is build to study infrared clutter and cloudiness. A number of methods for describing clutter have been presented in the last years[1][2]. For cloud clutter calculations, RMS variations in image cells give good estimates of the amount of clutter, but only if the image noise is removed from homogeneous sky areas. We have followed a similar approach. The Scorpio images are divided in cells of nxm pixels. Based on fixed cells (and both summations over pixels in these fixed cells), the RMS value of each cell can be calculated from the average intensity in the cell μ_{static}, via:

$$\sqrt{\frac{1}{mn} \sum_{i=1,j=1}^{i \leq m, j \leq n} [I(i,j) - \mu_{static}]^2}$$

$$\mu_{static} = \frac{\sum_{i=1,j=1}^{i \leq m, j \leq n} I(i,j)}{mn}$$

We use a slightly different method now, namely calculating the average intensity for each pixel separately $\mu_{dynamic}$, in order to calculate the RMS variations (hence the RMS summation is still over pixels in the fixed cells):

$$\sqrt{\frac{1}{mn} \sum_{i=1,j=1}^{i \leq m, j \leq n} [I(i,j) - \mu(i,j)_{dynamic}]^2}$$

$$\mu(i,j)_{dynamic} = \frac{\sum_{l=-m/2,k=-n/2}^{l < m/2, k < n/2} I(i+l, j+k)}{mn}$$

Instead of using the average of the cell in the RMS calculation, we apply the average of an area with the dimensions of the cell centred at the concerning pixel (x, y). We need to do a lot more computations to obtain all averages, but the result is clearly improved. In an area with little variance the two methods give nearly identical results, but in a structured area (cloud edges, objects) there is a significant difference.

To show the difference in both calculation methodes we use a partly clouded area (figure 3.5) of the full resolution image that was the basis of figure 3.2. In figure 3.6 we show images of the absolute difference between radiance values and the average μ, $|I(x, y) - \mu|$, in the same cloudy area, based on μ_{static} and based on $\mu_{dynamic}$. The cell dimensions that we use are $4_v \times 12_h$. The figures show that large differences between the averages μ_{static} and $\mu_{dynamic}$ are located near the edges of the cell (as might be expected). The greatest difference occurs both in the vertical and horizontal directions. The figure based on $\mu_{dynamic}$ shows a more natural distribution. This difference between these methods

is caused by using the average μ_{static} which is not a good representation of the true average of the surrounding area for a pixel at the edge of the cell. The RMS distribution graphs based on cells of 4x12, shows that there is a significant decrease in high RMS values in the case of a dynamic average, hence together with a noise threshold leading to a lower clutter measure. In figure 3.8 and 3.7 we present the distribution graphs of the difference from the average values of both μ_{static} and $\mu_{dynamic}$ for two different cell sizes (4x6 and 4x12). The smaller cell was chosen to show the effect of a smaller cell on the tail of the distribution. We note the difference between the two distributions for both cell sizes (figure 3.7 and 3.8). The smaller cell dimension results in a lower amount of high clutter values for both curves, but no great relative changes. Therefore the difference between calculations based on μ_{static} and $\mu_{dynamic}$ is certainly not dominated by the cell size. Hence it is clear that at the cost of computing effort (proportional to the cell size), less high clutter values, and a lower clutter measure can be obtained from the $\mu_{dynamic}$ calculations. Although the equations describe the standard deviation we will use "RMS" to indicate this operation. All references in this report to "RMS" are based on the $\mu_{dynamic}$. Figure 3.4 shows the distribution of the RMS clutter values, based on $\mu_{dynamic}$, for the entire Scorpio image that was presented in figure 3.2. Note the enhancement of cloud edges with respect to the cloud foreground and sky background.
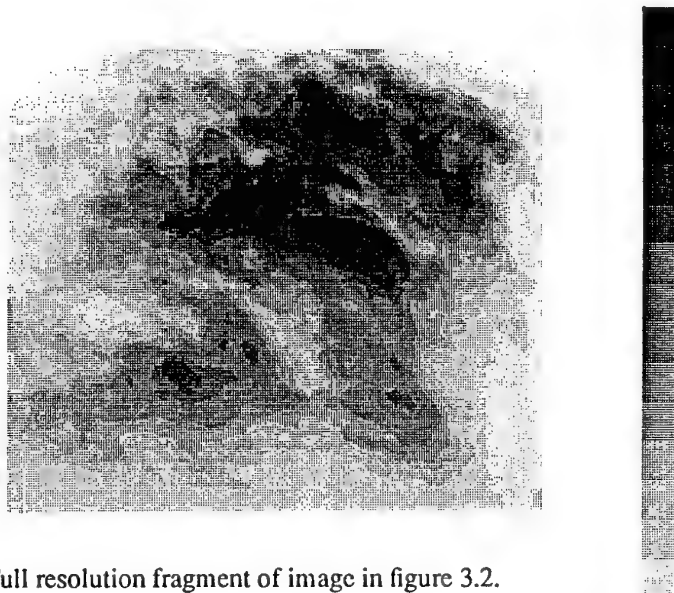
Figure 3.5:   Full resolution fragment of image in figure 3.2.

These RMS variations generally consist of a gaussian distribution caused by the noise of the scanner and detector system and a tail caused by clutter. Simple detection algorithms use an adaptive threshold to detect targets. The tail of the distribution is the interesting part with respect to clutter hampering detections. To show this high clutter area of interest all RMS distribution are shown
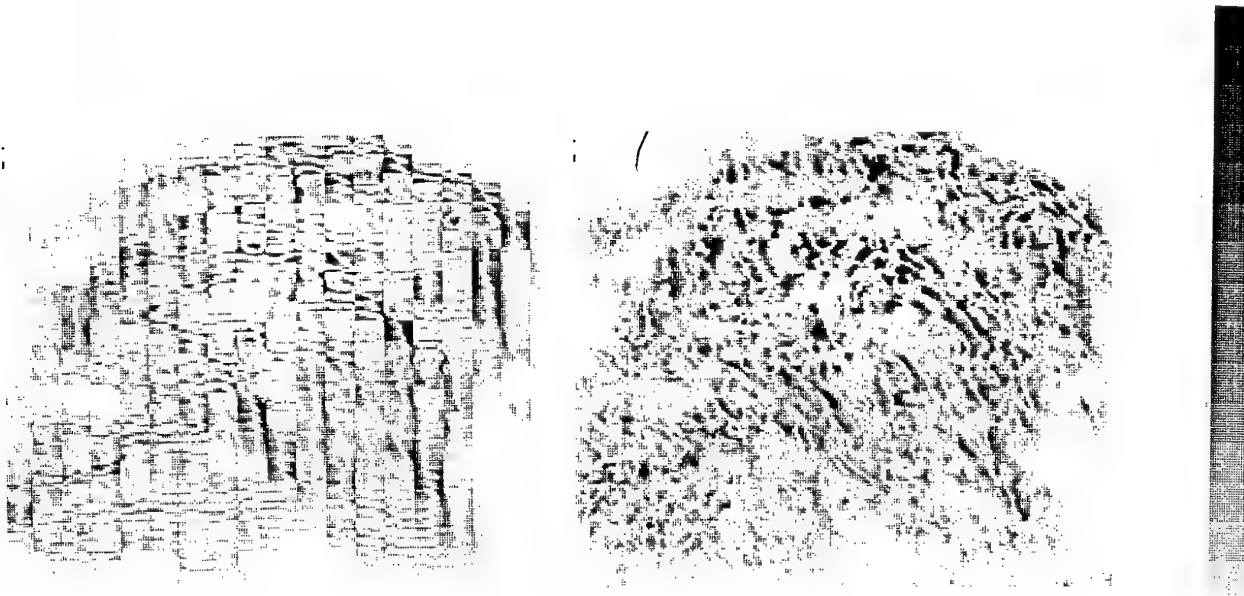
Figure 3.6: The absolute pixel differences from the average ($|(x, y) - \mu|$) based on μ_{static} (left) and based on $\mu_{dynamic}$ (right).
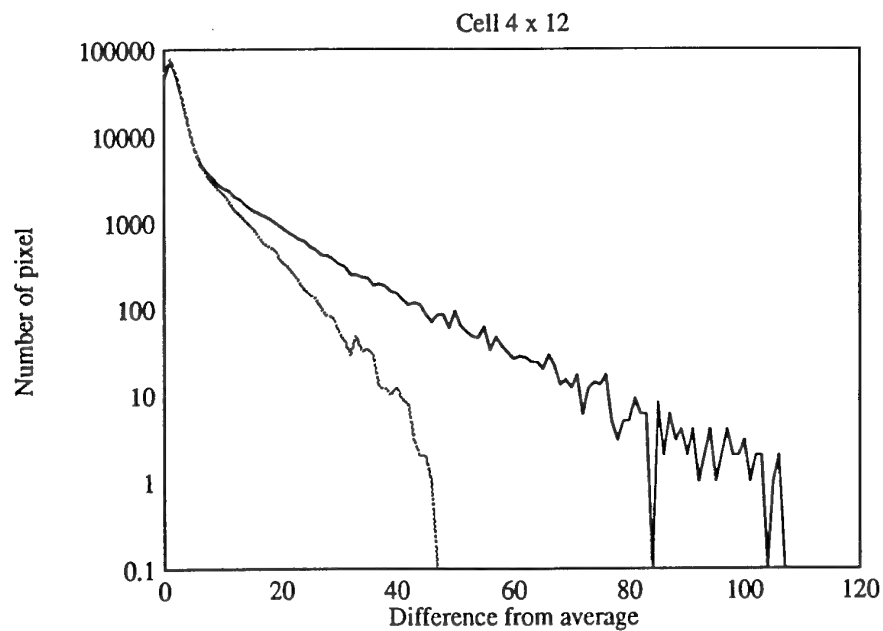
Figure 3.7: The distribution of ($|I(x, y) - \mu|$) for a 4x12 cell. Solid using μ_{static} and dotted $\mu_{dynamic}$.

Cell 4 x 6
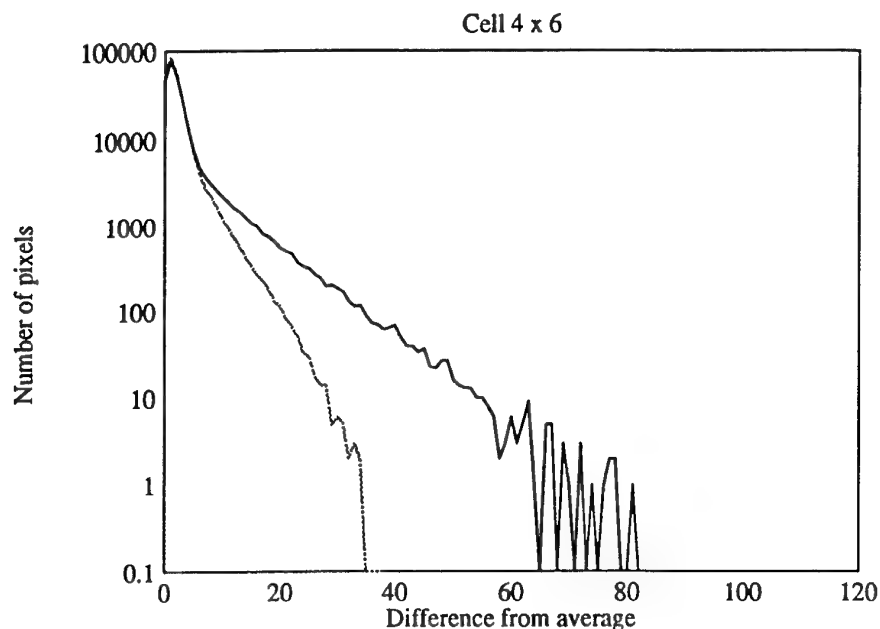
Figure 3.8:   The distribution of $(|I(x,y) - \mu|)$ for a 4x6 cell. Solid using μ_{static} and dotted $\mu_{dynamic}$.

in logarithmic graphs. A point target has an irradiance independent of the surrounding image. By using μ_{static} the clutter in non-uniform areas is over estimated at the edges of the cell. A longer tail may result in more false detections at the same threshold value, and a higher processing load, and possibly a higher false alarm rate. In the case of adaptive thresholds however, these will be raised and the detection probability of targets will be diminished. Also the clutter values become dependent of the position of a cell. We therefore conclude that the use of $\mu_{dynamic}$ should be preferred. Operationally the choice of $\mu_{dynamic}$ may lower the adaptive treshold settings in IRSTs and hence improve the processing sensitivity.

3.3   Elevation dependent analysis

We study dependencies of clutter with elevation angle. We therefore calculated the distribution of sky and cloud radiance and of clutter values in blocks of 0.9° of elevation. This results in 2-dimensional histograms which are presented in figure 3.9 for an image recorded on 3 March 1993. The distribution of sky radiance with elevation shows in general a smooth empty sky curve together with some pixels containing clouds. The RMS clutter contour/greyscale-plot values show high values only for the cloudy areas. The values are normalized to the area of the unblanked elevation block and the contours are spaced on a logarithmic scale (figure 3.10). In figure 3.11 the RMS
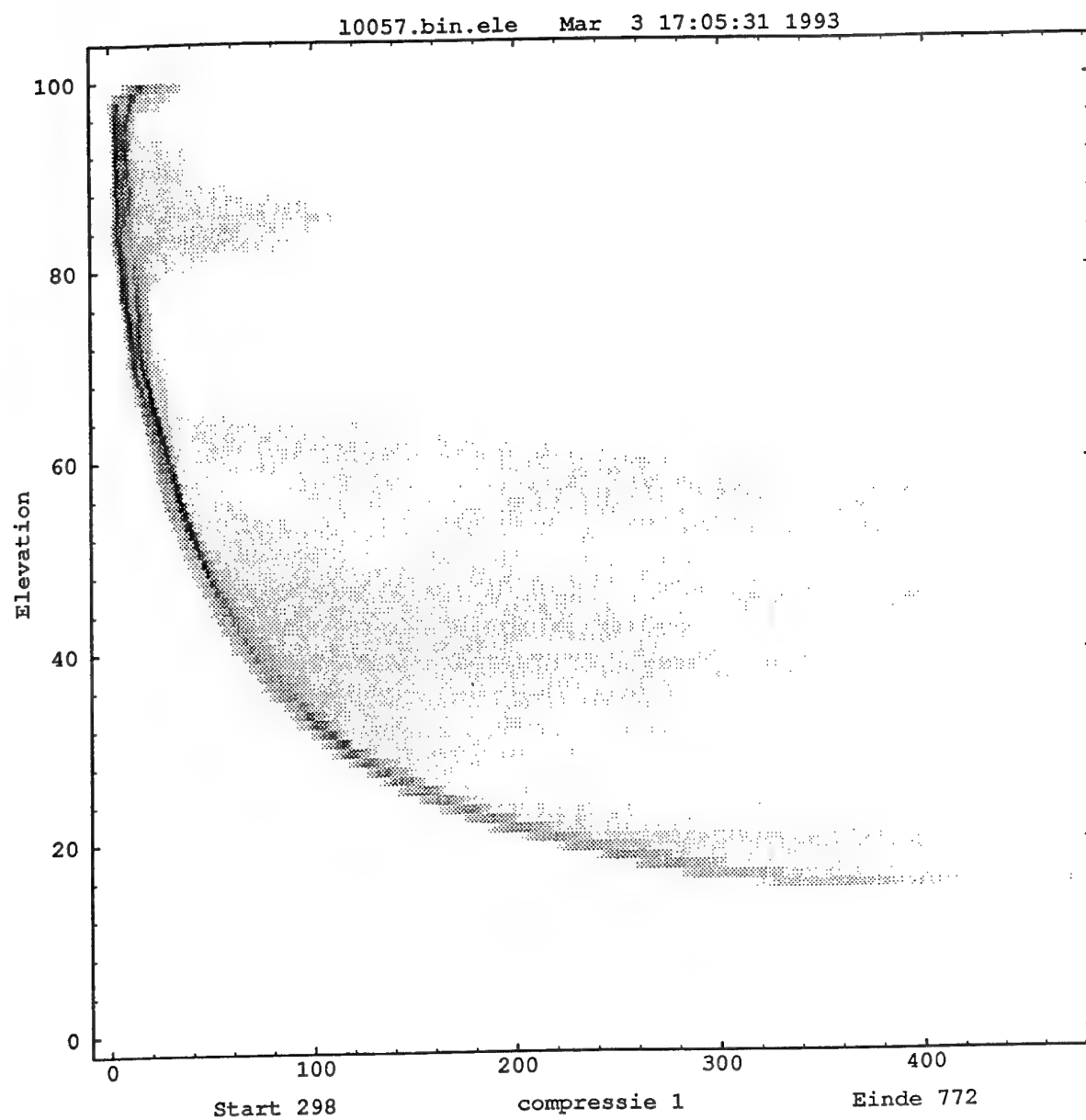
Figure 3.9:   Radiance distribution with elevation. Darker grey scales are higher occurrences. The radiance is in units of 0.053 $Wm^{-2}sr^{-1}$ and a offset of 4 $Wm^{-2}sr^{-1}$. The elevation is in $(y - units/100) * 90° - 18°$
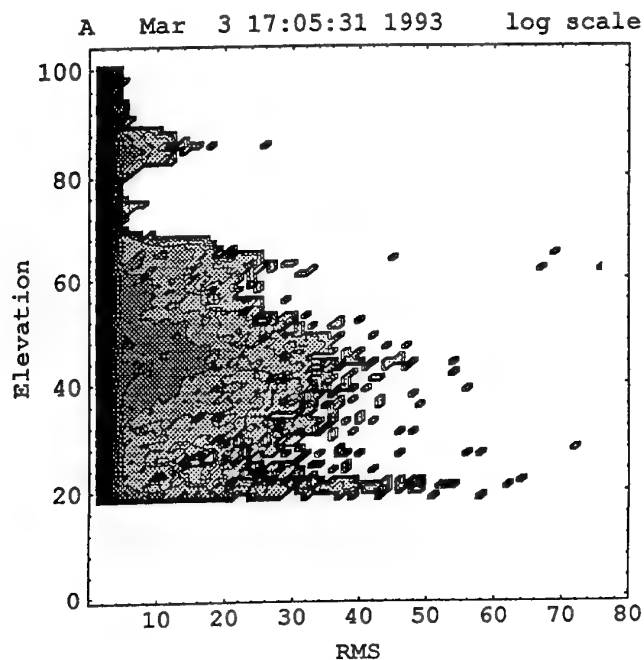
Figure 3.10:   Contour plot of the RMS distribution with elevation. The contours are logarith-
mically spaced. The horizontal units are 0.027 $Wm^{-2}sr^{-1}$. The black edge at
the left is caused by the system noise. The centre of the distribution (RMS>5) is
caused by clouds.
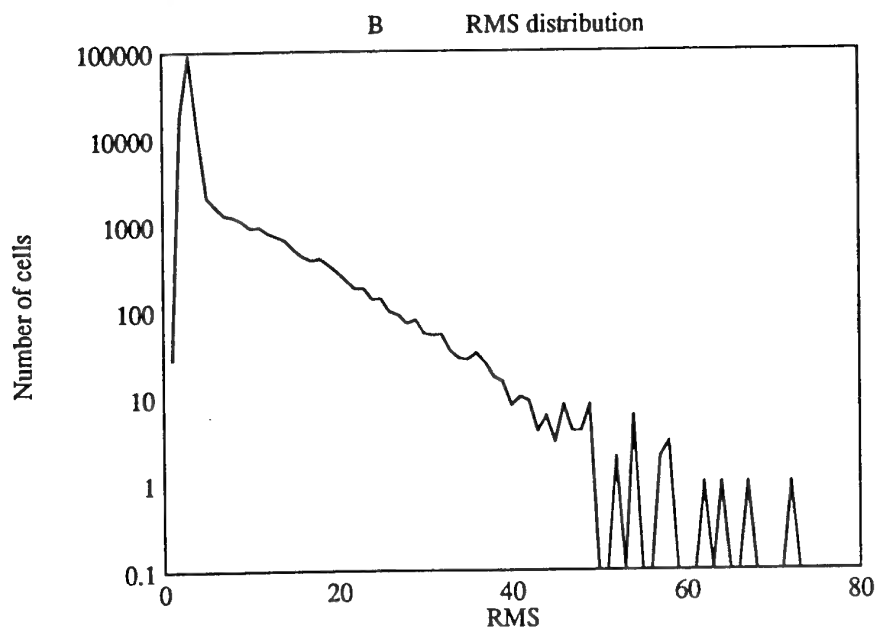
Figure 3.11:   The RMS distribution of the entire blanked images. The horizontal units are 0.027
$Wm^{-2}sr^{-1}$.
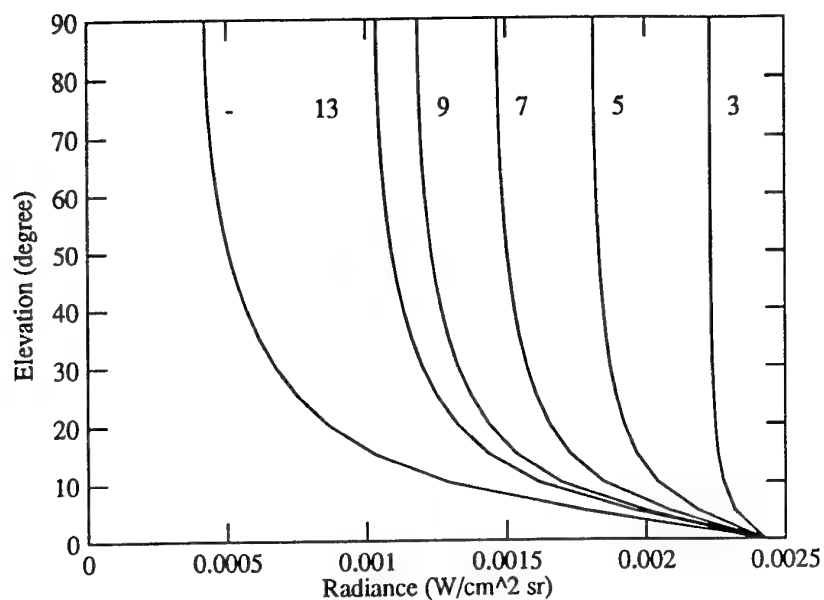
Figure 3.12:   Lowtran curves of open sky (-) and with clouds at 3, 5, 7, 9 and 13 km.

distribution of the entire image in cells of 4x12 and using $\mu_{dynamic}$. Lowtran7 calculations for the global atmospheric conditions at the time of the observations. These calculations were performed with a sky background and with cloud layers at respectively 3, 5, 7, 9 and 13 km height (figure 3.12). The empty sky Lowtran7 radiance curve corresponds well with the observed main curve.

4 LOWTRAN7 RADIANCE CALCULATIONS

4.1 Introduction

LOWTRAN7 is a Fortran code program used to predict optical/infrared propagation and emission in the atmosphere at low resolutions ($20 \, \text{cm}^{-1}$). Input parameters for this model are meteorological conditions. We use the LOWTRAN7 code to predict the radiance with elevation. The lowtran model exists of 34 layers maximum. Atmospheric layer data can be obtained from a balloon or an aircraft. In our study with the cloud scanner we do not have the possibility to obtain these data. We have chosen to use ground level meteorogical data, as this corresponds closest to operational circumstances. We do have meteorological data at ground level. A model of the atmosphere can be made based on these ground level data. For this model it is necessary to know the relevant meteorological parameters. This model can also be used to compute the influence of clouds.

As basis model we use a path to space from 10 m with the midlatitude winter model in the range of 770 to $1200 \, \text{cm}^{-1}$ (see lowtran table 4.1). We vary the zenith angle to get a distribution of radiance with elevation.

```
 3    3    1    1    0    0    0    0    0    0    0    1    0 0.000 0.00
 1    0    1    5    0    0  10.000    4.000    4.000    0.000
   0.010    0.000   90.000    0.000    0.000    0.000    0
 770.000 1200.000   10.000
 0
```

Table 4.1: Basis TAPE5 lowtran input file data. If no values are given in the text these values are used.

Lowtran can operate using single or multiple scattering. The difference in calculated radiance is up to $0.25 \, \text{Wm}^{-2}\text{sr}^{-1}$ between multiple and single scattering (see figure 4.1). MODTRAN, a moderate resolution model ($2 \, \text{cm}^{-1}$), is also available for calculations. The difference between LOWTRAN and MODTRAN is small at low elevation and in the order of $0.05 \, \text{Wm}^{-2}\text{sr}^{-1}$ at high elevation. The disadvantage of modtran is that it takes ten times longer when using the same TAPE5 input file. For all the following computations we use lowtran in the multiple scattering mode.

4.2 Simulation of cloud layers

Three ways to simulate the radiance with elevation for a full cloud layer at a specific height are:
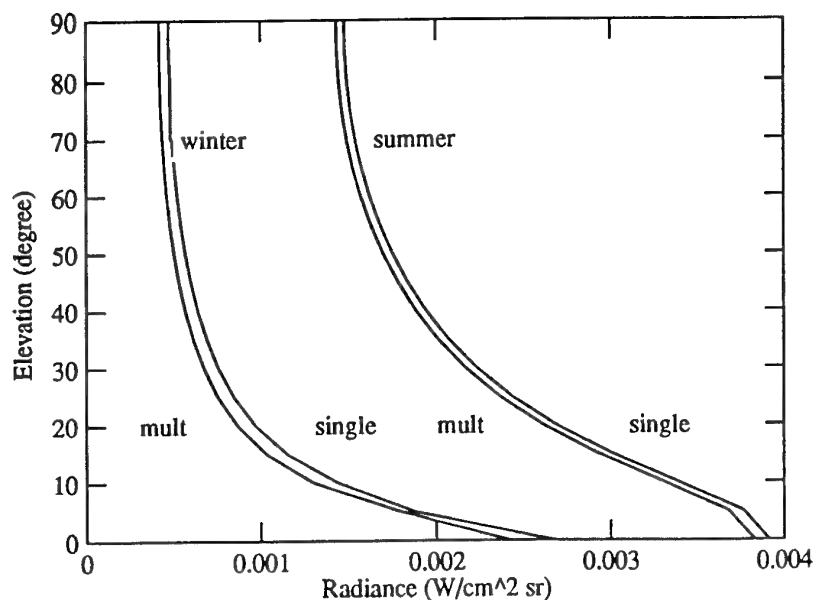
Figure 4.1:   Radiance distribution with elevation using the midlatitude summer and winter model. From left to right winter (multiple scattering, single scattering), summer (multiple scattering, single scattering).
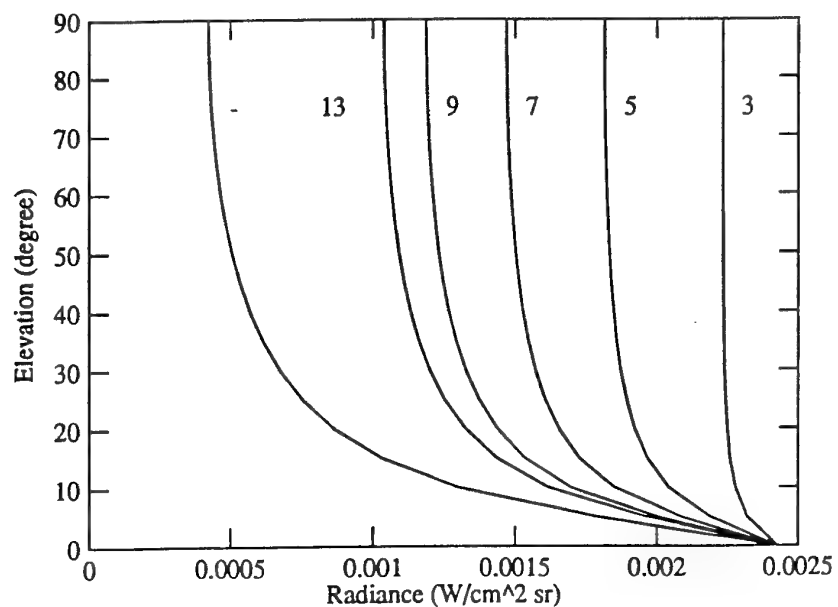
Figure 4.2:   Midlatitude winter lowtran calculations for cloud levels at different heights (3, 5, 7, 9, 13 km) and empty sky (–).
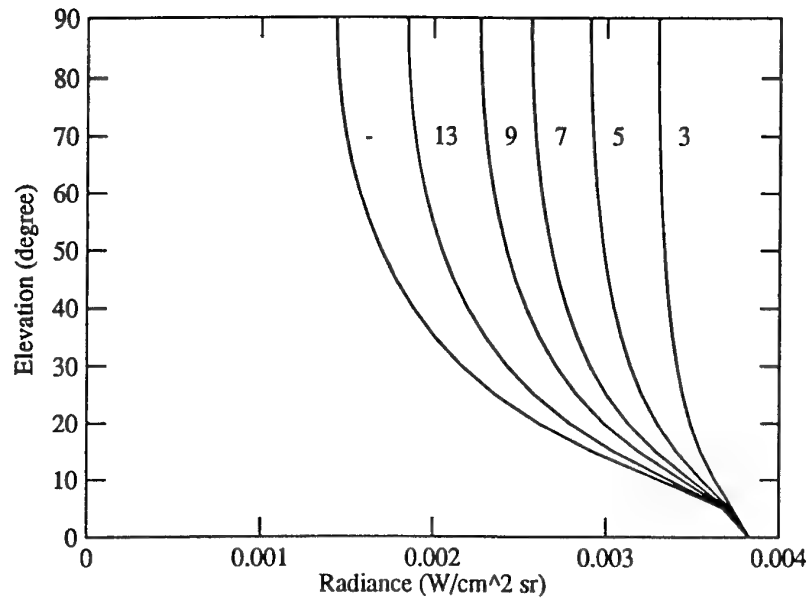
Figure 4.3:   Midlatitude summer lowtran calculations for cloud levels at different heights (3, 5, 7, 9, 13 km) and empty sky (−).
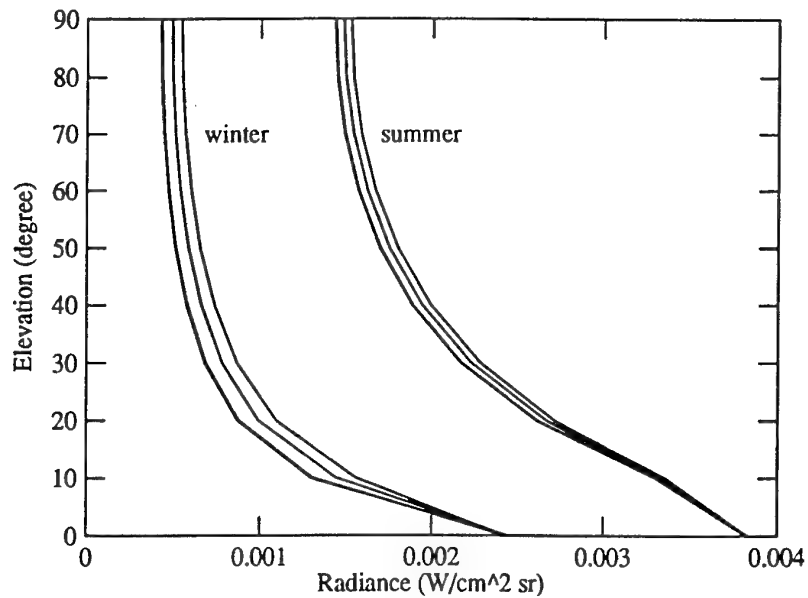
Figure 4.4:   Midlatitude winter and summer lowtran calculations for cirrus cloud models. From left to right: open sky, model 19, 18, 20 (card2 ICLD).

1. Compute a slant path to the cloud height using the cloud as a black body with the temperature of the layer.

2. Read a new layer model and set the RH to 100 % at the cloud level, the equivalent liquid water content to a value > 10 and set IHA1 of card 2C3 to a fog type. Each entry in the TAPE5 file should contain the profile. The LOWTRAN option IM=1 of card 1 should not be used. This profile should be rered for every elevation!

3. Using the cloud models of lowtran.

The last methode has the disadvantage that only 8 cloud models exists. Five low level cloud models and three cirrus cloud models. For comparing real radiance profiles with predictions only method 1 and 2 are usable. Method 1 is easier to use than method 2 because for this last method an atmospheric profile is necessary. The resulting radiance curves have a deviation of each other in de order of 1.5 $Wm^{-2}sr^{-1}$. Method 1 is used to calculate the following curves. Figure 4.2 gives the radiance curves in a midlatitude winter and figure 4.3 the curves in a midlatitude summer. The values of cloud levels above 7 km are not realistic at 52°N latitude. These are only shown to give an impression of how the curves would be. Clouds above 7 km are cirrus clouds. The physics of these clouds concerning scattering and transmission is different of lower level clouds. LOWTRAN7 has 3 special models for cirrus clouds (card 2 ICLD 18, 19, 20). Using card 2A the cloud height and thickness can be set. Figure 4.4 shows the three default curves. The radiance curves of cirrus clouds are almost identical to the open sky curve. This is in accordance with the measurements.

4.3   Variation of lowtran parameters

It is important to know which parameters are relevant for the radiance distribution. As basis model we use the midlatitude winter model (table 4.1). In figure 4.5 the visibility is varied to 5, 10 and 25 km for open sky and clouds at 7 km height. The main difference between the curves is that low visibility results in higher radiance at high elevations and lower radiance at low elevation. This results in a smaller radiance range. In figure 4.6 the visibility is set to 10 km and the aerosol model is varied to no aerosol, rural, urban and navy (IHAZE card 2) . All the curves, except for the no-aerosol model, are within 0.7 $Wm^{-2}sr^{-1}$ of each other. There will only be a small difference using not quite the correct aerosol model as long as we use an aerosol model. The differences in the midlatitude summer model are less then those in the midlatitude winter model.

The wind speed does not result in significant changes in the radiance profile when used for midlatitude winter conditions. The height of operation has some influence (see figure 4.7).
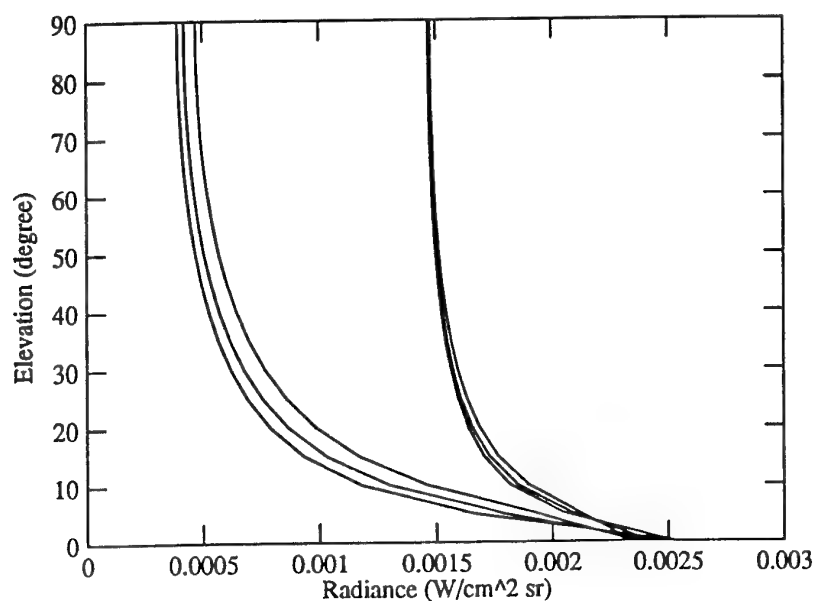
Figure 4.5:   Midlatitude winter lowtran calculations for visibilities of 5, 10 and 25 km. Clear
               sky left curves and clouds at 7 km right curves. At high elevations from left to
               right 20, 10 and 5 km. At low elevations 5, 10 and 20 km visibility.
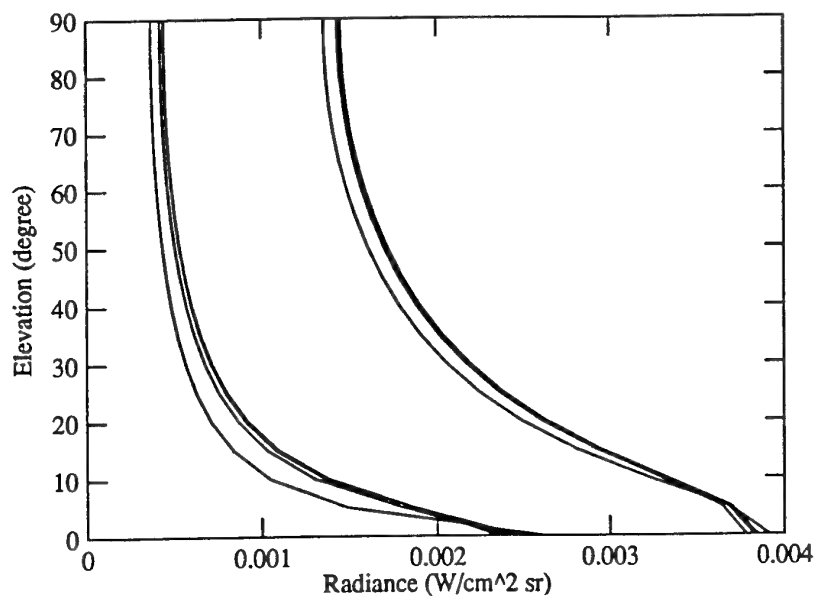
Figure 4.6:   Midlatitude winter (left) and summer (right) lowtran calculations for aerosol mod-
               els. At 90 ° from left to right. First set aerosol models for midlatitude winter: no
               aerosol, rural, navy, urban. Second set for midlatitude summer model: no aerosol,
               rural, urban and navy. This order is not preserved at low elevations. At 0 ° again
               from left to right: rural, urban, navy, no aerosol (all winter) and rural, urban, navy,
               no aerosol (all summer).
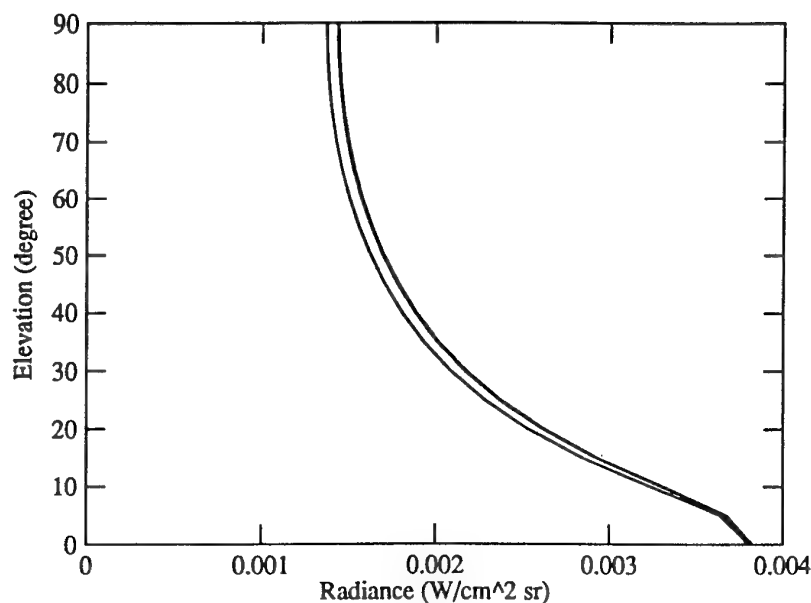
Figure 4.7:   Radiance distribution with the detector at a height of 100m, 10m and 0m (from left to right).

4.4   Atmospheric model

We do not have a complete atmospheric profile but we have meteorological data at ground level. For the total radiance the lowest layers have the greatest contribution. The rightmost curve is the midlatitude summer profile in figure 4.8. Starting with the lowest layers these are replaced with the midlatitude winter profile. Replacing layers above 5 km height gives rise to changes less then 0.1 $Wm^{-2}sr^{-1}$. For radiance prediction only the lowest 5 km of the atmosphere are important. The model consists of 4 parameters:

- Temperature at ground level $T(0)$.

- Relative Humidity RH or water vapor pressure P_w.

- Air pressure $P(0)$.

- Visibility V.

The first three parameters are used to estimate the first 5 km of the atmosphere [4]. The visibility is necessary for its large influence on the radiance at low elevation.
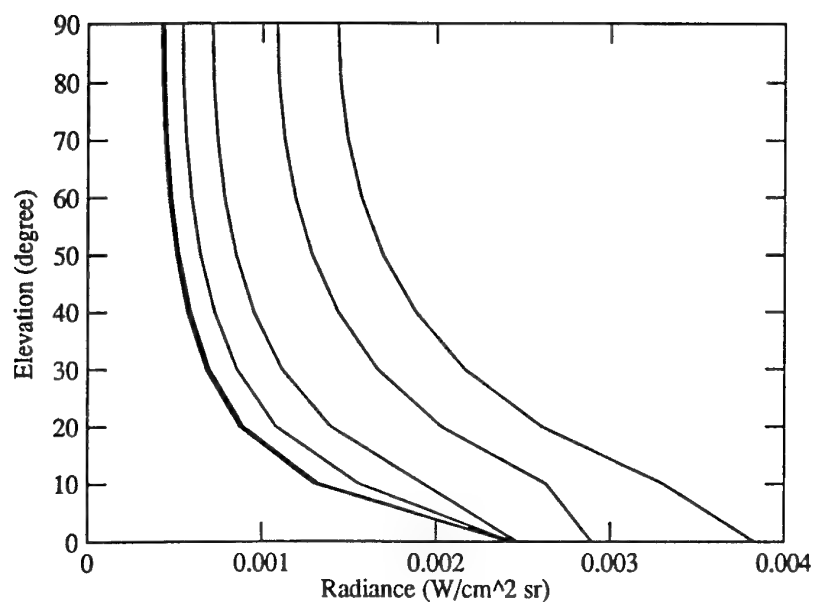
Figure 4.8:   Lowtran calculation using combination of the midlatitude summer and winter
                model. The outmost right curve is based on the midlatitude summer model. The
                outmost left curve is based on the midlatitude winter model. Starting with the first
                layers the midlatitude summer data is replaced with the midlatitude winter data.
                From left to right the curves after replacing the layers up till 26, 20, 14, 10, 6, 4,
                3, 2 and 1 km. Only the last three curves (3, 2 and 1 km) can be seen. The other
                curves are together with the midlatitude winter model a broad band.

Height	Pressure	(mb)	Temperature	(K)	Water vapor	(g/m³)
(km)	LOW	MDL	LOW	MDL	LOW	MDL
0	1018	1018	272.2	272.2	3.5	3.5
1	897	894	268.7	268.2	2.5	2.4
2	790	783	265.2	264.2	1.8	1.6
3	694	685	261.7	260.2	1.2	1.1
4	608	597	255.7	256.2	0.66	0.77
5	531	520	249.7	252.2	0.38	0.53

Table 4.2: LOW = Midlatitude winter model. MDL = atmospheric model based on ground level data.

We take the atmospheric temperature T to have a linear relationship with height [5].

$$T(h) = T(0) - L_m h \tag{4.1}$$

In equation 4.1 h is the height and L_m a constant value. The atmosphere is assumed to be a homogeneously mixed with the water vapor in hydrostatic equilibrium so that air and water vapor are treated as if they were perfect gases. We use as pressure relation

$$P(h) = P(0)(T(0)/T(h))^k \tag{4.2}$$

and for the water vapor pressure P_w we use

$$P_w(h) = P_w(0) exp(-C_s h) \tag{4.3}$$

These parameters are estimated for the U.S. standard atmosphere 1976 in reference [4]. We estimated these parameters for the midlatitude summer and winter model of lowtran for the first two km. This results in $L_m = 4.0 K/km$, $k = 8.7$ and $C_s = 0.38/km$. Table 4.2 and 4.3 show the model values and the calculated ones using the ground level values. The mismatch in temperature also results in a mismatch in the water vapor density. Figure 4.9 shows the curves using lowtran and the generated profile. The winter curve almost matches and the summer curve has a derviation of at most 1 Wm⁻²sr⁻¹. The higher radiance of the generated summer curve is caused by the higher temperature and water vapor density. This generated model gives a good fit with the lowtran model.

This model is used to calculate the influence of the air pressure, RH and the ambient temperature. Air pressure changes in the order of 10 mbar indicate no significant changes for the curves. The influence of the RH and the temperature is significant. Figure 4.10 shows the resulting curves based on the midlatitude winter model. The effect is very clear to see in figure 4.11 based on the midlatitude

Height	Pressure	(mb)	Temperature	(K)	Water vapor	(g/m³)
(km)	LOW	MDL	LOW	MDL	LOW	MDL
0	1013	1013	294.0	294.0	14.0	14.0
1	902	899	290.0	290.0	9.3	9.6
2	802	797	285.0	286.0	5.9	6.5
3	710	705	279.0	282.0	3.3	4.4
4	628	622	273.0	278.0	1.9	3.1
5	554	549	267.0	274.0	1.0	2.0

Table 4.3: LOW = Midlatitude summer model. MDL = atmospheric model based on ground level data.
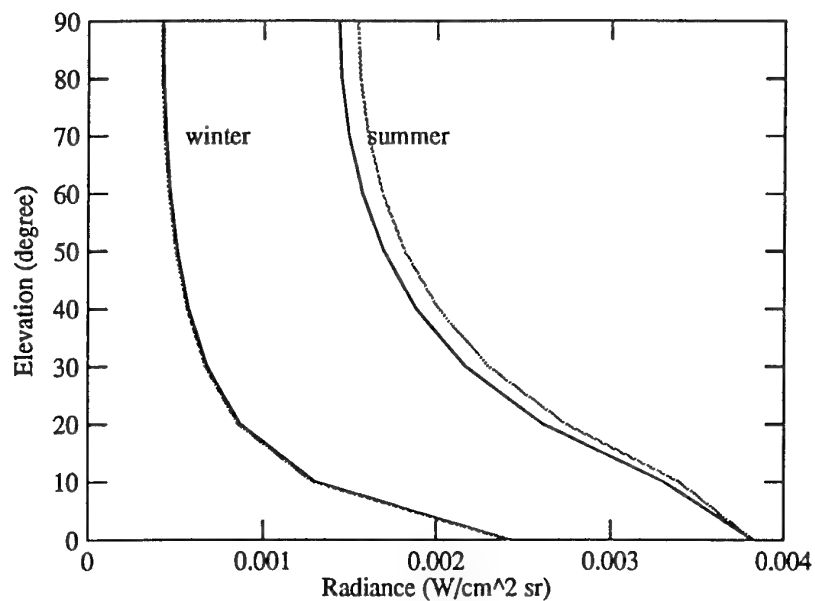
Figure 4.9: Lowtran7 calculations based on the midlatitude winter and summer profiles (solid) and based on a generated profile using the ground level data (grey).

summer model. At low elevations there is no effect when changing the RH. Obvious, a change in the temperature causes a change in radiance. At high elevations the effect of a temperature which is 3° C more or less is the same as a RH of 25 % more or less. Matching radiance at low elevation but deviation at high elevation can indicate a mismatch in humidity.

winter (1018, 62 77 92, 272 +3 -3)
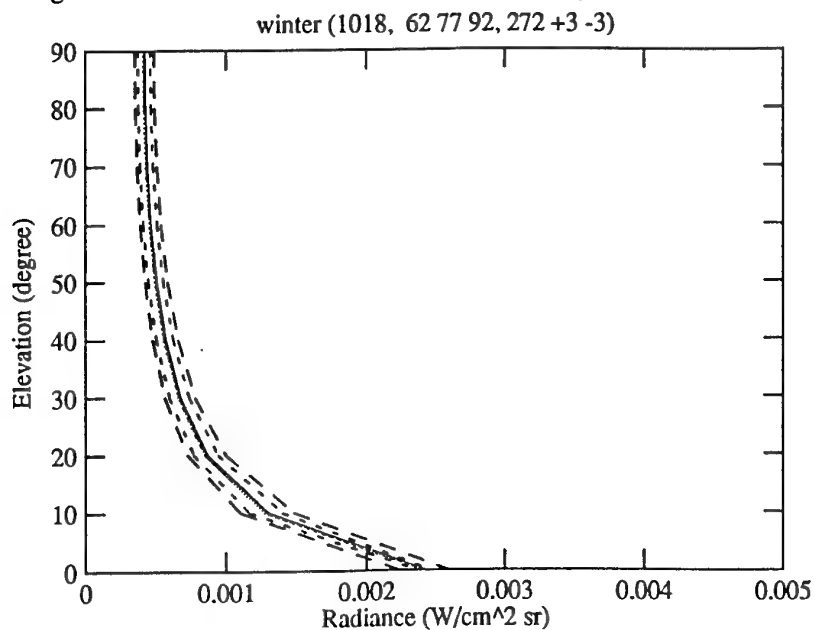
Figure 4.10: Lowtran calculations with the midlatitude winter model (solid), the generated curve based on the ground level data (grey). Generated curves with a RH of 25 % less and more (dotted). Generated curves with a temperature of 3° C less and more (dashed).

summer (1013, 61 76 91, 294 +3 -3)
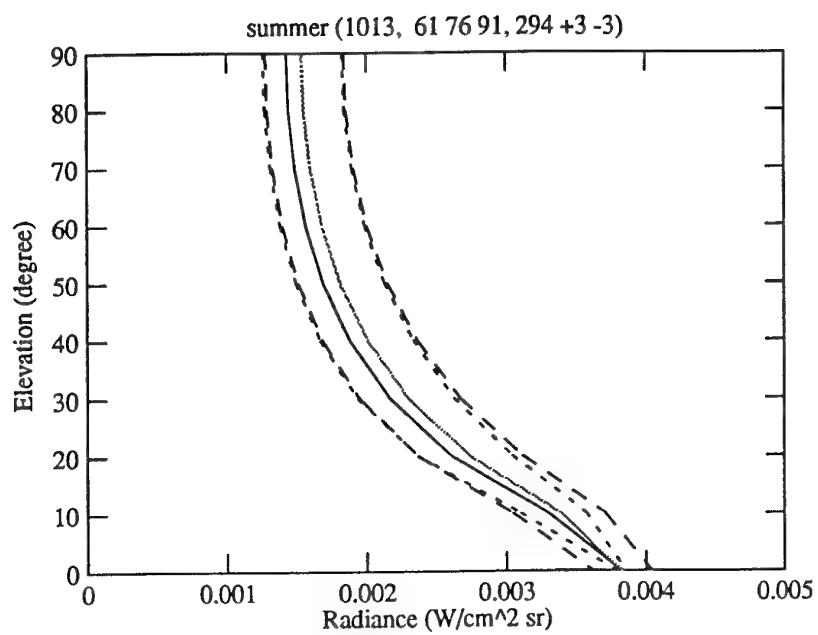
Figure 4.11:   Lowtran calculations with the midlatitude summer model (solid), the generated curve based on the ground level data (grey). Generated curves with a RH of 25 % less and more (dotted). Generated curves with a temperature of 3° C less and more (dashed).

5 RADIANCE WITH ELEVATION MEASUREMENTS

An intriguing part of the radiance with elevation curves predicted by lowtran is the lowest 5 ° (figure 4.3). In the midlatitude summer model a sharp bending of the curve occurs. A bending is also present in all other summer models. None of the measurements do have this bend. Radiance predictions based on the model described in chapter 4 with a high water density also have this bending. The mask used for the blanking of the buildings also mask a small part of the sky. The images start at about 1 °. Crosscuts of unblanked images are made to check if a bend occurs in the last degree. None of the images reveal a bending as in the midlatitude summer model.

This indicates that the description of the atmosphere is not quite correct for the conditions at TNO-FEL. The MAPTIP trials nearby TNO-PEL were an opportunity to check this. Images were acquired using the cloud scanner on 28 and 29 October 1993. Three weather balloons were used to measure the atmospheric profile as part of the MAPTIP trials.

Figures 5.1, 5.2 and 5.3 show the radiance with elevation predictions of lowtran based on the atmosphere profile (solid) and based on the model of chapter 4 which itself is based on ground level meterological data (dashed). The bending in the generated curves is not present in the radiance prediction based on the measured atmospheric profile. Comparing both profiles the big difference is the humidity and an inversion layer (see tables 5.1 to 5.6). The measured profile has a RH of 30 % above 1 km while according to the model the RH should decrease with increasing heights. Also an inversion layer exists which is not incorporated in the generated atmosphere of the model. Both can be incorporated in the model by using at 1 km an identical temperature as present at the ground level and by setting RH to a fixed value of 30 % for heights from 1 km to 5 km. The pressure and temperature remain identical to the model of chapter 4. We use for this model also the rural aerosol model. This model is the grey curve in figure 5.1, 5.2 and 5.3. Although this curve also does not match the prediction based on the atmospheric profile the shape of the curves is identical. The difference in this curves is caused by an inversion layer temperature which is higher than the temperature used in the model.

Comparing the predicted radiance curves with the real measurements show that the measured radiance curve is much more curved at low elevations (see figure 3.9). A rapid decrease in radiance occurs in the first 20 °. The lowtran prediction show a smaller decrease. This is especially true for the summer models conditions. A better match can be achieved with a model that results in a more curved radiance prediction. Figure 4.6 shows that the no-aerosol model fulfills this condition. The first two models use "rural" as aerosol model. The third model we use consist of using the
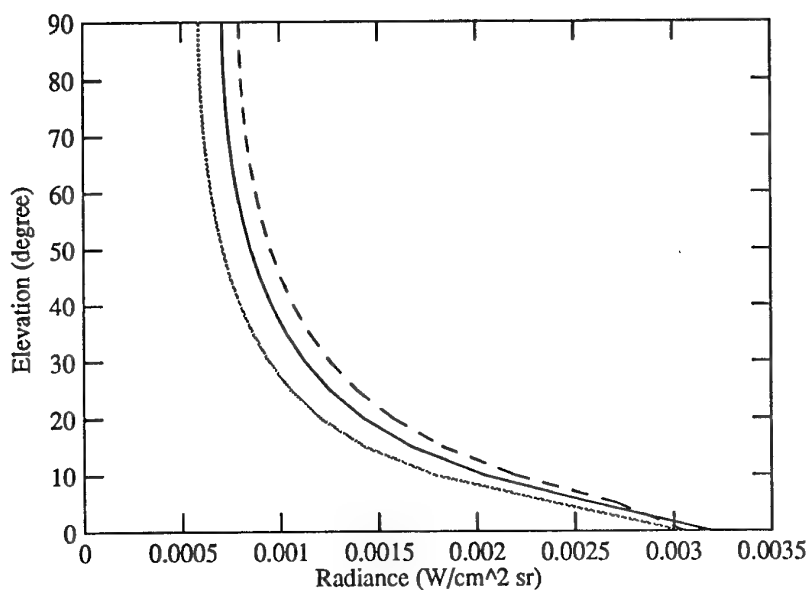
Figure 5.1:   Radiance predictions for 28 October 1993 1300 UTC by lowtran based on a mea-
sured atmospheric profile (solid) and based on generated atmospheric profiles
(dashed, grey).
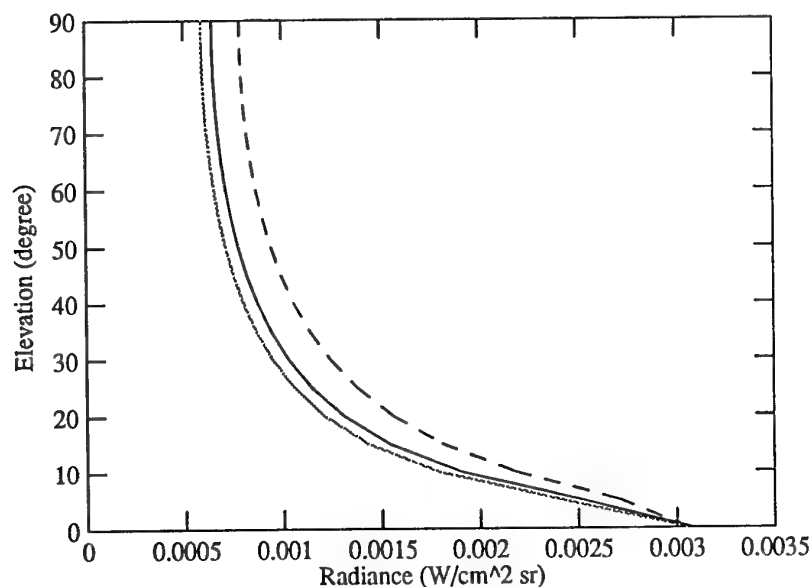
Figure 5.2:   Radiance predictions for 29 October 1993 1500 UTC by lowtran based on a mea-
sured atmospheric profile (solid) and based on generated atmospheric profiles
(dashed, grey).

Height	Pressure	Temperature	RH
(km)	(mb)	(^{o}C)	(%)
0.008	1028.2	8.8	86.0
0.073	1020.1	8.2	73.2
0.380	982.8	5.2	97.3
0.725	941.9	2.2	100.0
0.744	939.7	2.2	93.1
0.766	937.2	2.7	52.5
0.794	934.0	6.4	28.0
0.833	929.5	8.5	22.1
1.003	910.7	10.9	33.1
2.597	750.4	4.0	38.5
4.331	603.5	-7.3	34.2
4.698	575.7	-8.7	22.5
5.683	505.9	-17.1	24.7
6.214	471.2	-19.8	22.1
8.120	361.5	-35.4	27.5
9.788	282.6	-48.2	28.1
11.475	217.2	-61.0	30.4
12.451	185.3	-65.3	31.0
14.427	134.4	-64.9	30.0
16.926	89.3	-65.4	29.4
18.144	73.2	-62.2	28.7
19.375	60.0	-62.0	28.3

Table 5.1:   Atmospheric profile at 28 October 1993 1300 UTC.

Height	Pressure	Temperature	RH
(km)	(mb)	(K)	(%)
0.000	1028.200	281.950	87
1.000	908.010	277.950	77
2.000	800.425	273.950	69
3.000	704.280	269.950	62
4.000	618.501	265.950	57
5.000	542.101	261.950	52
6.000	462.700	243.700	43
7.000	401.600	237.700	31
8.000	347.300	231.700	23
9.000	299.300	225.700	19
10.000	256.800	219.700	17
11.000	219.900	219.200	5.5
12.000	188.200	218.700	3.0
13.000	161.100	218.200	2.3
14.000	137.800	217.700	2.0
15.000	117.800	217.200	1.8
16.000	100.700	216.700	1.6
17.000	86.100	216.200	1.4
18.000	73.600	215.700	1.3
19.000	62.800	215.200	1.2
20.000	53.700	215.200	1.0

Table 5.2:   Generated atmospheric profile at 28 October 1993 1300 UTC based on ground
level meteorological data .
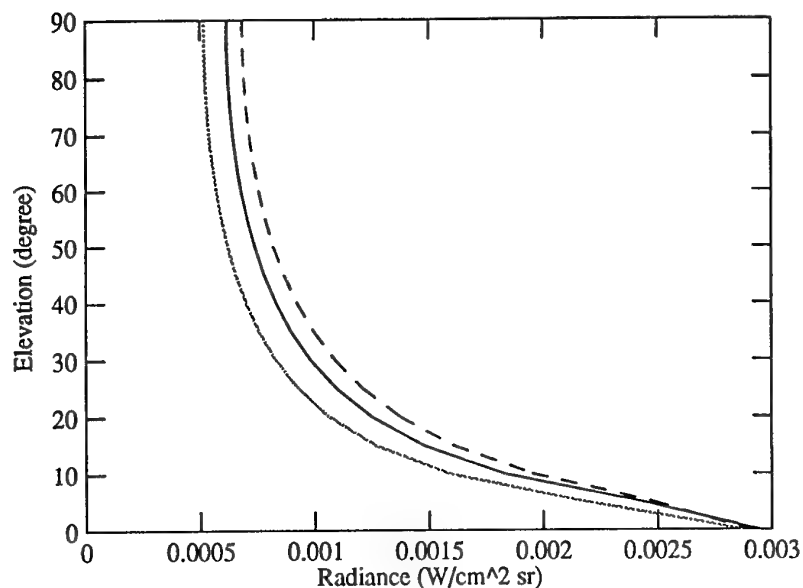
Figure 5.3: Radiance predictions for 29 October 1993 2100 UTC by lowtran based on a measured atmospheric profile (solid) and based on generated atmospheric profiles (dashed, grey).

Height (km)	Pressure (*mb*)	Temperature (°*C*)	RH (%)
0.008	1027.7	9.1	83.0
0.307	991.1	6.2	97.2
0.370	983.6	9.9	59.0
0.456	973.5	11.4	35.7
0.661	949.9	12.3	30.7
1.513	857.6	9.4	30.1
2.340	775.3	3.2	45.6
2.682	743.2	2.2	22.5
3.280	689.9	0.7	19.7
4.960	557.1	-11.2	24.4
5.964	487.7	-20.1	24.5
6.304	465.8	-20.7	19.7
8.144	360.3	-35.2	25.3
9.881	278.5	-49.8	27.4
11.146	228.8	-57.3	28.5

Table 5.3: Atmospheric profile at 29 October 1993 1500 UTC.

Height (km)	Pressure (mb)	Temperature (K)	RH (%)
0.000	1027.700	282.250	84
1.000	907.689	278.250	75
2.000	800.252	274.250	67
3.000	704.227	270.250	60
4.000	618.544	266.250	55
5.000	542.220	262.250	51
6.000	462.700	243.700	44
7.000	401.600	237.700	31
8.000	347.300	231.700	23
9.000	299.300	225.700	19
10.000	256.800	219.700	17
11.000	219.900	219.200	5.5

Table 5.4: Generated atmospheric profile at 29 October 1993 1500 UTC.

Height (km)	Pressure (mb)	Temperature ($^{\circ}C$)	RH (%)
0.008	1029.0	6.2	88.0
0.151	1011.2	5.1	98.5
0.393	981.8	6.9	80.8
0.534	965.2	11.4	41.6
0.866	927.7	11.8	28.2
1.680	841.1	8.3	26.4
2.308	779.0	3.8	29.8
2.626	749.0	3.5	22.2
4.208	614.1	-6.2	21.3
4.900	561.7	-10.8	22.7
5.682	506.6	-18.2	28.1
6.028	483.7	-19.4	25.2
7.694	383.9	-34.5	30.5
9.347	301.3	-46.3	30.8
10.989	234.0	-56.5	32.2
12.301	189.8	-62.0	32.9
12.934	171.3	-62.8	32.9
13.530	155.5	-60.8	32.5
14.961	123.5	-63.2	32.3
15.407	114.9	-62.2	32.2
17.532	81.3	-63.3	32.0

Table 5.5: Atmospheric profile at 29 October 1993 2100 UTC.

Height	Pressure	Temperature	RH
(km)	(mb)	(K)	(%)
0.000	1029.000	279.350	89
1.000	907.658	275.350	79
2.000	799.156	271.350	71
3.000	702.295	267.350	65
4.000	615.973	263.350	60
5.000	539.178	259.350	55
6.000	462.700	243.700	43
7.000	401.600	237.700	31
8.000	347.300	231.700	23
9.000	299.300	225.700	19
10.000	256.800	219.700	17
11.000	219.900	219.200	5.5
12.000	188.200	218.700	3.0
13.000	161.100	218.200	2.3
14.000	137.800	217.700	2.0
15.000	117.800	217.200	1.8
16.000	100.700	216.700	1.6
17.000	86.100	216.200	1.4
18.000	73.600	215.700	1.3

Table 5.6:   Generated atmospheric profile at 29 October 1993 2100 UTC.

no-aerosol model, an inversion layer at 1 km with a temperature of ambient + 2 °C and a RH of 20 %. Except these changes the atmospheric profile is identical to model 2.

The three models are:

1. Original model described in chapter 4.4 which is based on the midlatitude models of lowtran and uses the "rural" aerosol model.

2. The adapted model based on balloon profiles which indicate the presence of a inversion layer and a RH which is 30 %. This model uses also the "rural" aerosol model.

3. The model adapted to the curvature of the measured curves. The prediction based on model 1 and 2 have a radiance which decreases too slow compared to the measured profiles. Using "no-aerosol" as aerosol model and a small adaption in the inversion layer by using a 2 ° C higher temperature and a RH of 20 %.

All images are analysed using these three models. An example is figure 5.4. The minimum and maximum measured radiance with elevation are the solid lines. The units in the horizontal direction are the measured bit value and in the vertical direction the line numbers (0 is the top of the images, 500 the bottom and the horizon is at line number 430). The blanking also maskes a part of the sky at low elevations. In general the curves start at 1 °. The solid curves are an outline of the 2-dimensional radiance histograms as in figure 3.9. The image was made with an almost clear sky. The minimum and maximum curve have little deviation of each other. The three models are drawn in grey. At high elevations the order is from left to right model 3, 2 and 1. Models 1 and 2 have the same radiance at 0 °. Model 3 has a higher radiance 0 ° but due to the sharp decrease the radiance at 5 ° is less than model 1 and 2. The model 1, 2 and 3 curves can be distinguished by the fact that at high elevation the order is form left to right model 3, 2 and 1. The order at low elevations is not always the same.

The radiance contribution of a horizontal path (0 °) can be predicted very well with the ground level meteorological data. Only the first layer is important for the radiance. To make a good prediction at higher elevations also information about the atmospheric profile is needed. The mismatch at high elevations is due to this unknown profile. The mismatch at low elevations is caused by the blanking of the image. To blank the image and remove all the buildings at low elevations the blanking starts at 1 °. The last 1 ° of the radiance curve is not shown in this figure. Examination of crosscut of the images shows that in the last degree the curve sharply bends and coincides with the prediction based on model 1 and 2.

In figure 5.4 none of the generated curves have a really good or bad match with the measured curve. The starting radiance (high line numbers) of model 3 is too high. This is due to the fact that

lowtran does not use the water density in its calculation for the no-aerosol model. An example of a measurement with a low water density is figure 5.5. The three models have nearly identical values at all elevations. The RH during this measurement was 38 %, the temperature 281.9 K and the pressure 1021 mbar. The mismatch in model 1 and to some extend in model 2 are in the first 5 °. The starting radiance is correct but the lowtran calculations have a too small decrease in radiance with increasing elevations. The effect of the water density is good for the radiance prediction for a horizontal path but for a vertical path the contribution is overestimated in the model 1 and 2 predictions. Figure 5.6 and 5.7 are measurements and prediction with nearly identical meteorological conditions. The solid curves of the measurement are nearly identical. The model 3 curve, which is not influenced by the water density, is the same in both figures. This is also the case for the model 2 curve. But the model 1 curve is shifted at high elevation about 50 LSB in radiance value. None of the measurements at TNO-FEL indicate this great dependence for the water density. Model 1 in general gives the greatest mismatch between the measured and the predicted radiance values. Model 1 is not the best description of the atmospheric profile.

Model 2 is less dependent for the water density than model 1. The predictions made by model 2 are better than model 1. Model 2 is based on atmospheric profile measurements on 28 and 29 October 1993 during the MAPTIP trail. In figure 5.8 the solid curves are again the minimum and maximum radiance with elevation, the three grey lines are the three model based curves and the third solid line is the prediction based on the measured atmospheric profile. Both the model 2 and 3 curve and the radiance prediction based on the measured profile match the measured radiance well. In this image a larger blanking mask was used due to the placement of mounting devices for a HF antenna. The first values are at an elevation of about 3 °. Figure 5.9 is made in the same meteorological conditions. The temperature is 0.1 K higher, the pressure is 14 mbar lower and the RH is 2 % higher. Model 2 has a greater deviation than figure 5.8. Model 3 still matches reasonably well.

The conclusions for the three models are:

- Model 1 is based on the lowtran midlatitude summer and winter profiles and is used with the rural aerosol model. The predictions are correct for a horizontal path ($0°$ elevation) but for a slant path a mismatch exists. This mismatch is most striking at the first 5 °.

- Model 2 is a meteo profile adapted to atmospheric measurements made on 28 and 29 October 1993. The model has also the correct radiance value at 0 ° and the overall fit is better than model 1. The match is very good for the measurements made on 28 and 29 October as can be seen in figure 5.8. The models prediction match less for other days (see figure 5.9). The main reason is still the large influence of the water density on the predictions. Curves based on low water density have an identical shape as the measured curves. The curves based on a

/abq/ackn4//10088 meteo: 1014.0 295.5 57.0 1061 radiance 1307 3921
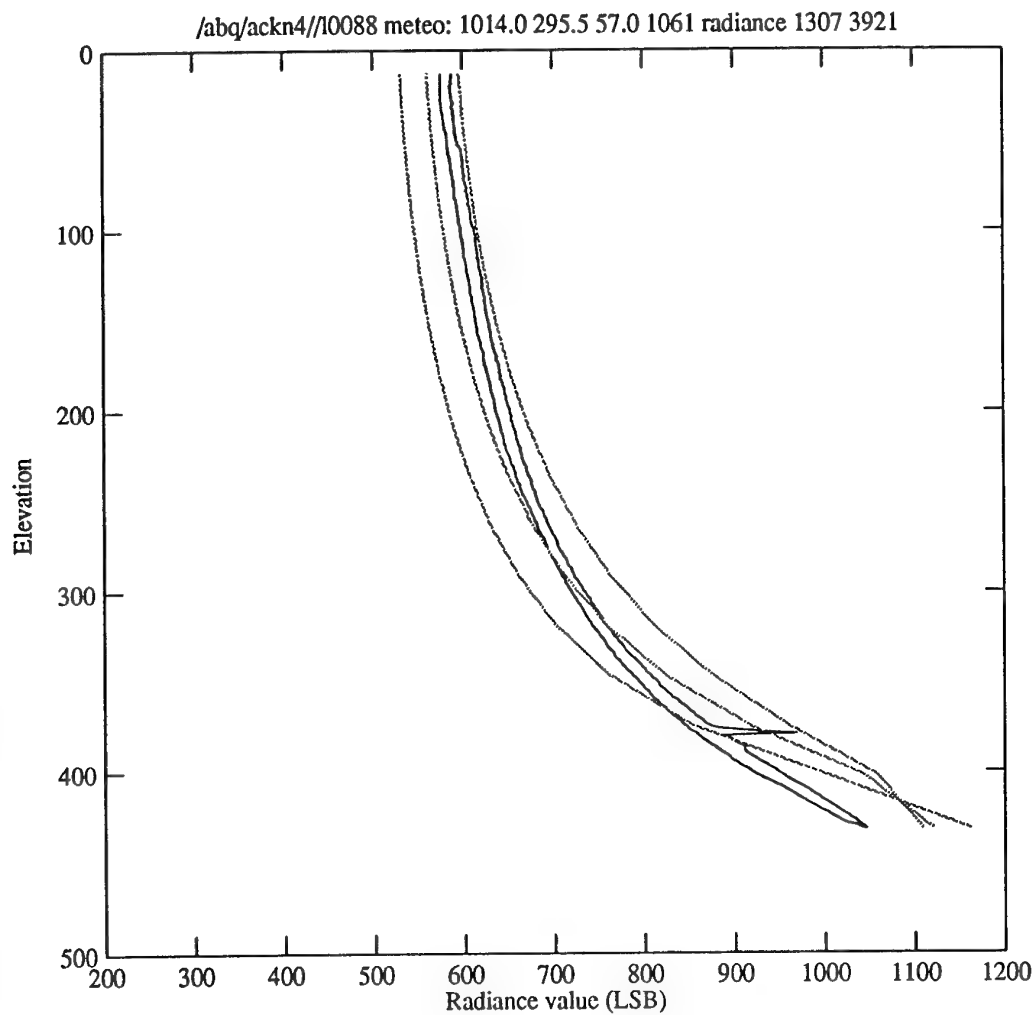
Figure 5.4:   Real measurements and lowtran predictions of the radiance with elevation for
measurement 88 on 11 May 1993 14:12 CEST. The radiance is in bit values as
measured using the absolute range and a gain of 8. The solid lines are the min-
imum and maximum radiance with elevation measured. The grey lines are the
radiance prediction made with atmospheric model 1, 2 and 3. The three models
can be identified at high elevations. The order is always from left to right model
3, 2 and 1.

/abq/ackn4//l0068 meteo: 1021.0 281.9 38.0 0 radiance 459 3045

Figure 5.5:   Real measurements and lowtran predictions of the radiance with elevation for
measurement 68 on 29 March 1993 15:57 CEST . The low water density result in
three almost identical prediction for the three models.

/abq/ackn4//l0090 meteo: 1007.0 296.8 48.0 1061 radiance 1201 3968

Figure 5.6:   Real measurements and lowtran predictions of the radiance with elevation for
measurement 90 on 12 May 1993 14:15 CEST. Meteorological conditions: tem-
perature 296.8 K, 1007 mbar and RH of 48 %.

/abq/ackn4//L0085 meteo: 1015.0 296.1 60.0 1088 radiance 1432 3932

Figure 5.7:   Real measurements and lowtran predictions of the radiance with elevation for
measurement 85 on 28 April 1993 13:06 CEST. Meteorological conditions: 296.1
K, 1015 mbar and RH of 60 %. Only the model 1 curve is really different in this
figure and in figure 5.6.

high water density have a different shape in the first 5 °. This bending is not present in the measured radiance curves.

- Model 3 has a shape that looks like the measured curves. Model 3 is a no-aerosol model and the radiance predictions are only slightly influenced by the water density. The result of this is an incorrect prediction of the radiance for 0 ° but a shape that looks like the measured curves.

The overall conclusion is that in general model 3 has the best match but that the radiance prediction for the first degree is too high. Model 2 matches good in low water density meteorological conditions and has a correct radiance prediction for a horizontal path. The influence of the water density in the lowtran predictions for the radiance is too great as concerning the condition at the coast of The Netherlands.

Using this simple model good predictions can be made of the radiance with elevation. It is possible to make a program that varies the atmosphere parameters to match the measured curve. To know what realistic changes are, more atmospheric profiles are needed. With this knowledge very good predictions can be made as can be seen in figure 5.8. The influence of different layers depends on the elevation angle. Radiance values of all angles from 1 ° to 70 ° are known. With the extra knowledge of realistic changes a good prediction of the atmospheric profile for the first 5 km can be made.

/abq/ackn4//L0122 meteo: 1031.0 283.5 90.0 940 radiance 913 3063
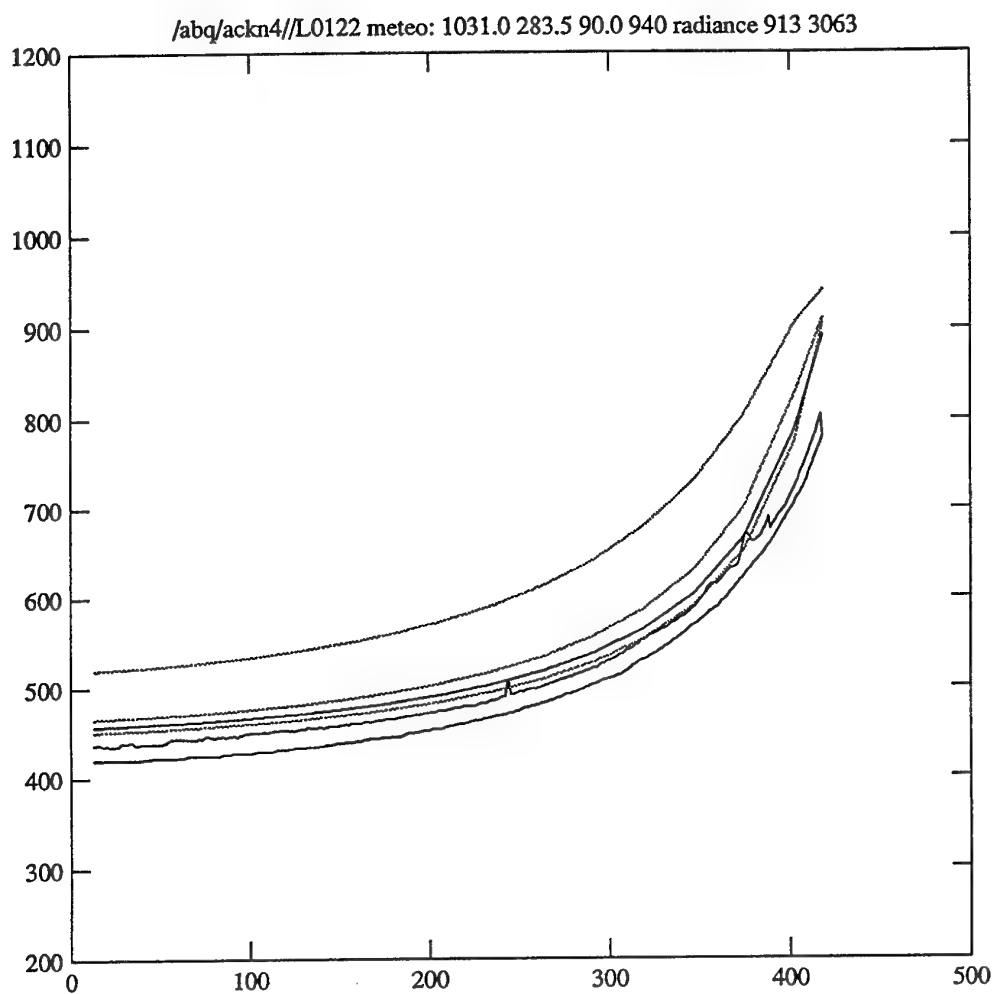
Figure 5.8:   Real measurements and lowtran predictions of the radiance with elevation for measurement 122 on 29 October 1993 11:23 CET.

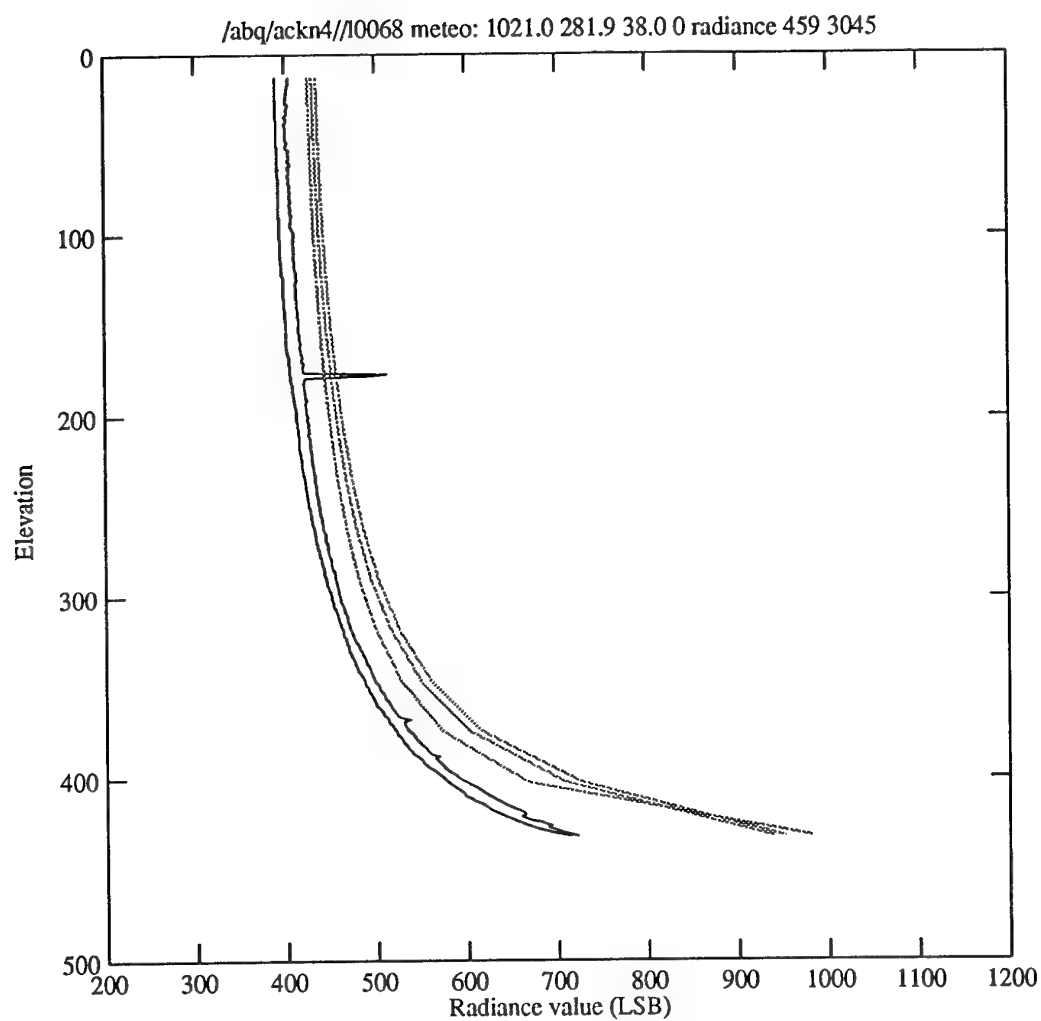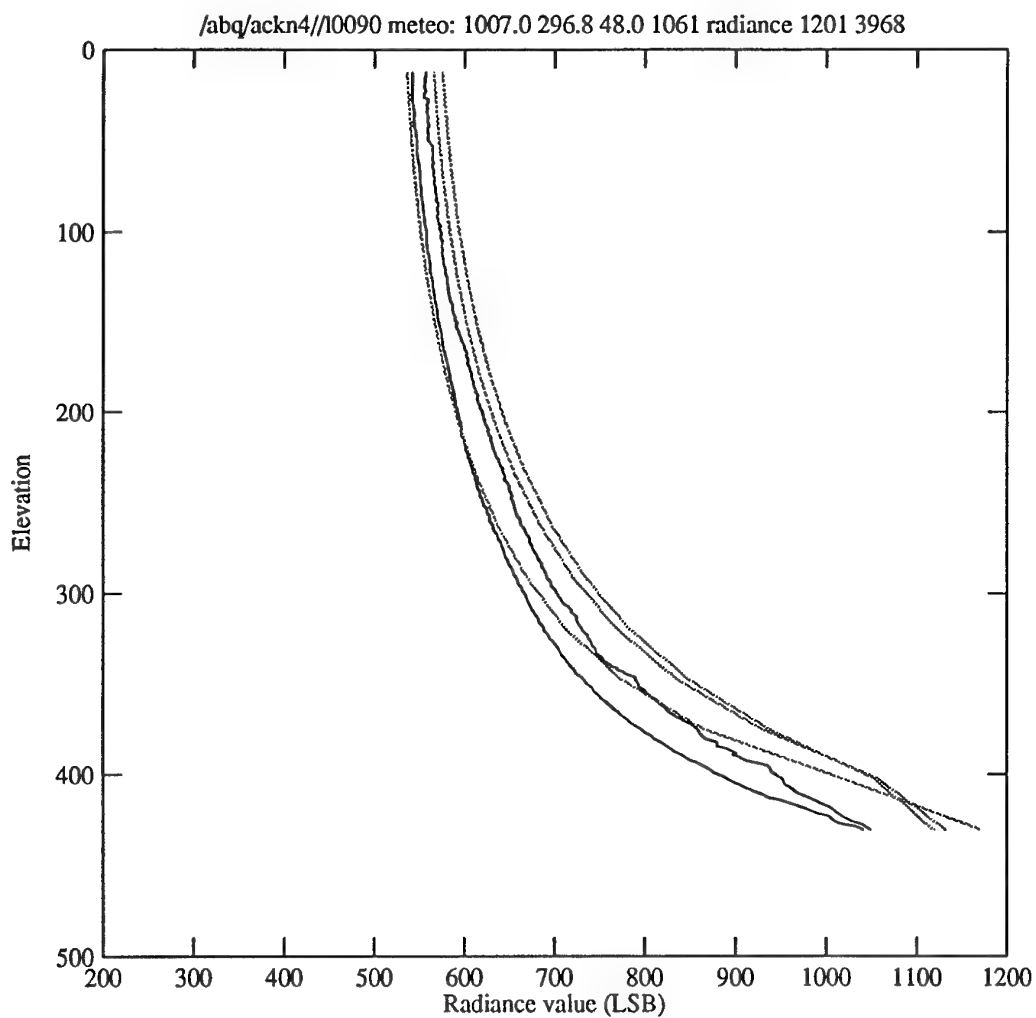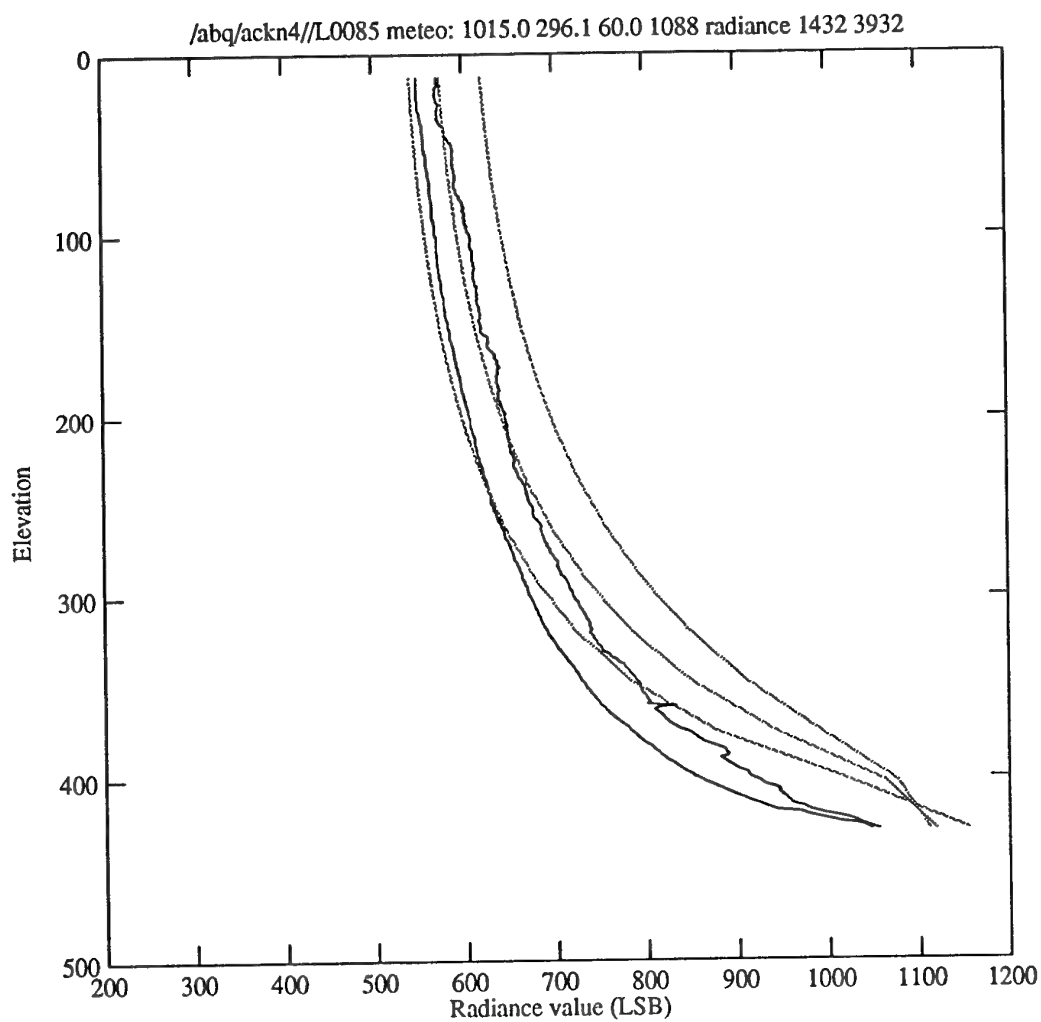/abq/ackn4//L0072 meteo: 1017.0 283.6 92.0 0 radiance 1015 3125
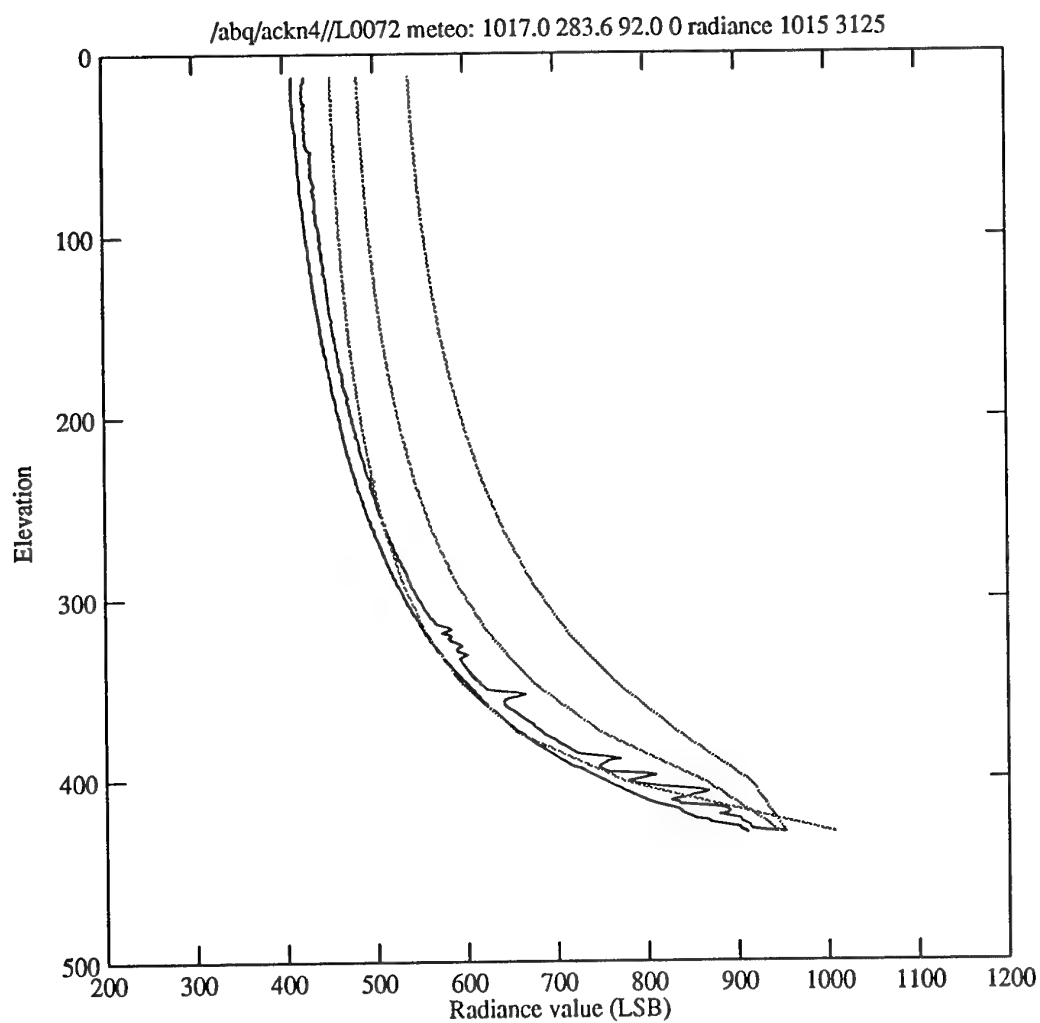
Figure 5.9:   Real measurements and lowtran predictions of the radiance with elevation for measurement 72 on 15 April 1993 13:27 CEST.

6 IMAGE ANALYSIS

6.1 Introduction

The analyses of the images concentrated in three main directions: profile, clutter and cloudiness. The analyses of the radiance profile is described in chapter 5. In this chapter the clutter and cloudiness are described. The measurement conditions can change significantly during a day. The absence or presence of cloud layers has a great influence on the measured radiance with elevation. An example of this is given in paragraph 6.2. The presence of clutter hampers the identification and detection of objects. In paragraph 3.2 a description of the clutter contents in an image is described. The clutter is correlated with the cloud type and the cloud height. The radiance and RMS' distribution are used to calculate the cloudiness. Both the clutter and cloudiness give an impression of the potential detection limit of the system in specific conditions.

6.2 Daily variations

Figure 6.1 shows nine distributions of image radiance with elevation recorded on 15 January 1993 between 9:57 CET and 14:37 CET (Central European Time). All measurements are shown at the same scale. As can be observed from the diagrams, different cloud layers existed during that day at different heights. These cloud layers partially shielded each other. These changing cloud conditions were also recorded at the Meteorological Office, as shown in table 6.1. Other general weather conditions are a 80 % relative humidity at 10°C ambient temperature, a visibility of around 13 km, and a wind velocity of about 20 kts.

To illustrate the analysis of clouds and cloud clutter we have analysed a large number of images recorded on a single day (15 January 1993). During the observation of figure 6.1.a a cloud layer at a low height covers almost the entire sky. Small disturbances from the layer are clearly seen as

	10:00 CET	13:00 CET	15:00 CET
Cloud layer 1	1 Sc 2,000	1 Sc 4,000	2 Sc 1,500
Cloud layer 2	3 Sc 4,000	5 Ac 10,000	8 Sc 1,800
Cloud layer 3	6 Ac 8,000	7 Ci 22,000	—

Table 6.1: Cloud conditions at 15 January 1993 (octa/type/height(ft)).

deviations from the main curve in the figure. In figure 6.1.b, 15 minutes later, the complete sky is covered with this layer. The height of the cloud layer can be estimated from the radiance of the sky. According the meteorological data the height of this stratocumulus (Sc) layer is about 4000 ft. In figure 6.1.c (after 50 minutes) and 6.d (after 2 hours) the cloud layer at 4000 ft has vanished and an altocumulus (Ac) layer covers the sky. This layer is at about 10,000 ft and again covers the entire sky. Only a limited amount of distortion from the main curve is present in figure 6.1.d. Around 13:00 CET the 10,000 ft layer covers 5 octa of the sky. In figure 6.1.e also a cirrus (Ci) cloud layer at 22,000 ft of 7 octa is present. In figure 6.1.f and 6.1.g the altocumulus layer covers again almost the whole sky. But in 6.1.g deviations from the main curve occur at almost all elevations. In figure 6.1.h the sky is almost filled with stratocumulus clouds. Just above the TNO-FEL building there is a gap in this layer so we also see the Altocumulus layer. In figure 6.1.h these layers can be distinguished by their different radiance. We see in fact two parts of different main curves. From $0°$ to $50°$ elevation we see stratocumulus and from $65°$ to $72°$ we see altocumulus. In figure 6.1.i the low-height stratocumulus layer covers again the complete sky. By comparing the high elevation radiances between figure 6.1.b and 6.1.i it we see that the clouds in the latter image have a higher radiance value and the cloud height should be lower. This is confirmed by the meteorological data presented in table 6.1. Our measurements are also confirmed by a LIDAR system of the KNMI in De Bilt. Figure 6.2 shows these measurements. De Bilt is around 100 km East of the Hague. A time delay will occur caused by the time necessary for the wind to blow the clouds to that position.

6.3   Clutter

The created histograms or images of the RMS' (and RMS) variations generally consist of a gaussian distribution caused by the system noise of the scanner and detector system and a high-RMS' tail caused by clutter. After application of the spatial filter, present-day detection algorithms use an adaptive threshold to detect targets (i.e. $\mu + k\sigma$, where k is set by CFAR and the acceptable processing load; see e.g. Coates[6]). These thresholds are adaptive to the local structure, which can be quantified by the RMS' value. Therefore, the tail of the RMS'-distribution is the interesting part with respect to clutter hampering detections. This tail normally consists of only a few percent of the total area. To show these high clutter areas of interest all distributions in this report are presented on logarithmic scales.

The earlier proposed methods for calculating clutter values are based on a single clutter metric. In those cases a summation was performed of all RMS'-values exceeding the cut-off limit of $\mu + 3\sigma$. The disadvantage of this method is that a scene with a large number of low RMS'-values (but higher than the cut-off limit) give the same clutter value as a small number of high RMS'-values. Hence,
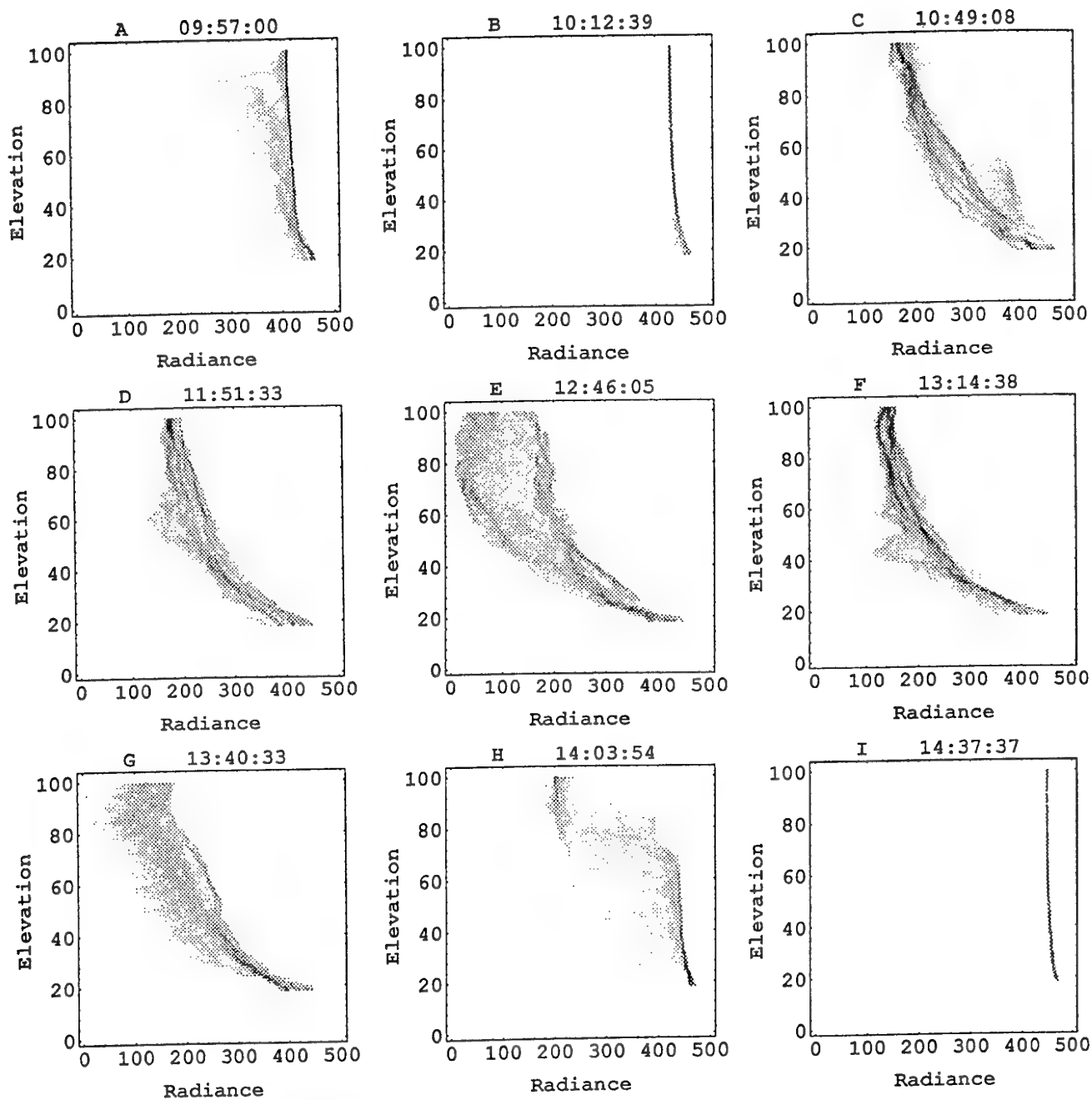
Figure 6.1: Daily variation in cloud height and octa results in differences in radiance. Nine images obtained at 15 January 1993 between 9:57 and 14:37 CET.
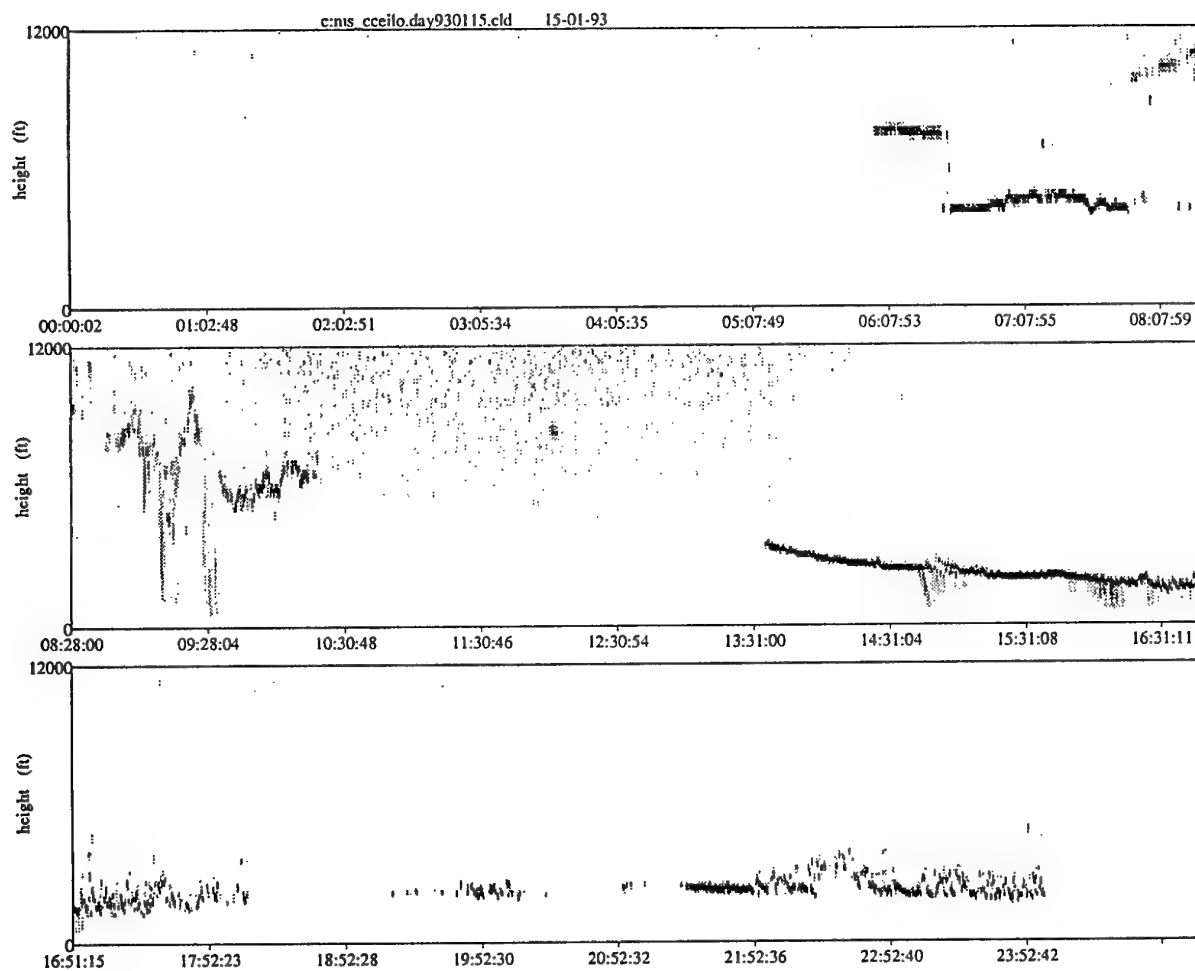
Figure 6.2:   LIDAR measurement.

when looking only at the resulting clutter values we get the impression that we have a similar scene. In effect, a large number of low RMS'-values exceeding the detection threshold have an important effect on the processing load and may therefore degrade the system performance (detection range) by a threshold increase (i.e. sensitivity decrease). Of course the threshold increase is caused to limit the number of unwanted temporal correlations. On the other hand, a few high RMS'-values have a more important influence on the clutter rejection process. Without the threshold increase the same performance is kept. It will take some computing effort to get rid of these false detections. It is not clear to say which case is worse as this depends on the further system and threat details. An additional point is valid for similar cloud clutter (the same continuous RMS' distribution; similar to the distributions found in this report) measured with different sensor systems. Less sensitive systems (with a higher Noise Equivalent Irradiance NEI and therefore a higher irradiance threshold) give a lower clutter value than more sensitive systems (with a lower NEI). This is because the number of cells which are above the $\mu + 3\sigma$ threshold limit is smaller in the high NEI case.

A way to overcome the problem of clutter value ambiguity discussed in the previous paragraph is to calculate the slope of the tail of the distribution in addition to the clutter metric value. As we shall show in this report the value of this slope gives a good estimate of the cloud clutter present in the image. The slope of this tail is independent of the noise of the system and gives a good prediction with respect to the detection hampering clutter. We fit the slope with

$$\log(Number \ of \ \mathrm{RMS'} \ cells) = \mathrm{RMS'}/\alpha + \beta.$$

We are not interested in the gaussian (noise) part of the RMS'-distribution and we therefore only use values for the fitting procedure in the RMS'-histogram above the $\mu + 4\sigma$ limit. The gaussian part of the system is quite consistent, with $\mu \approx 0.11$ and $\sigma \approx 0.015$ Watt m^{-2}sr^{-1}, in most cases with only a small variation. The upper limit for the fit is reached when blocks containing sums of ten consecutive RMS'-bins are equal to zero (hence between 10 and 20 consecutive RMS'-bins are equal to zero). To calculate the fit coefficients α and β we use a weighed least square method. The weight factor that we use is the number of cells with that particular RMS' value. The combination of the α and β gives in most scenes a complete description with respect to the cloud clutter. This method will be used throughout this report. The constant β can be related to the clutter metric as described earlier by summation of RMS' values above the $\mu + 3\sigma$ level.

There exists a clear correlation between the slope of the tail of the RMS'-distribution $(1/\alpha)$ and the cloud type in combination with the cloud base height. Our images can be divided into six groups: totally clear or empty sky, all covered with clouds or overcast, Cumulus clouds (Cu), Stratocumulus clouds (Sc), Altocumulus clouds (Ac), Cirrus clouds (Ci). Some characteristic clutter distributions for these clouds are shown in figure 6.3. This figure presents six RMS'-histograms for the entire

Scorpio image on a logarithmic scale. The label gives the image number and the cloud situation. The x-axis shows the RMS' values from 0 to 1 Watt $m^{-2}sr^{-1}$. The y-axis gives the number of cells for each RMS' value. Note that the y-scale is logarithmic and that the tail in the histograms start at about the 1 % level or lower of the peak histogram value. The clutter tail is always descending. The integral under the histogram equals the total number of data points in the clutter map (around 140,000 cells).

Observations from the totally clouded and the all clear sky give a gaussian distribution caused by the noise of the Scorpio system. It can also be seen that in the clear sky distribution a few high clutter values exist. These are caused by (one or more) objects such as birds and airplanes but are certainly not caused by cloud clutter. These objects cannot be seen in the overcast distribution because the clouds obscure them. To compare the distribution of the other four groups, RMS'-distributions are chosen that are almost equally clouded (2-3 octa). The slopes α are given in the last column of table 1 in Watt $m^{-2}sr^{-1}$/decade. The distributions of Cu, Sc, Ac and Ci clouds show an increasing slope (steeper descend) with increasing cloud height level. There are three possible explanations of this slope-height effect:

- 1. The lower the clouds are (higher temperature) the larger the contrast is between the (cold) clear sky and the clouds (see the Lowtran-7 curves in figure 4).

- 2. The lower the clouds are the smaller the area (in square meter) is of one pixel.

- 3. The clouds at different heights have a different structure.

From the first point it is clear that lower clouds should give larger clutter RMS' values caused by a greater contrast with the empty sky. The effect of the second point is not completely clear. Greater areas can give a smoother clutter value because the radiance is averaged over the whole area. However it can also cause a greater difference between two neighboring pixels. The boundary between the cloud and the sky consists of pixels with radiances within the limits set by the curves of an empty sky and of a cloud. Looking at small physical areas can give a smooth step between the cloud and the sky and hence a low clutter value. Large areas can give much larger steps and larger clutter values. The effect of the area is not yet clear. Also the third effect can be present but is difficult to show, and very situation dependent. The data are obtained in the Mid-latitude winter and summer conditions in the period January-October (with temperatures between 0-23°C). Since clutter is caused by contrast between clouds (edges) and sky the α-slopes can be different in other conditions. Figure 6.4 and 6.5 are made with a time difference of 15 minutes. The clouds are slowly covering a larger part of the sky. In The RMS' slope of histogram of image 6.5 is 0.27 $Wm^{-2}sr^{-1}$/decade while image 6.4 has a slope of 0.13 $Wm^{-2}sr^{-1}$/decade. The clouds are of the
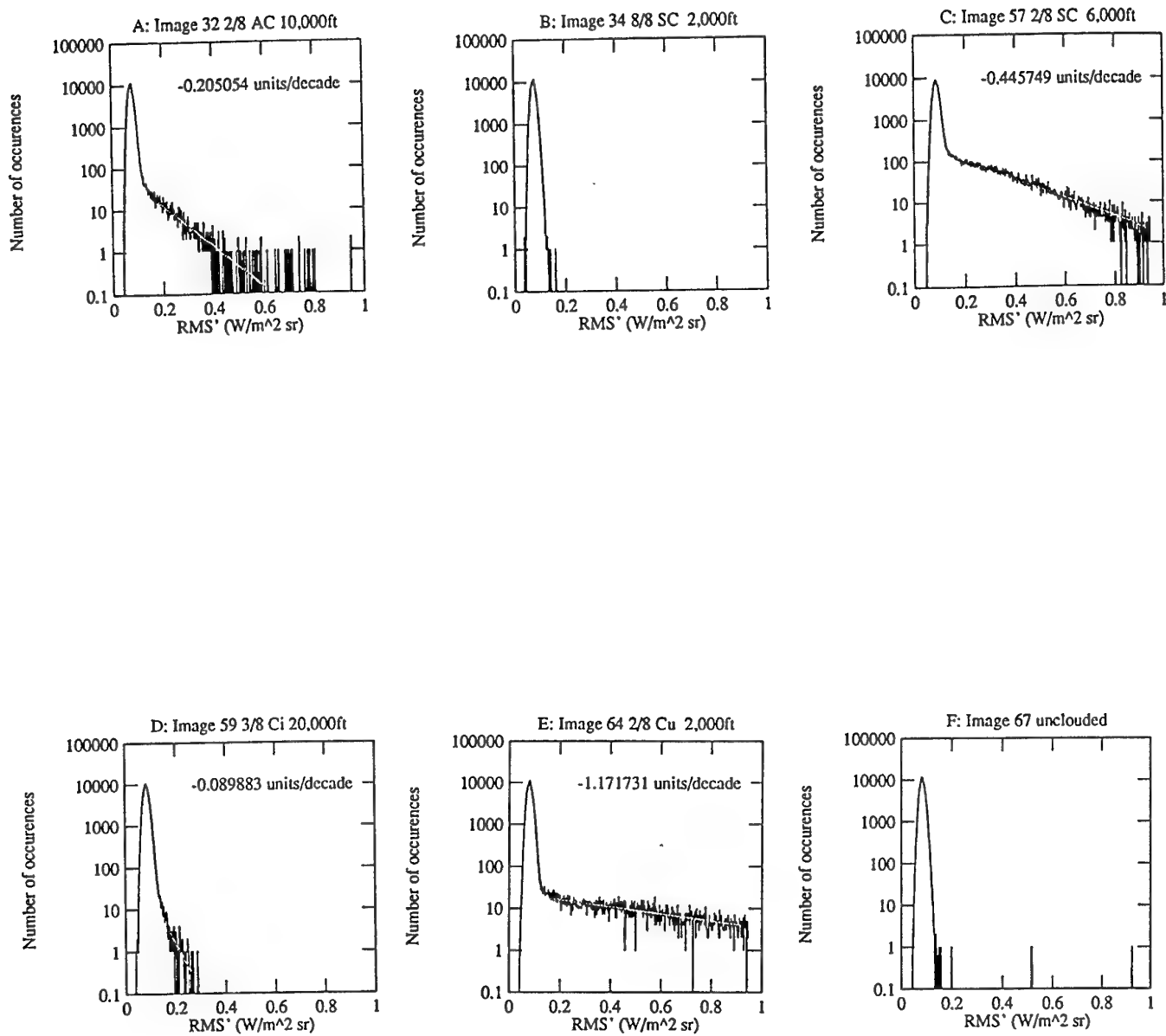
Figure 6.3: RMS' clutter histograms over entire cloud scanner 10 μm images for six different
dates and cloud heights.

Cloud type	slope lower	range upper
None	0.0	0.0
Ci	0.0	0.1
AC	0.1	0.3
Sc	0.2	0.5
Cu	0.5	-

Table 6.2:   Cloud classification using the RMS$'$ slope α. These values are for a partially clouded sky. A overcast sky has a RMS$'$ histogram comparable with a clear sky.

altocumulus type at 12000 ft. The meteorological conditions are the same but the slope is different. In general the classification of the cloud type is table 6.2. Only for altocumulus clouds and cumulus clouds an idetification problem exists.
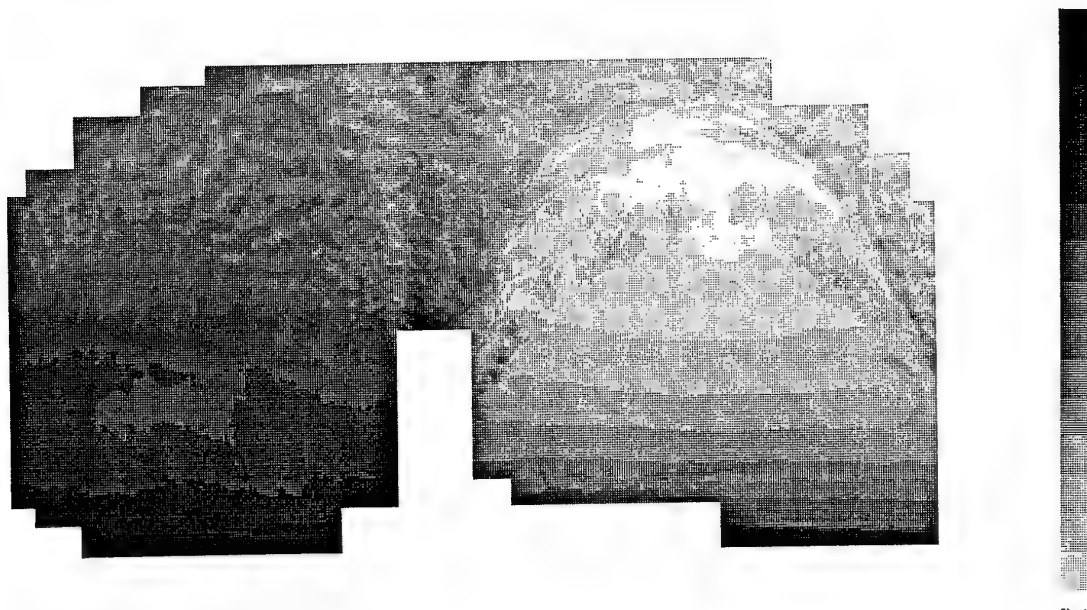
Figure 6.4:   Image recorded on April 16, 1993 15:45 CEST.

To study dependencies of clutter with elevation angle, we also calculated the distribution of sky and cloud radiance and of clutter values in elevation blocks. The spacing between the contours in a 2-dimensional clutter histogram (figure 3.10) gives us the slope of the tail of the RMS$'$ distribution qualitatively. For interpretation purposes (and quantification) it is better to analyse and to show the distribution of RMS$'$ per elevation as a histogram. These are presented for observations on
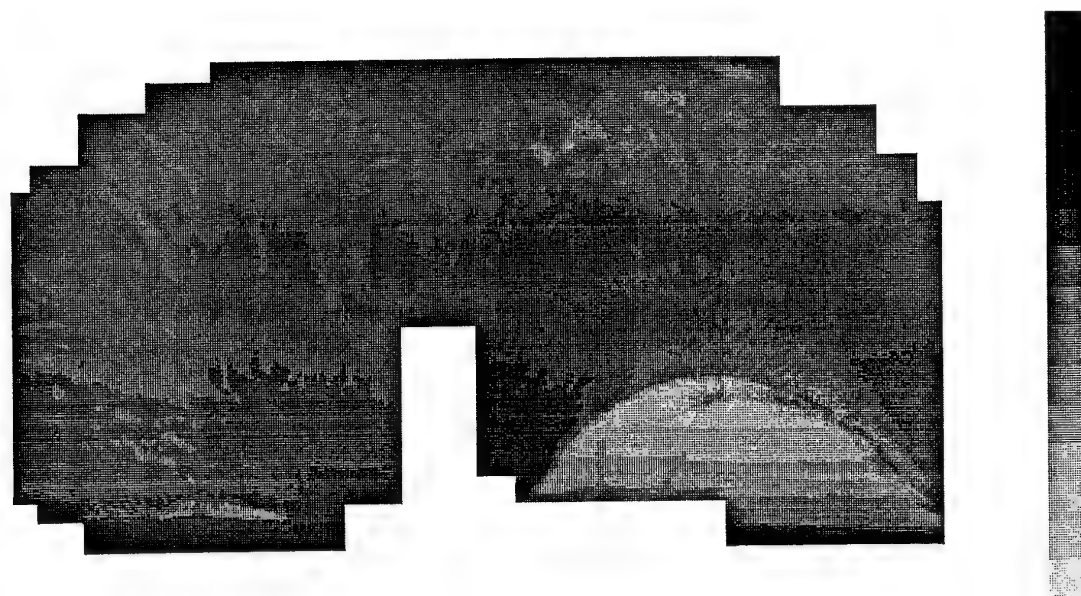
Figure 6.5:   Image recorded on April 16, 1993 16:00 CEST.

four different dates in figure 6.6. The elevation range is divided into nine parts. The central seven show the histogram of an elevation range of 9 degrees. The highest and lowest curves show the histogram in the remaining highest resp. lowest few degrees (each about 4 degrees wide). The x-axis gives the RMS$'$ (Watt m^{-2}sr^{-1}), and the y-axis gives a logarithmic value for the number of RMS$'$ occurrences (arbitrary units). Higher elevation data is presented higher in the figures, shifted 2 units on the y-axis. We have chosen to present four quite different sets of histograms. Relatively cloudy and cluttered scenes are given in figures 6.6.b and 6.6.c (images 83 and 86). Figure 6.6.d (image 91) gives a relatively 'empty' scene (with respect to clutter), while figure 6.6.a (image 60) is a case in between. The clutter tails in the diagrams are fitted with the procedure presented above. The labels at the right of each curve give the slope of the fit (α). Depending on the presence of clouds and cloud clutter at certain elevations it is clear from the figures that most clutter occurs at the lower elevations. This does not necessarily mean that this is also the case close to the horizon (elevation zero).

These examples show a change in the α-slope value with elevation (especially image 86). In general we have found that steeper slopes with a shorter clutter tail occur at higher elevations. This effect is observed in almost all distributions of Sc, Ac and Cu. Cirrus clouds (see e.g. image 91) in general have a very steep slope and the effect is not very clear. The explanation of these variations in slopes is already mentioned before. The first effect (of those three), the change in the difference in radiance

variation with decreasing elevation cannot cause the slope decrease as a result of the larger clutter values. With only one cloud type, the only difference in structure is the vertical structure of the cloud. This vertical structure can be seen in a partially clouded sky with low elevations. But in an almost completely covered sky this structure cannot be seen but the change in slope is also present there. The only clear explanation can be the variation in the observed pixel area. As explained earlier this can give a greater contrast between neighboring pixels and cause larger clutter values. This also means that higher clouds have larger clutter values (the observed area is larger) but that this effect is smaller than the difference in contrast causing for a overall lower clutter value.

6.4   Cloudiness

In the last paragraph is shown that the height of clouds can be determined by computing the RMS slope. Also the height can be calculated using the radiance distribution with elevation (see paragraph 6.2). This information can be used to distinguish between clouds and sky. An algorithm is developed to make this separation. This algorithm is mainly based on:

- RMS clutter values above 0.2 $Wm^{-2}sr^{-1}$ and less than the radiance of the intersection of the RMS' slope fit with the 0.1 occurrence. In figure 6.3.a this would be 0.75 $Wm^{-2}sr^{-1}$ and in figure 6.3.b 0.16 $Wm^{-2}sr^{-1}$.

- Radiance values which are more than 1.5 $Wm^{-2}sr^{-1}$ the minimum radiance at that elevation.

To make a better separation additional conditions should be met.

First the minimum and maximum radiance values with elevation are estimated. This results in an outline of the radiance distribution plots as in figure 5.4. The radiance at a specific elevation is compared with this minimum and maximum values. Due to the curvature of the curve a greater difference is needed at low eleavtions to mark a pixel as clouds than at high elevations. From 0 to 10 $^\circ$ a difference of 1.5 $Wm^{-2}sr^{-1}$ should exist, between 10 and 15 $^\circ$ 1.3 $Wm^{-2}sr^{-1}$ and for 15 $^\circ$ and upwards only 1.5 $Wm^{-2}sr^{-1}$. A big difference marks a pixel as cloud. RMS' values between 0.2 $Wm^{-2}sr^{-1}$ and the radiance at the intersection of the 0.1 occurrences axis of the RMS' slope fit are probably cloud edges. Pixels above these values are probably objects and values beneath these values are sky or dense clouds. Pixels with a low radiance difference and low RMS' values are marked as sky. Pixels with a high radiance and a low RMS' indicate a clouded area with a uniform distribution. These areas represent the dense centres of the clouds.
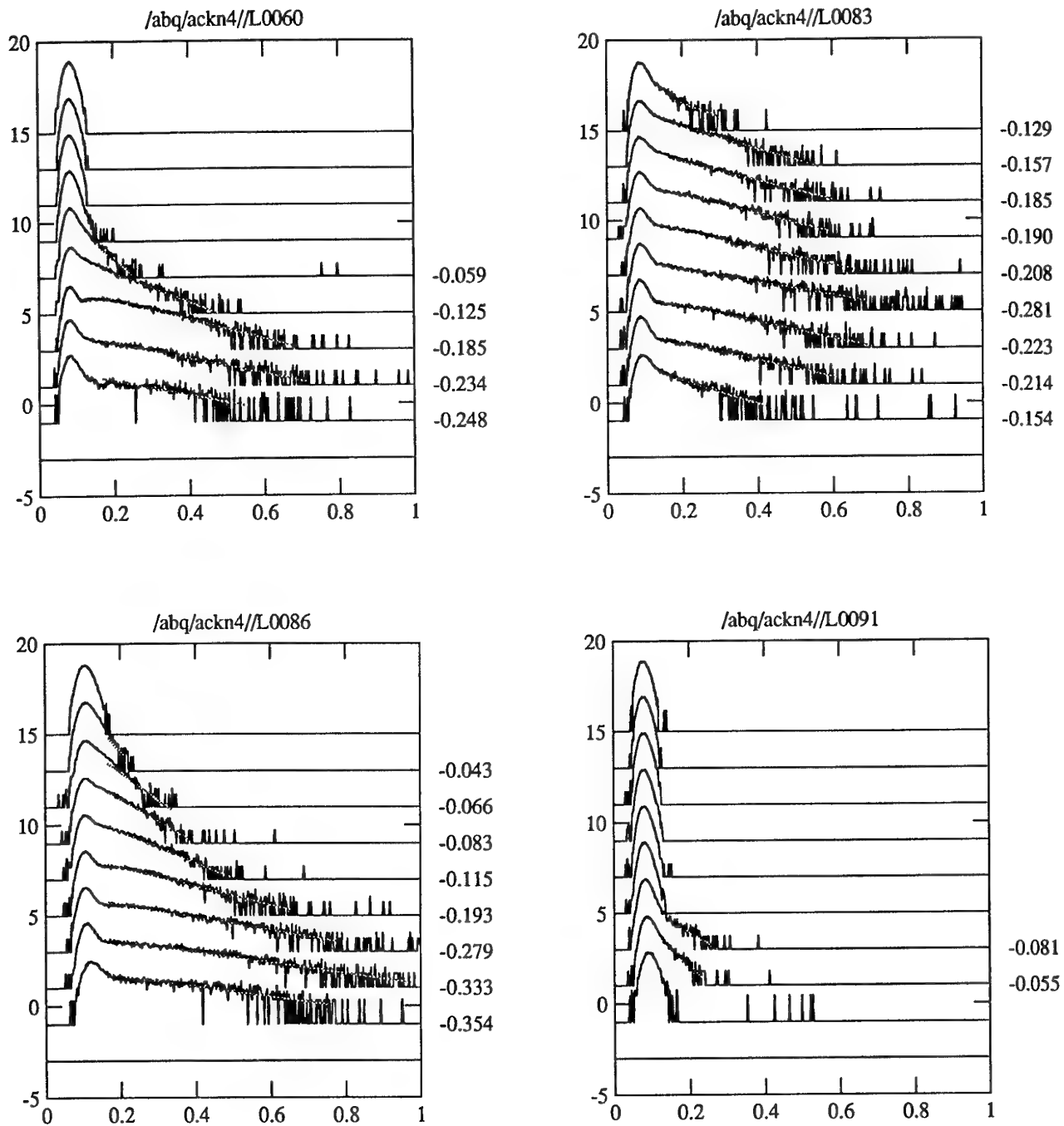
Figure 6.6: RMS' clutter histograms with elevation of four different Scorpio 10 μm images.

	< Limit	≥ Limit	≥ Limit+5	Limit > 0.8 * max. dif.
	clear sky			
Cloud pixels ≥ 3		cloud		
Cloud pixels < 3		sky		
RMS' > 0.2 Wm^{-2}sr^{-1}			cloud	
RMS' < 0.2 Wm^{-2}sr^{-1}				dense cloud

Table 6.3:   Classification table for clouds. Limit is de radiance limit for specific elevation (see text). Cloud pixels is the number of neighbour pixels that are marked as clouds. Radiance values that exceeds 80 % of the difference between the minimum and maximum are marked as dense clouds.

Table 6.3 shows the classification criteria. The image processing starts at low elevations. Each pixel has 4 out of 8 neighbour pixels that are already processed. The classification of these pixels is used for the classification of the pixel. After this first classification a part of the pixels is not identified as cloud or sky. These pixels did not meet all criteria needed for a classification. A second classification starts to classify these pixels. Potential cloud pixels with neighboring cloud pixels are marked as cloud pixels. One or more neighboring cloud pixels results in a classification as cloud. Five or more clear sky pixels results in a classification as sky. The sky classification overrules the cloud classification. The image is once scanned from top to bottom and once from bottom to top.

Figure 6.7:   Grey scale image of the radiance difference with the minimum radiance with elevation. White indicates low radiance differences. Black indicates high radiance differences. The white shape in the lower right is the blanking mask for the TNO-PEL tower. Measurement 86 on 4 May 1993 9:25 CEST.

Figure 6.8:   Image after cloud classification processing. Black indicates dense clouds, medium grey clouds and light grey open sky. Measurement 86 on 4 May 1993 9:25 CEST.

Figure 6.7 is the radiance distribution. Using the above mentioned criteria the pixels are classified. Figure 6.8 is the image after classification. Sky is light grey, cloud edges are medium grey and "heavy" clouds are black. The radiance distribution with elevation is in most cases a range of values between the empty sky curve and the fully cloud curve. The edges are not so dense as the centre of the clouds. The discrimination between edges and the centre is important to compute the cloud height using the radiance distribution. Only dense clouded pixel radiance should be used in this calculation. These pixels are known to have a radiance value that can be compared with that of an overcast sky. Cloud edges can have a lower radiance value. The radiance curve based on these dense clouded pixels indicates the cloud height. If the points can not be fitted with one prediction curve this is an indication more layers exist. In the RMS' distribution it is hard too distinguish between more layers. The RMS' slope is determinated by the lowest cloud layer. A second cloud layer has a radiance between the empty sky and the first cloud radiance. Only looking at the radiance minimum and maximum curves could result in the wrong identification as edges of clouds. The method based on the radiance values of dense clouds can identify two layers.

The cloudiness classification program operates well. The detection algorithm can even classify cirrus clouds. In figure 6.9 5/8 Ci at 22000 ft exists. Figure 6.10 is the result after cloud classification. It should be noted that the radiance range grey scale used to show the difference in values image 6.9 is 4 times that of figure 6.7. Ci clouds have only a small contribution to the radiance. Lowtran

calculations also indicate this (see figure 4.4). The arc shape of the Ci clouds is due to the cartesian projection of a half hemisphere.

Comparing the infrared image and the result after processing show little to no areas which are wrongly identified. The estimated cloudiness is difficult to compare with meteorological data due to the changing cloud conditions. Figure 6.4 and 6.5 show this. The octa numbers of the meteorological service are an impression of the observer during a certain time. The cloud scanner records only a few images. One large cloud just above the cloud scanner will result in a high octa number. This can result in a wrong impression of the cloudiness. Continuous operation of the cloud scanner can overcome this. Also a weight factor can be used. Low elevations have a higher weight factor. The clouds detected are at a greater distance and one pixel represents a greater area (in m^2) of the cloud.
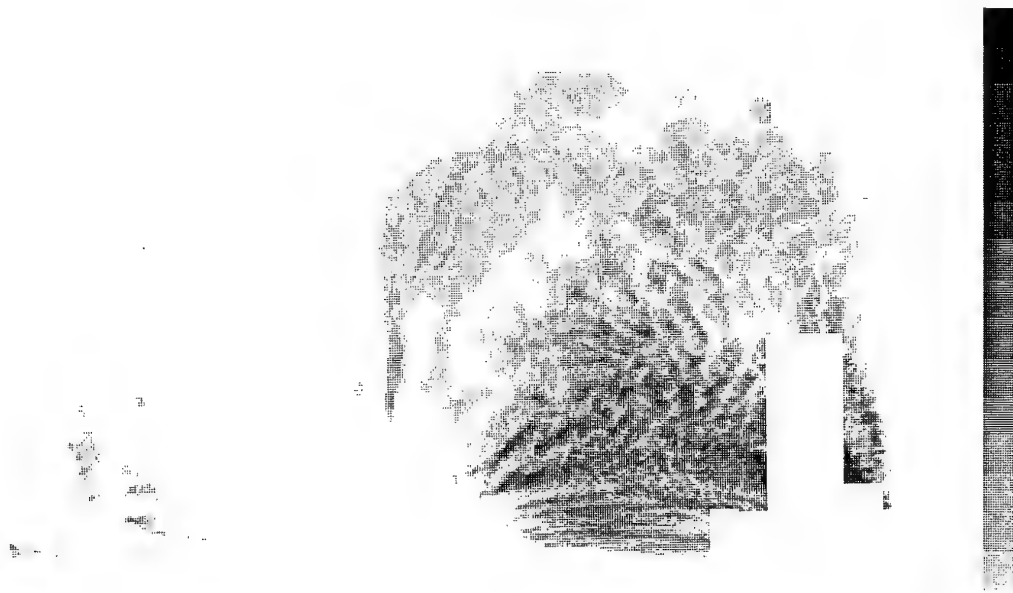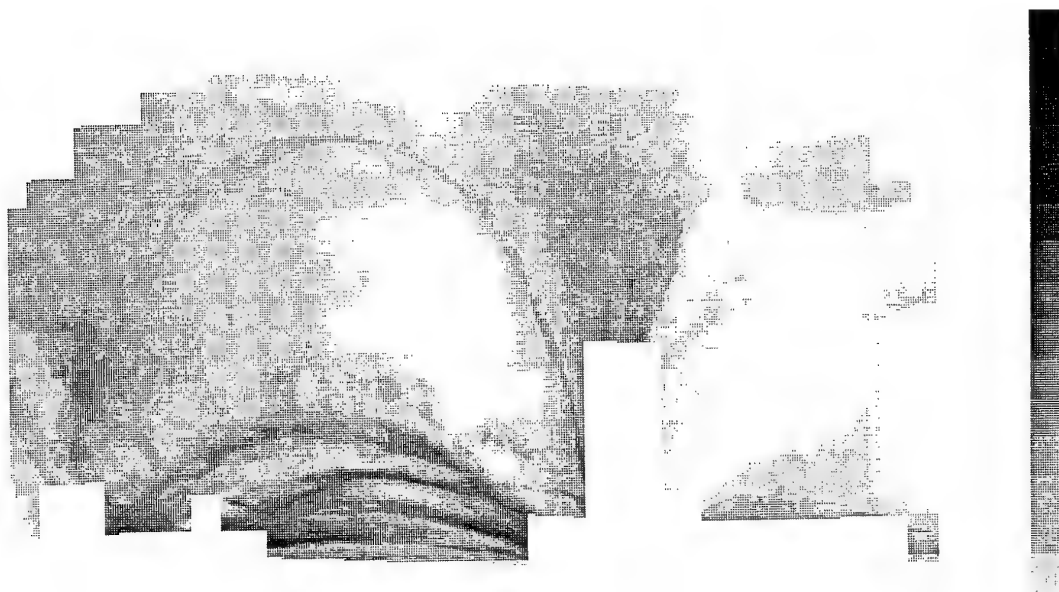

Figure 6.9:   Grey scale image of the radiance difference with the minimum radiance with elevation. White indicates low radiance differences. Black indicates high radiance differences. Measurement 84 on 28 April 1993 12:53 CEST.

6.5   Detections and objects

The detection with infrared is only possible when a contrast between the target and the background exists. We take a subsonic rocket with a speed of 300 m/s and an area of 0.3 m^2 as target. The radiance of this rocket is 50 Wm^{-2}sr^{-1} at an ambient temperature of 280 K in the 10 μm band.
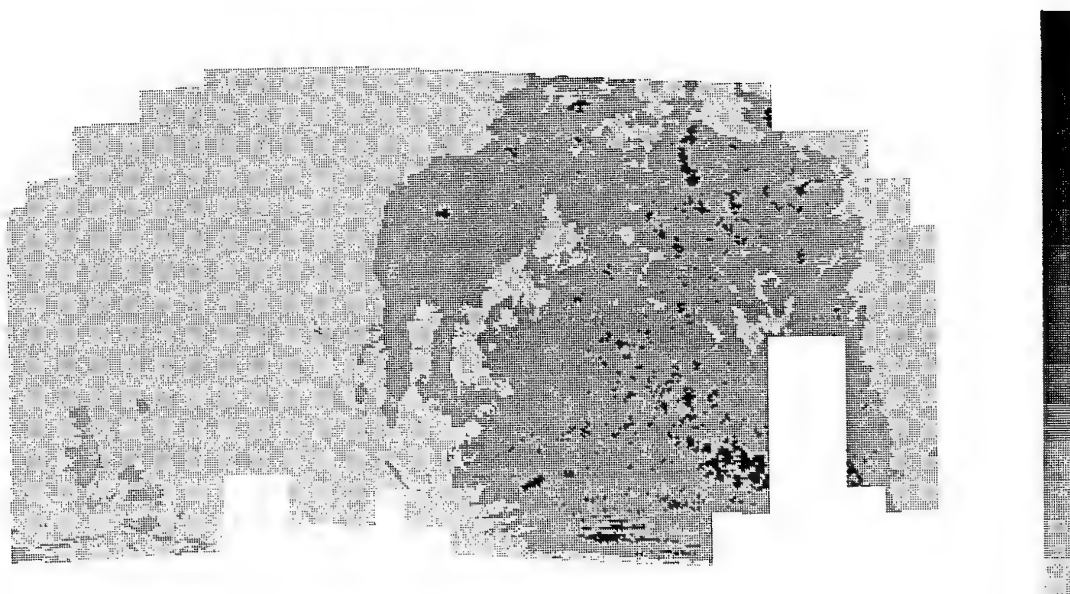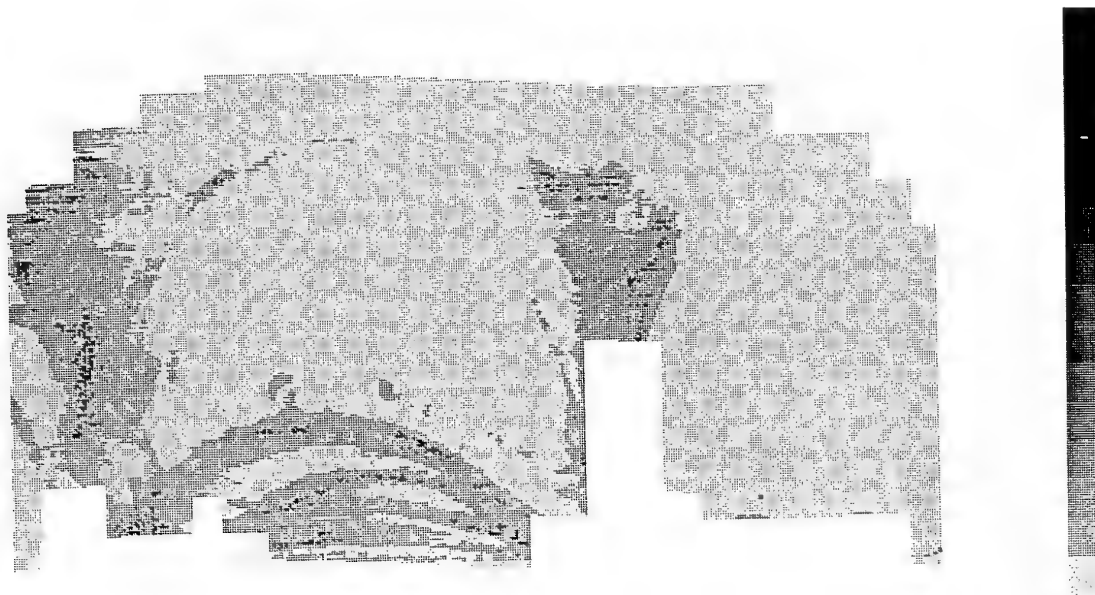
Figure 6.10:   Image after cloud classification processing. Black indicates dense clouds, medium
               grey clouds and light grey open sky. Measurement 84 on 28 April 1993 12:53
               CEST.

The radiance in a pixel with objects is:

$$I_{target} = \tau \frac{A}{\alpha^2 R^2} L_{target} + \frac{\alpha^2 R^2 - A}{\alpha^2 R^2} L_{background} + \frac{A}{\alpha^2 R^2} L_{foreground}$$

In this equation A is the area of the object, α is the IFOV, R is the detection range, L_{target} is the
target radiance, τ the transmission through the path, $L_{background}$ is the background radiance of the
sky and $L_{foreground}$ is the emission of the air between the detector and the object. The contrast
between a pixel with a object and without one is:

$$I_{object} = \tau \frac{A}{\alpha^2 R^2} L_{target} - \frac{A}{\alpha^2 R^2} L_{background} + \frac{A}{\alpha^2 R^2} L_{foreground}$$

The foreground contribution will be between $L_{background}$ and zero. A $L_{foreground}$ of zero will result
in a minimum contrast. For a horizontal path and a long range > 5 km this contribution will be in
the order of $L_{background}$. Assuming $L_{foreground} = L_{background}$ the equation can be simplified:

$$I_{object} = \frac{A}{\alpha^2 R^2} \tau L_{target}$$

The contrast which can be detected depends on the NEI of the system and the S/N. The contrast
itself is determinated by the IFOV (α), the range (R) and the transmission (τ).

The cloud scanner has an IFOV of 0.8 mrad, a radiance noise (NEI related) of 0.11 $Wm^{-2}sr^{-1}$ and a σ of 0.015 $Wm^{-2}sr^{-1}$. In an empty sky pixels with a RMS value of > 0.2 $Wm^{-2}sr^{-1}$ are objects (see figure 6.3). The extra radiance contribution in one pixel of a cell that results in a RMS' of 0.2 $Wm^{-2}sr^{-1}$ is 1 $Wm^{-2}sr^{-1}$. The radiance difference is calculated using :

$$\sqrt{\frac{\sum_{i=0}^{i \leq n}(V_i - \mu)^2}{n}} = \Delta$$

$$\sum_{i=1}^{i \leq n}(V_i - \mu)^2 + 1\delta^2 = n\Delta^2$$

In these equations n is the number of pixels in a cell (48), μ is the average value of the cell, δ is the difference in a pixel needed to obtain a RMS' of Δ. and V_i the value of the ith pixel. We use LSB values in this calculation. 1 LSB corresponds with 0.05 $Wm^{-2}sr^{-1}$ using the absolute sensitivity and 8 times ADC gain. If $n >> 1$ then $(n - 1) = n$, $\sum_{i=1}^{i \leq n}(V_i - \mu) = (n-1)NEI + \frac{\delta}{n-1}$. The NEI is 2 LSB. The presence of δ is needed to incooperate the change in average (μ) by the extra radiance contribution. The equation becomes:

$$n(2 + \frac{\delta}{n})^2 + \delta^2 = n\Delta^2$$

Again using $n >> 1$.

$$\delta^2 + 4\delta + 4n - \Delta^2 n = 0$$

A RMS' of 0.2 $Wm^{-2}sr^{-1}$ is 4 LSB. $\Delta = 4$ results in $\delta = 22$ LSB (1 $Wm^{-2}sr^{-1}$).

The range at which this target can be detected using only the RMS calculation is 6 km ($\tau = 0.5$ and $L_{background} = 30$ $Wm^{-2}sr^{-1}$). The scanner is too slow to use a temporal processing. The advantage of temporal processing is that the time development of a pixel can be followed. A smaller difference is sufficient to be classified as a possible target. The time development of the pixel discriminates between noise and targets. For this kind of processing a $\delta > NEI + k\sigma$ is enough. $k = 5$ results in δ is 0.185 $Wm^{-2}sr^{-1}$ or 4 LSB.

The transmission is an important factor in the contrast. This transmission can be calculated using the horizontal path mode in lowtran. For sea-skimmers this is alright but for objects at higher elevations at long ranges a difference in transmissions exists. It should also be noted that the transmission for

a horizontal path depends stronly on the atmospheric profile of the first 10 m. A good description of this 10 m is needed for correct transmission calculations. We will point out that for objects with a slant path to the observer also a good description of the first km of the atmosphere is needed.

Figure 6.11 shows the transmission for a object at 5, 10 and 20 km. The calculations are made with lowtran using the midlatitude model. The grey lines are based on the maritime aerosol model and the solid lines on the no-areosol model. High elevations have a transmission arround 80 %. At low elevations a significant difference exists. At 20 km the transmission using the no-aerosol model is 0.4 while the maritime model result only in 0.1. The same is true for the midlatitude summer model (see figure 6.12). At high elevations the transmission is 0.6 for all the aerosol models. At 0 ° a wide range of transmission values exists. This figure shows the importance of well known atmospheric profiles espacially for the first km. The transmission in the no-aerosol model is 0.017 and in the maritime model 0.004. A difference of a factor 4. The height of the object is important for the transmission. A target at 20 km at a height of 3000 ft has a more then 4 times higher (i.e. better) transmission than a target at sea level.
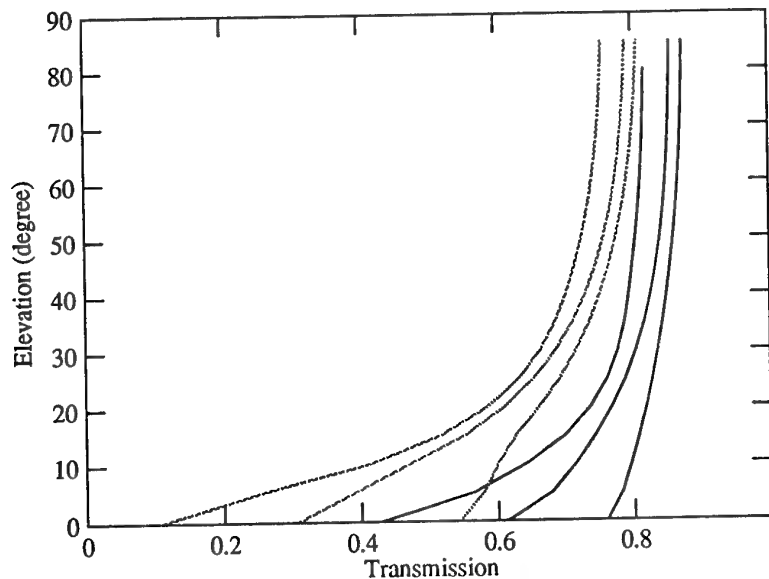
Figure 6.11:   Transmission predictions of lowtran based on the mid-latitude winter model. Solid curves are calculations with the no-aerosol model and grey lines with the maritime model. The two sets of three curves are the transmission for a object at 20, 10 and 5 km (from left to right).

The water density is a very important factor in the transmission calculation. In chapter 5 it is shown that this contribution is overestimated in the standard lowtran models at low elevations. For a worse scenario the lowtran calculations can be used but for correct transmissions better model 3 can be
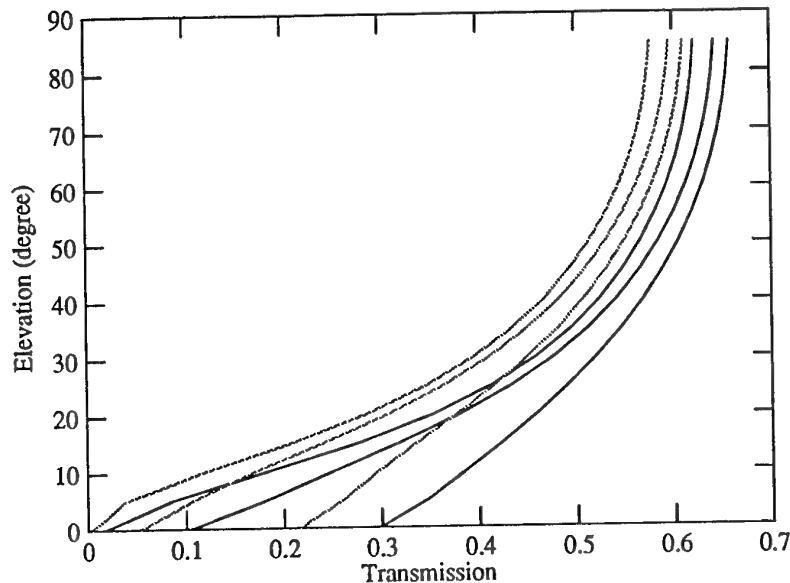
Figure 6.12: Transmission predictions of lowtran based on the mid-latitude summer model. Solid curves are calculations with the no-aerosol model and grey lines with the maritime model. The two sets of three curves are the transmission for a object at 20, 10 and 5 km (from left to right).

used. The measured sharp decrease in radiance with elevation indicates a more opaque atmosphere (higher transmission) than the lowtran calculation uses. The no-aerosol calculation resembles these conditions. Figure 6.12 shows the difference in transmission between the maritime model and the no-aerosol model. This is relevant for long range detection of airplanes by ships and vice versa using infrared detectors.

7   CONCLUSIONS

The cloud scanner Scorpio is used to obtain a large data set of nearly all-sky infrared images. The images are recorded in different meterological conditions. In this report a description of the system and the recordings are given. Statistics were built up from a large image database was analyzed.

The data were analyzed at a Masscomp 5500 unix computer with specially developed processing software. The raw 12 bit data time sequences are first pre-processed after the observations, resulting in two-dimensional images. Images are then masked and unwanted low elevation areas such as buildings not related to the sky and clouds are removed in this masking procedure or blanking pre-processor. The remaining data are analysed for the clutter content. RMS clutter calculations are obtained in cells with a dynamic average background (i.e. local to the point of interest and hence the average may exceed the cell limits). This method results in clutter metric values for the entire image as well as for (smaller) selected image areas (e.g. elevation ranges).

The cloud scanner Scorpio can be used to determine cloud height and cloudiness. The clutter in an image is largerly caused by clouds. Knowledge of the expected clutter content is important for the evaluation of detection algorithms. This knowledge can also be used in the algorithm itself to adapt the threshold level. Good use of it will reduce the processor load.

A model is made for the first 5 km of the atmospheric profile. In this model the "no-aerosol" model in lowtran is used. The radiance predictions based on this model have a good match with the measured curves. The influence of the water density is less than in two other described models. Better radiance predictions are made for non horizontal path radiances and transmissions using this model. The transmission of long range targets strongly depends on the water density. For correct detection range predictions a good description of the atmosphere is necessary.
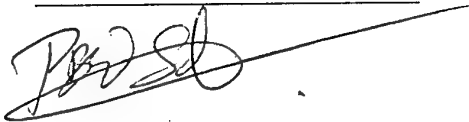
The main impact of this research is the improvement of the clutter metric that was used by TNO-FEL during the IRSCAN evaluation trials in 1992. For future IRST validation trials even more accurate clutter metrics can be build based on this information. Elevation profile analysis led to first order estimates for the clutter behaviour near the horizon with respect to higher elevations. These data can also be used in background modelling of the IRST models for performance analysis.

8   ACKNOWLEDGMENTS
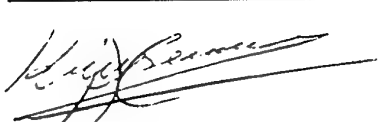
REFERENCES

[1] W.R. Reynolds.
Toward quantifying infrared clutter.
In *Characterization, Propagation and Simulation of Infrared Scenes*, pages 232–240, Orlando Florida-USA, April 16-20 1990. SPIE, Vol. 1311.

[2] P.B.W. Schwering.
Characterization of infrared cloud background clutter.
In *Characterization, Propagation and Simulation of Sources and Backgrounds II*, pages 311–322, Orlando Florida-USA, April 20-22 1992. SPIE, Vol. 1687.

[3] J. Winkel.
Beschrijving van de wolkenscanner.
Technical Report IR 1987-54, FEL-TNO, 1987.

[4] Li Z. R. and M.J. McDonnell.
Atmospheric correction of thermal infrared images.
Int. J. Remote Sensing, 9(1):107–121, 1988.

[5] et al. F.X. Kneizys.
Users Guide to LOWTRAN 7.
US Air Force Geophysics Laboratory, AFGL-TR-88-0177, 1988.

[6] P.V. Coates.
Detection and classification of single airborne targets over a wide field of regard.
In 54th *AGARD AVP Symposium on electro optical systems*, Athens-Greece, 1987.

P.B.W. Schwering
(Project leader)

A.C. Kruseman
(Author)

OPERATIONAL NOTES

A.1 External noise

During operation it appeared that the Scorpio system is sensitive for external Electro-Magnetic fields. The signal from the 4 μm detector is also disturbed by the motor used to rotate the mirror. The 10 μm signal is not hampered by the motor. Two other sources of EM fields that give extra noise are known. The first one is the FELSTAR radar system. This system is never pointed towards the cloud scanner system but during operation of the FELSTAR noise bands appeared in the image of the cloud scanner. Figure A.1 shows the characteristic bands of noise. These bands consist of a slightly higher RMS' value and have always the same duration. The other known noise source is the HF antenna placed in September 1993 above the cloud scanner. This obscures a large part of the sky and made it necessary to use a much larger blanking mask. The operation of the HF antenna gives rise to a large noise contribution (see figure A.2). The RMS' is under normal conditions about 0.1 Wm^{-2}sr^{-1}. While the HF antenna is broadcasting the RMS' rises to 0.3 Wm^{-2}sr^{-1}. Also a satellite disk at 20 meter distance of the scanner can give rise to additional noise. But both systems have never been operated simultaneously.

A.2 Sun

The hot solar surface of 6000°C causes the detector to clip (saturate). In the 4 μm wavelength band this results in incorrect values in the next pixels (see figure A.3). In the 10 μm wavelength band this also occurs but at a much smaller scale. To avoid this the reference bar is used to obscure the sun. Sometimes the sun can be reflected on the cloud scanner and be projected on the reference bar. The reference bar is used to calibrate the detector and the sunspot can corrupt this calibration. The line will be darker than it should be.

A.3 ADCs

Two AD12FA ADCs are available in the Masscomp computer system. The AD12FA can digitize a signal of 1 Mhz in 12 bits. The input range can be set from –5V to +5V or from 0V to 10V. An internal gain of 1, 2, 4 and 8 times is also available. Both ADC have been tested. One ADC does not correctly digitize the signal. The 4th bit which represents the $2^4 = 16$ value is set too late. The
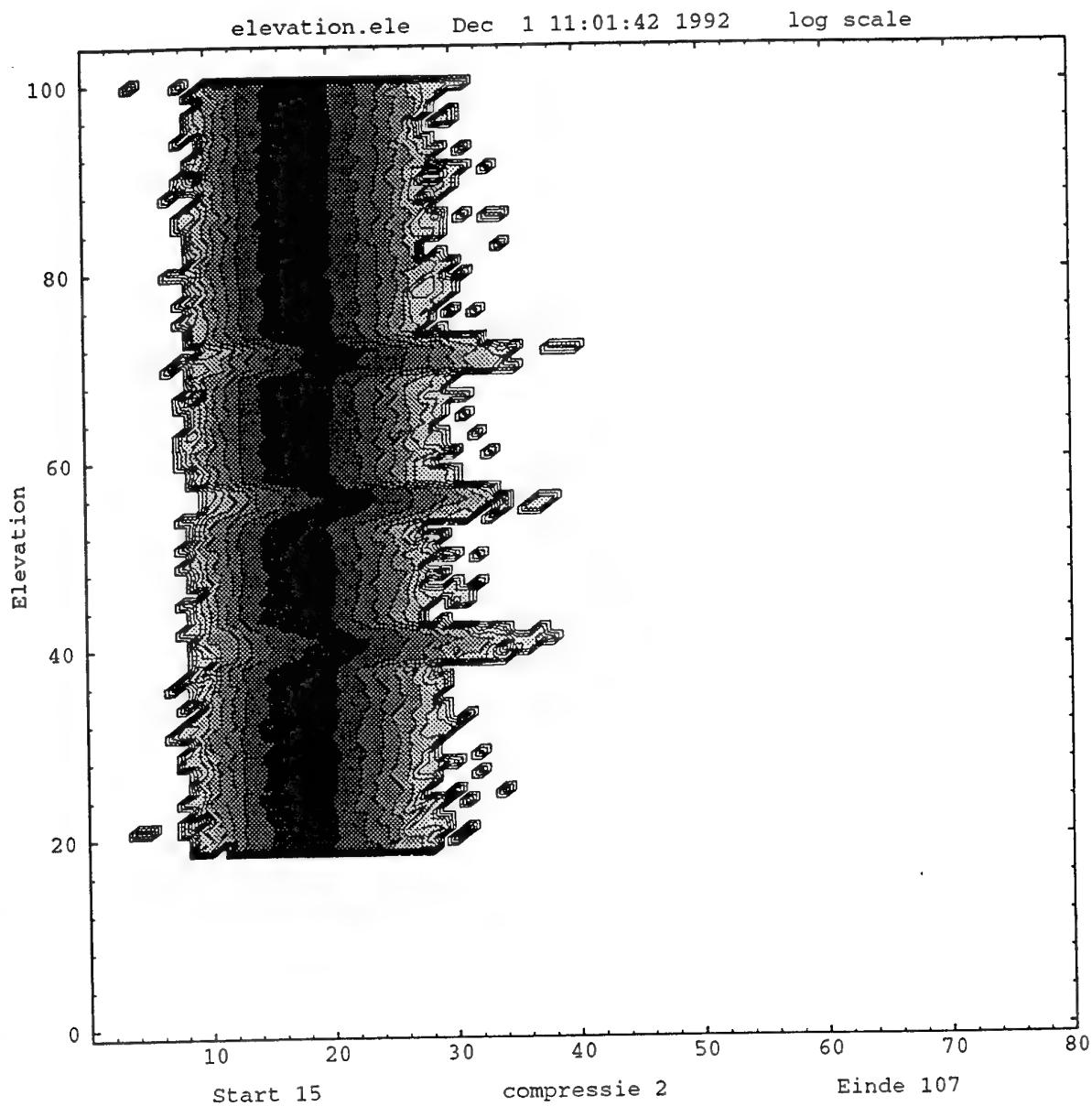
Figure A.1: RMS' distribution with elevation. Elevation in units of 0.9° starting at −18°. RMS' is in units of 0.02 $Wm^{-2}sr^{-1}$ starting at 0.2 $Wm^{-2}sr^{-1}$. Three times a small increase in RMS' occurs. Inspection of the image shows three bands. The time duration of a band is 3 seconds. These bands occur only when also the FELSTAR is in operation. Image 22 at December 1, 1992.

/abq/ackn4//L0110
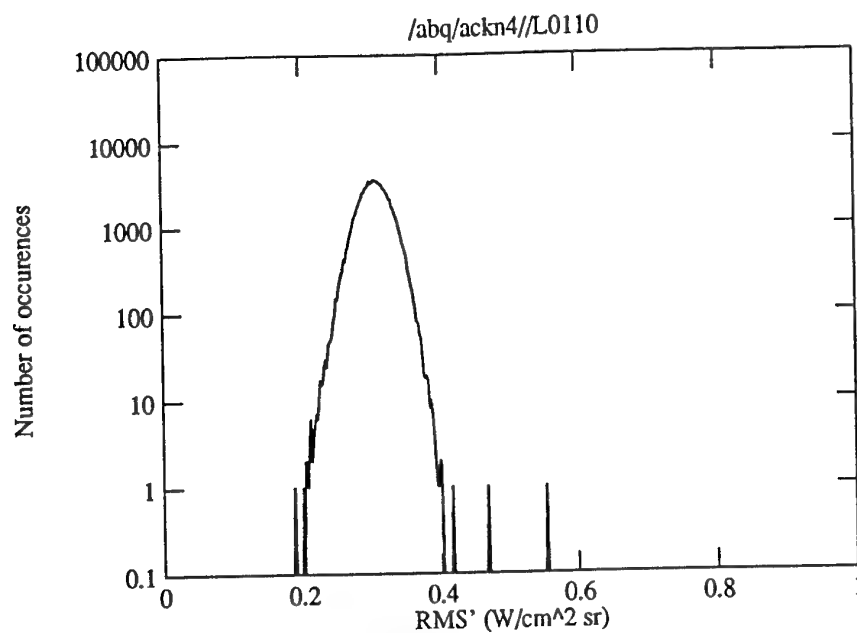
Figure A.2:   The RMS' distribution of an image made while the HF antenna was broadcasting.
Image 110 of 22 September 1993.
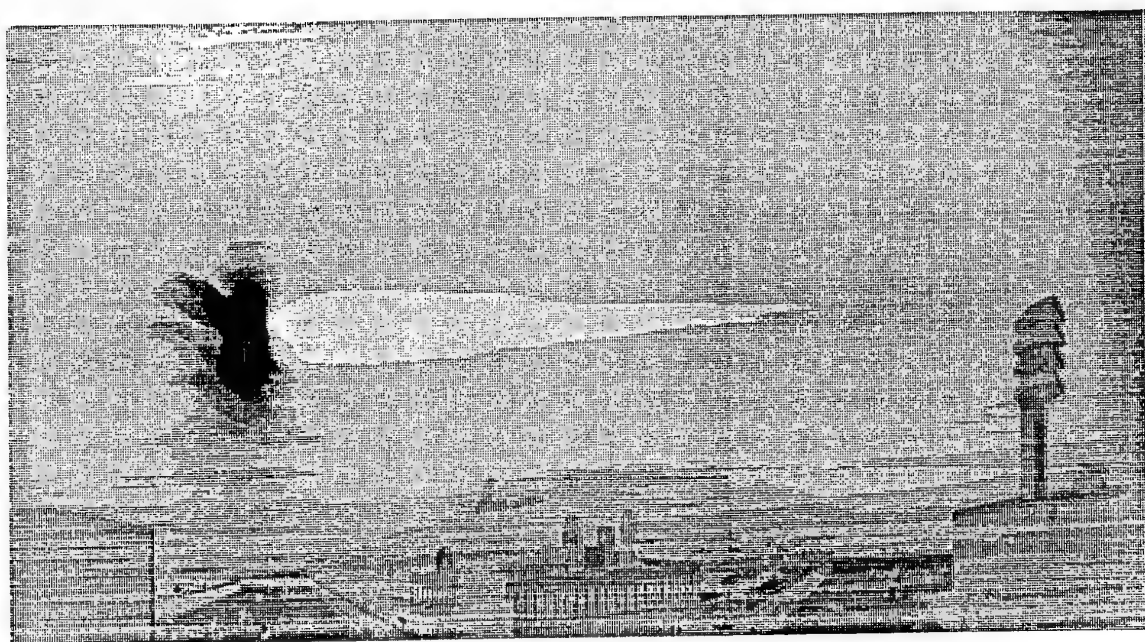
Figure A.3:   4 μm image of the sun. The direct radiation causes incorrect values. The detector
needs about half a line scan (0.02 seconds) to restore.

counting for this ADC is 9, 10, 11, 12, 13, 14, 15, 0, 17, 18, 19, $\cdots$, 30, 31, 16, 32. Figure A.4 shows a crosscut in elevation of an image. The values for which modulo 16 are zero show a decrease of 16. This is no noise and it repeats in every image. The other ADC operates correctly. The internal gain of the ADC, which can be set to 1, 2, 4 and 8 times, is also checked and is lineair.
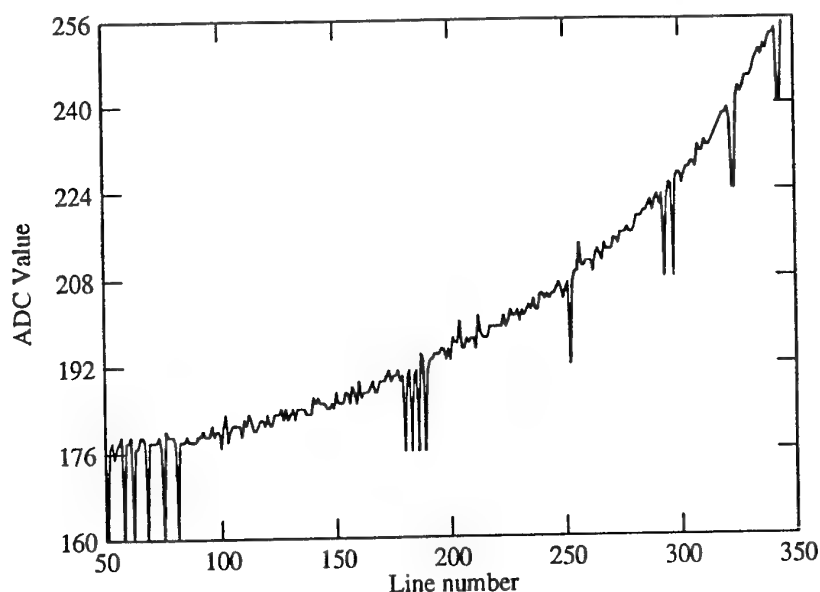
Figure A.4:   Crosscut of an image in elevation. Values of modulo 16 are zero where the ADC gives an incorrect value which is 16 too low. The second ADC does not have this problem.

A.4   Correction of images

The cloud scanner should be positioned water-level. Only in this case a line in the image is at a constant elevation (neglecting the small change due to the spiraling mirror). To do this the cloud scanner can be adjusted in height. But this is only possible when the cloud scanner is outside the weatherproof box. The cloud scanner will have a slight tilt in the box. Also the box is positioned on a rotatable platform which itself is not at water-level. A line should have a constant elevation but it does not. The result of these tilts is that there are differences in radiance at the same line of the images. This effect is most significant at low elevation because of the changing steepness of the radiance curve. Figure A.5 is a radiance image obtained at 11 May 1993 with a clear sky. The grey levels are spaced 16 LSB. A line in the images at low elevations has three different grey levels. Indicating at least a difference of 32 LSB in radiance values.

Figure A.6 shows both tilts. The difference between both tilts is that the tilt caused by the platform is always in the same direction (for the outside world) and the tilt of the cloud scanner rotates with the platform. In an image for a specific pixel position the tilt caused by the cloud scanner is always the same while the tilt caused by the platform changes when the platform is rotated.

The shift can be corrected by positioning the total system water-level or by correcting the images for these tilts. It is very difficult to correct the shift of the platform itself. The last option is chosen and the images are corrected by the data processing programs.

The shift can be corrected with the following equation:

$$line\_shift(\phi) = amp\_shift * sin(\phi + \rho + \beta)$$

The $line\_shift$ is the shift in lines at azimuthal pixel position ϕ. ρ is the phase shift for the rotation of the platform (only for the shift by the tilt of the platform), β is a constant phase shift which should be determinated and amp_shift is the amplitude of the shift. For both tilts these values should be calculated. A simplified solution is used by measuring the β and the amp_shift at two different orientation of the platform (two different ρ's). We use the two outmost operational positions of the platform for these measurements. A linear displacement is assumed. For the correction the following equations are used:

$$\alpha = B_{min} + \frac{(A_{min} - B_{min})}{(A_{mask} - B_{mask})} * (mask - B_{mask})$$

$$line\_shift(pixel) = 10 * sin(pixel * \frac{2\pi}{467} - \alpha) + 10$$

A and B are calibration measurements. The min subscript is the pixel position with the maximum downward shift and $mask$ is the position of the mask (representing the orientation of the cloud scanner). The value 467 is the number of pixels in an image (5600/12). An additional number of 10 lines are added, hence the shift is always positive. The low part of the image contains buildings and is blanked. The shift is always to lower elevations so the image still fits within its original 512x512 size image.

The scanning mirror of the cloud scanner is positioned at 2.20 m above the roof level. The horizon is estimated by checking the position of objects on the roof at 2.20 m. Due to the tilt the position changes with the orientation of the cloud scanner. The horizon is at line 70 in a 500 lines corrected image.

Also the images have a signal contribution with a frequency of 50 Hz and an amplitude of 7.5 LSB. This contribution shows clearly at high elevations. This is artificial. Rotating the platform does not change the wave pattern. This wave pattern is not present when operating with a closed scanner box

so it is not noise of the 50 Hz outlet voltage. It can be the top mirror of the system which radiance gives a small contribution but it can easily be another part of the system. The presence of the wave pattern is clear at high elevations but it is hard to tell if it is also present at low elevation. At low elevations the influence is small compared with that of the tilt of the system. This wave pattern is compensated with :

$$value_{new}(pixel) = value_{old}(pixel) + 7.5 * sin(pixel * \frac{2\pi}{467} - 2.4047)$$

Both these corrections are only necessary to correct the radiance images. The RMS' image is not affected by these distortion because they have a low frequency (same order as line frequency).

A corrected image is shown in figure A.7. The image is improved at low elevations. A constant elevation has less variation in grey scales and thus in radiance. The correction results not in a real improvement at high elevations. The highest radiance occurs in the centre of the original image. After the correction the lowest radiance occurs in the centre. The correction is not fully correct. Because of the unkown source of the 50 Hz contribution it is difficult to adapt the correction. In general an image with both corrections is at high elevations slightly better than images with only the tilt correction.

The correction is important for a correct radiance distribution at low elevation. The distribution in figure A.8 is uncorrected. At low elevations a wide range of radiances occur. The distribution in figure A.9 is obtained after correction. The radiance distribution is a line with a narrow distribution. The line is still to broad compared to the NEI but there is a significant improvement. As already indicated the low elevations improve most. In a block of 0.9° the range of radiance values changes from 80 LSB to 30 LSB.

A.5   Horizontal shifts of the image

Sometimes horizontal shifts occur in the image. Figure A.10 shows an example of these shifts. The image is generated using a function generator. The reason for these shifts is not quite clear. The imager program uses only the pixel synchronization and not the line synchronization. The errors are cumulative and are caused by missing pixel synchronization pulses. It is possible that they are generated by the wind or by trembling of the system by the wind. It can help to fix the box but this does not always work. Another possibility is a problem with the lubrication of the rotation mechanism. Sometimes a few lines at low elevations show the same image indicating a problem with the spiraling movement of the mirror. This happens only at very low elevations, the first 50 lines of a image, and can be caused by for example dirt in the mechanism. These shifts are clearly
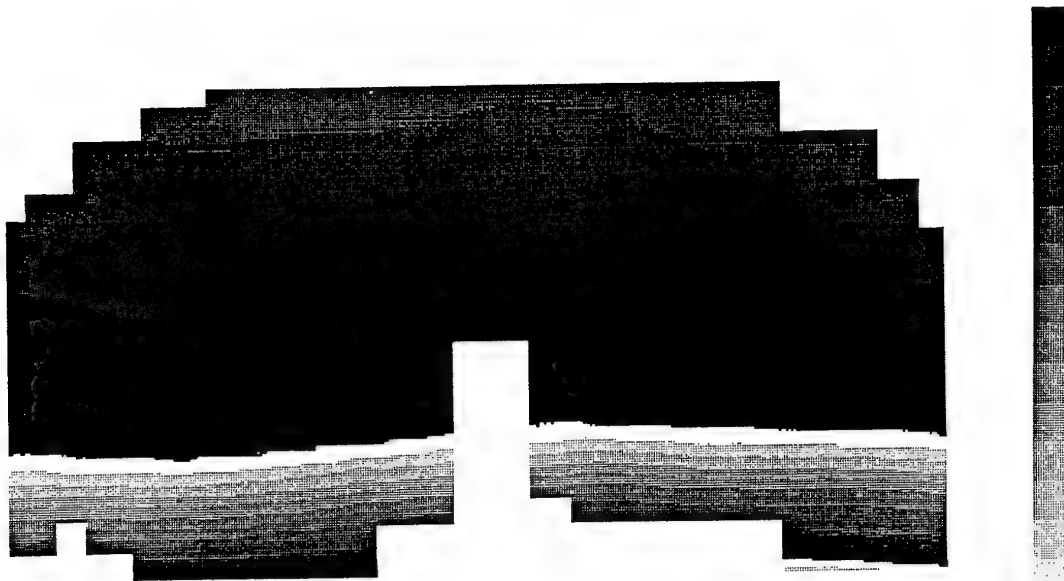
Figure A.5: 50 Hz wave pattern at high elevations and 25 Hz wave pattern at low elevations caused by a tilt of cloud scanner. The 16 grey levels are spaced 16 LSB to show the effect better. The radiance values have a range of 600 LSB. The same grey levels can indicate different radiance values. The black level at the bottom of the images has a 256 LSB higher radiance value than the black level in the centre of the image. Measurement 89 at 11 May 1993.

Tilt cloud scanner

Too low

Too low   Too high   Too low   Too high

Tilt platform

Too low   Too high   Too low   Too high
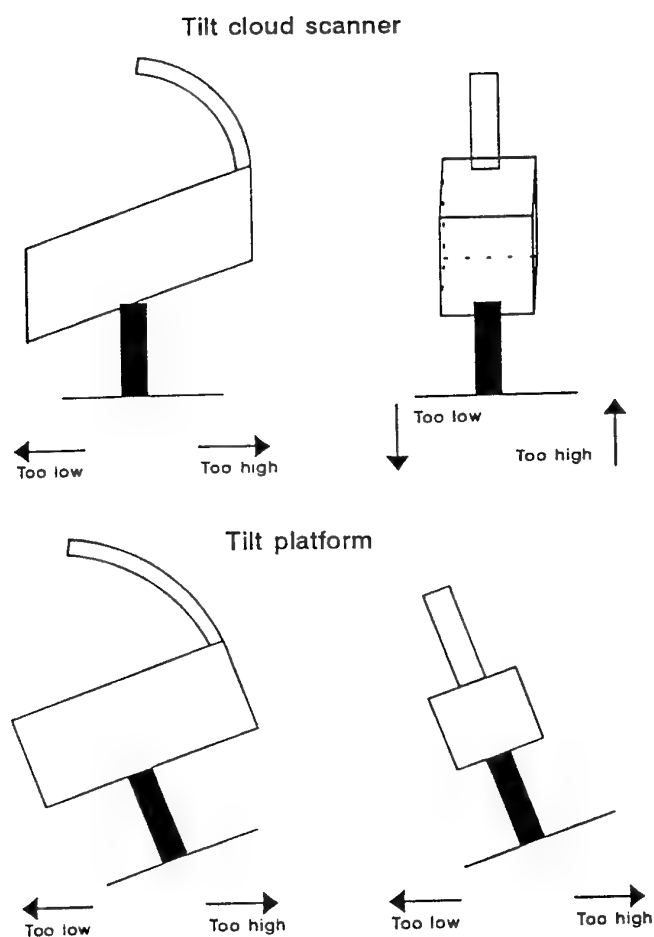
Figure A.6:   Two possible faults by non water-level operation. Top: The cloud scanner is not positioned water-level inside the mounting device. Bottom: The mounting device for the cloud scanner is not water-level.
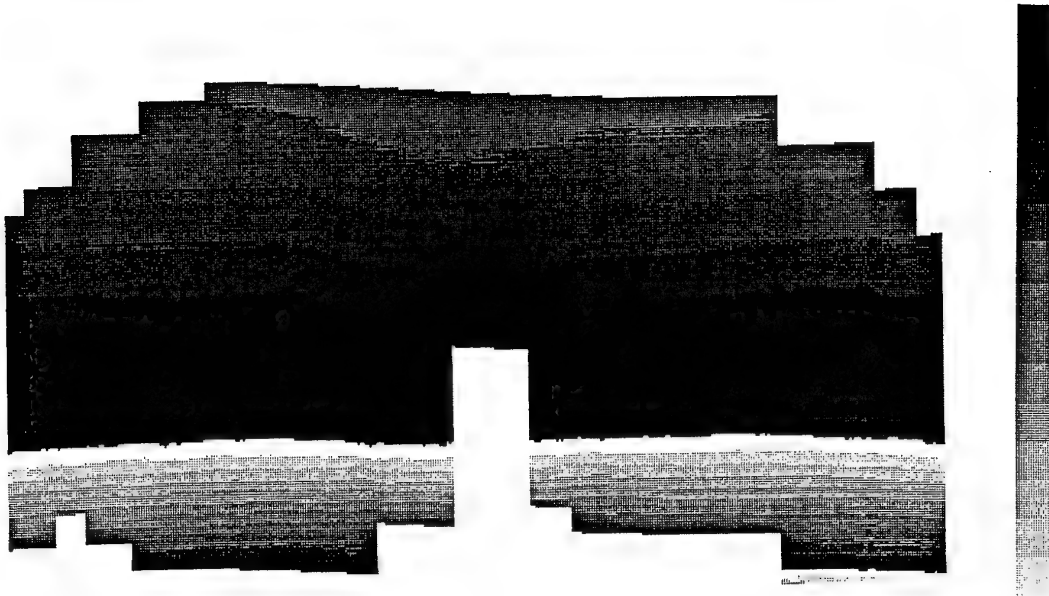
Figure A.7:   Corrected image of figure A.5 for tilt and 50 Hz contribution

recognizable in the images and apart from a complete revision of the system the easiest solution is just to make another image.

These shifts are not caused by a processor overload or IO overload of the computer system.

A.6   Vertical lines in image

In each image vertical lines of one pixel exists with values differing from the following pixels. These lines repeat at an interval of 7 lines and are caused by the pixel synchronization pulse of the scanner. The pixel values are a few LSB too high or too low (typically about 3 LSB for absolute range 8x gain). These lines are only distinguishable in parts of a images with a uniform distribution. These lines have only a small influence in the RMS' calculations. A cell of 4x12 will contain at most 2 of these vertical lines. The RMS' will be $\sqrt{\frac{3^2}{6} + \frac{5*2^2}{6}} = 2.2\text{LSB}$ in stead of 2 LSB.
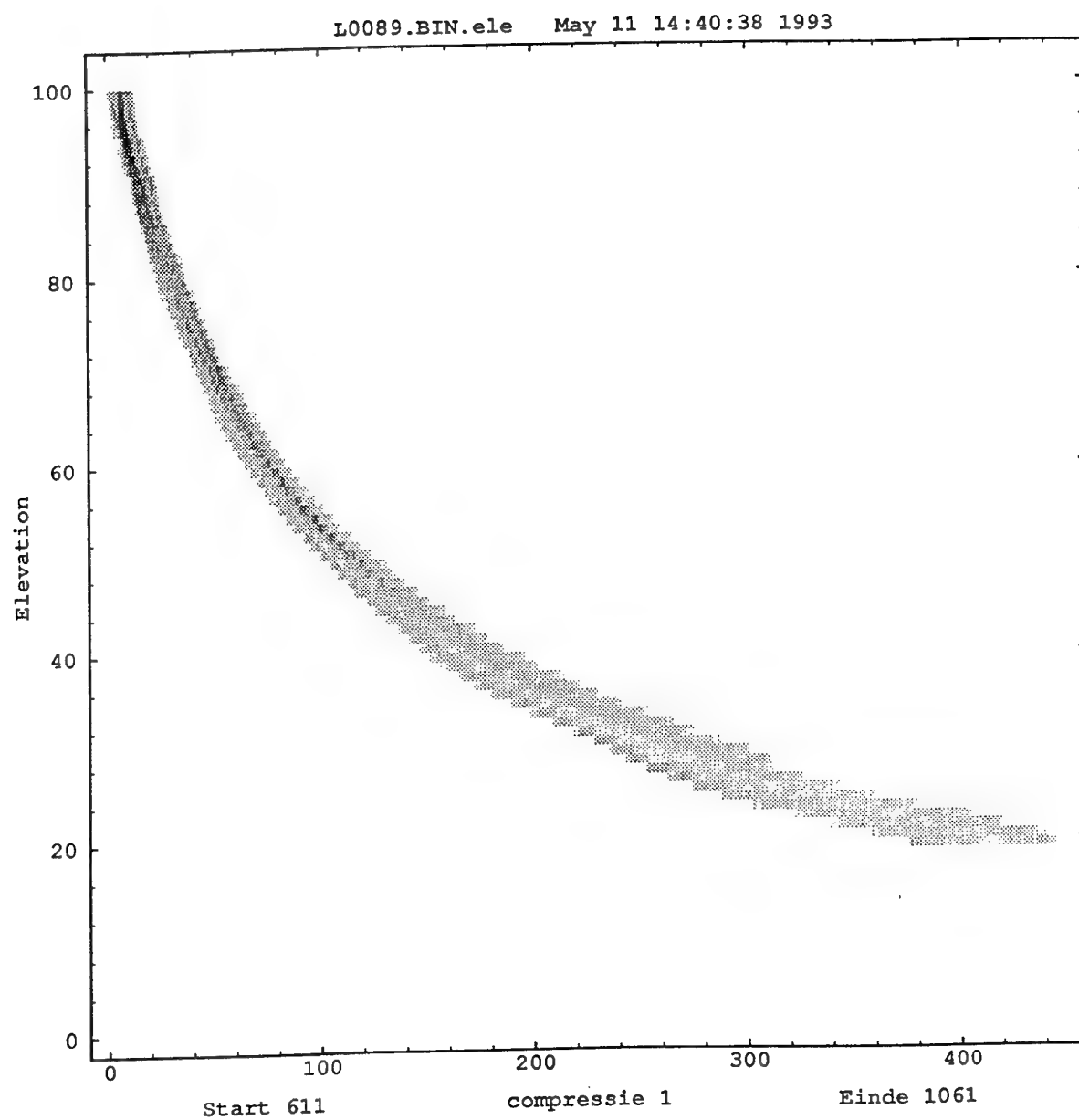
Figure A.8:   Radiance contribution of the non corrected image of figure A.5.

L0089.BIN.ele   May 11 14:40:38 1993

Start 611   compressie 1   Einde 1066
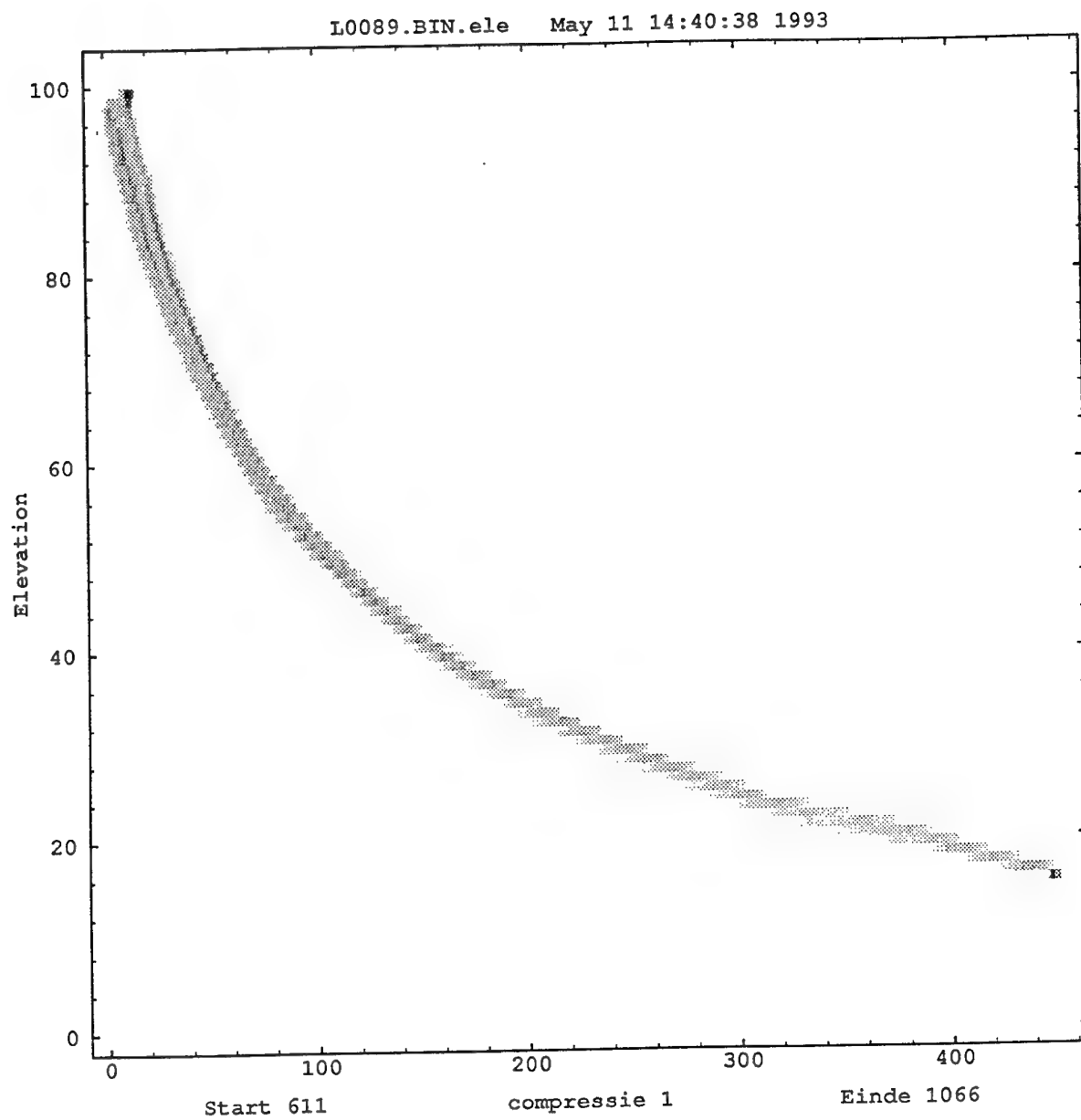
Figure A.9:   Radiance contribution of the corrected image of figure A.7.
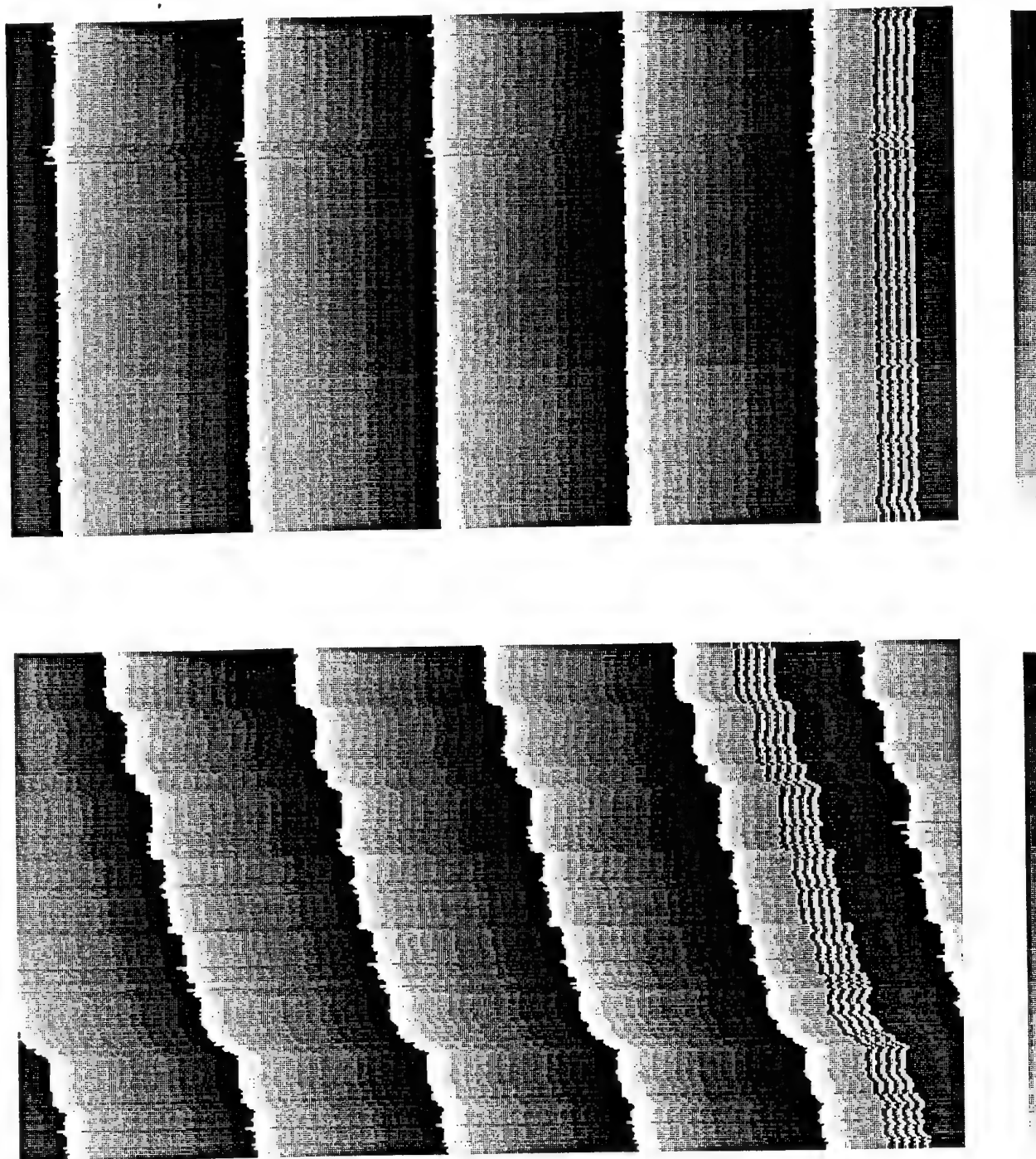
Figure A.10:   Top image: Image without horizontal shifts. Bottom image: Image with horizontal shifts.

CALIBRATION

The calibration of the system is performed by using the Electro Optical Industries P14000 differential temperature source available at TNO-FEL. This system consists of a centre plate which can be cooled or heated and two side plates which are at ambient temperature. The system is positioned at 10 m from the cloud scanner. The transmission is better dan 0.999 % for this very short path. The centre plate is set at +5°C. The temperature of the outside plates is measured in the left plate (front sight). An image is obtained by the cloud scanner and the part with the source is selected. The plates are 25x25 pixels. An area of 10 to 16 pixels in the vertical and in horizontal direction is selected. The average value and the standard deviation σ of this area are calculated. The results of this measurement are in table B.1 for 2 March 1993 and in table B.2 for 29 November 1993.

Figure B.1 shows the measurements. The temperature in March was lower than in November so the points can be divided in two pairs. The open circles are the outside plate in March the filled circles are the centre plate measurements in March the open diamonds are the outside plate values in November and the filled diamonds are the centre plate in November. Two of these sets are indicated with a dotted line. The difference between the outer plate and the centre plate is controlled by the system and should be the most accurate. When comparing these values this results in bit differences between 50.4 and 52.9 in March and between 40.8 and 46.7 in November. The difference is too large to be caused only by noise. Also there is a correlation between the temperature and the response of the system. The response of the cloud scanner or the differential temperature source is not linear.

The cloud scanner clamps its signal each rotation at the reference bar to correct for the dark current of the detector. For the absolute sensitivity the temperature of the bar is measured with a Pt-100 resistor and added to the signal. The value which is added is linear in temperature instead of the radiance and is set on 5 mV/K. The response of the system is between 2.5 and 3.2 mV/K. This can be determinated with:

$$\frac{\frac{\Delta(LSB)}{ADCgain}\frac{10(V)}{4096(LSB)}}{T_{dif}(K)} = r(\frac{V}{K})$$

With Δ the difference in bits, T_{dif} the used temperature difference, $ADCgain$ the used gain and r the response of the system. This mismatch in response of the detector and the Pt-100 will result in an offset that changes with the temperature of the reference bar. This results in an offset which changes with the ambient temperature. The mismatch between the two calibration sets in figure B.1 is probably caused by this changing offset. When not in operation the system is held at a temperature of 10°C. There is a large reservoir of anti-freeze so temperature changes are relatively slow. The measurements on 2 March are done in two hours. The measurements on 29 November are done in

six hours. The measurements on 29 November are more likely to be hampered by this changing offset due to the longer duration. When only looking to the response of the centre plate (or the left plate) in figure B.1 the response is 4.6 mV/K (5.2 mV/K for the left plate). The grey curves in figure B.1 are the fits through the six data points. The changing offset can result in a 20 LSB lower value for a ambient temperature of 0 °C and a 20 LSB higher value for a ambient temperature of 20 °C. Corrections for the difference in radiance response and temperature response are minor compared to this temperature dependent offset.

The offset can be calculated if the clamp value is known. This is done by calculating the average of $4_v x 12_h$ pixels at line 1000 at pixel position 12. This value is stored in the image header. Figure B.2 is a crosscut of the bar in the azimuthal direction. The flat top indicates the bar. The centre of the bar is at pixel position 256. The influence of the bar is about 200 pixels broader. This can be seen by the decreasing bit value. It is important that the image is not shifted (see appendix A.10). A shift of more than 50 pixel will result in a wrong bit value. Also a crosscut is made of the radiance values of the bar in the elevation direction. Figure B.3 shows this crosscut. The pattern is typical for all crosscuts in the elevation direction. Starting with average + 5 values slowly decreasing to average - 5 and then again rising to average + 5.

Measurement	Time	Outside			Inside			Difference
	MET	°C	avg.	σ	°C	avg.	σ	LSB
a	11:51	5.7	911.3	2.0	10.7	964.2	2.7	52.9
b	11:59	5.8	917.2	1.7	10.8	969.8	1.8	52.6
c	12:07	5.9	919.6	1.8	10.9	972.5	1.8	52.9
d	12:18	5.9	917.3	1.9	10.9	970.2	2.1	52.9
e	12:47	6.8	925.9	1.7	11.8	977.4	2.0	51.5
f	13:00	7.3	934.1	1.9	12.3	985.5	2.2	51.4
g	13:18	7.4	939.8	1.8	12.4	990.2	1.7	50.4
h	13:34	7.7	937.3	1.9	12.7	987.9	2.0	50.6

Table B.1:   Calibration measurements made at 2-March-1993 using absolute range and a gain of 8 times.

The response of the relative signal is measured in three ways:

- Using the EOI differential temperature source.

- Making an image using the absolute and a relative signal and compare several regions in the images.

- Using two sources with a temperature of the ambient + 5 °C and +10 °C.

Measurement	Time	Outside			Inside			Difference
	MET	$^\circ C$	avg.	σ	$^\circ C$	avg.	σ	LSB
a	10:25	8.7	942.0	2.2	13.7	988.7	2.5	46.7
b	10:57	8.7	937.1	1.6	13.7	981.3	1.9	44.2
c	11:32	9.4	947.1	2.1	14.4	991.8	1.9	44.7
d	12:49	10.4	969.2	1.8	15.4	1011.2	1.9	42.0
e	14:16	11.0	982.0	2.2	16.0	1022.8	2.3	40.8
f	16:01	10.7	972.0	2.1	15.7	1016.9	2.5	44.9

Table B.2:   Calibration measurements made at 29-November-1993 using absolute range and a gain of 8 times.
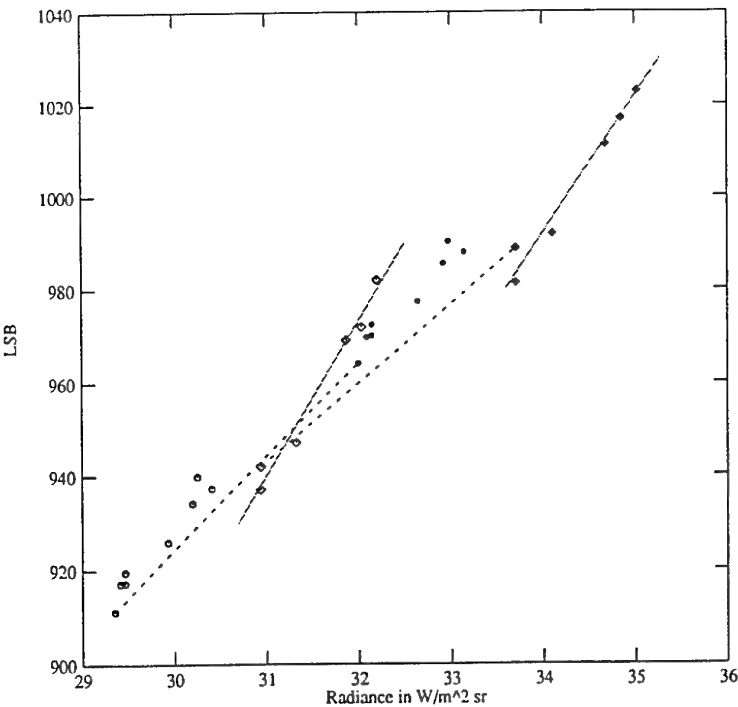
Figure B.1:   Calibration measurements done at 2 March (circles) and 29 November 1993 (diamonds). The open symbols are the outside plate. Which has the ambient temperature. The filled symbols are the centre plate with a temperature of ambient + $5K$.
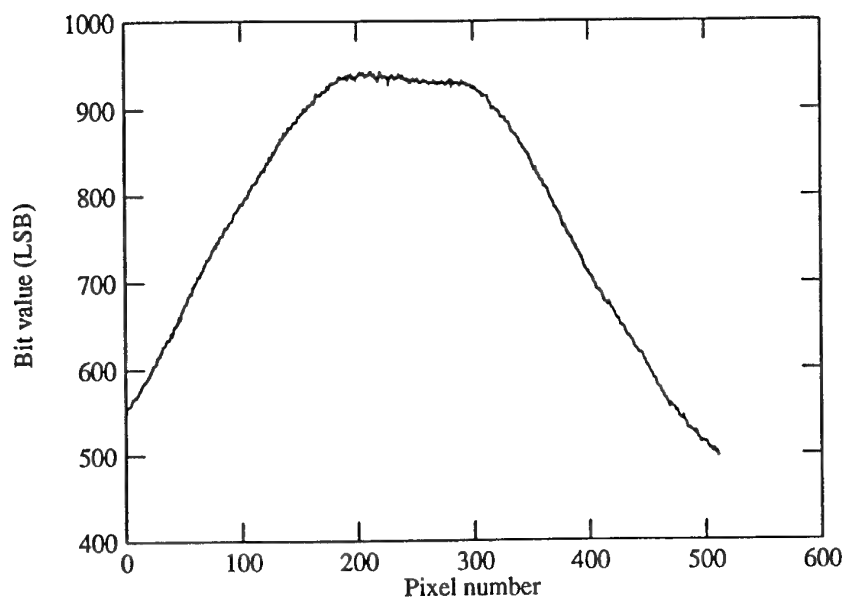
Figure B.2:   A crosscut of the bar in azimuthal direction. The flat top in the curve is the bar. The centre of the bar is positioned at pixel position 256.
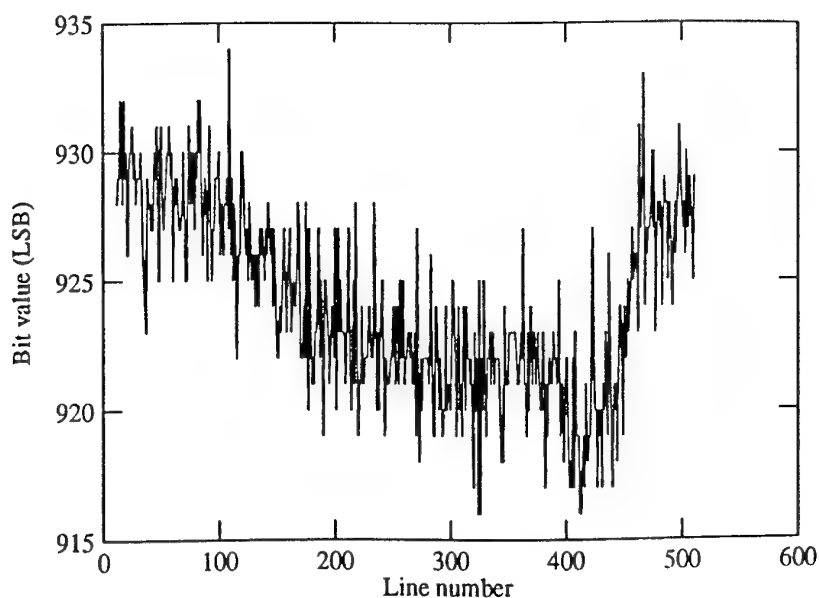
Figure B.3:   A crosscut of the bar in the elevation direction.

This results in a amplification of 13 ± 1 instead of 10. The clamp value is correctly set at $-0.5V$. This is a value of 1250 ± 10 using the gain of 4 of the ADC and should be 1228.

SOFTWARE

C.1 Introduction

Several software packages are developed for analyzing the cloud scanner images. This appendix briefly describes the most important programs and their use. The descriptions contain the name of the program, a description of its use and the syntax. Most programs have a range of options to control the program. The operation of the program in a batch is easy this way. All non-necessary options are placed in brackets. # indicates a number. Important information of images is stored in a header. This header is present in the first 100 bytes of each processed image. Table C.3 is a description of the header.

C.2 Software programs

Name: clouds

Description: Obtain a cloud scanner image using the 12 bits ADC of the masscomp. A section of the image is displayed using the IP-512 video board of the Masscomp.

Syntax: clouds gain filename channel azimuth elevation. The gain is 1, 2, 4 or 8. The channel is 0 or 1 and represents the channel number of the ADC. Azimuth and elevation give the section of the images that will be displayed on the monitor.

Remarks: Program cannot be recompiled on RTU 4.0 operating system. Propably a conflict between the ADC and the ethernet card.

Name: fastblok

Description: Display a cloud scanner image using a cartesian projection. The image is displayed using the IP-512 video board. The image can be larger than the dimensions of the IP-512 memory (512x512). The dimensions of the image and the dimensions of a cell of the image that will be displayed on the screen as one pixel are defined in the program. For other values the program should be recompiled. After loading the image a cursor appears. The position and the value of the pixel are shown on the computer monitor. The position is given in pixel

coordinates with respect to the image and with respect to the monitor. The displayed value is also the value of the image pixel and that of the monitor pixel. With 'z' it is possible to zoom the image and get an one to one display of the image. With 's' the image will be saved under `filename.bin`.

Syntax: `fastblok [-x #] [-y #] [-g] [-q] filename shift.`
Filename is a cloud scanner image. The program assumes an extension of .dat. The option –x and –y are used to zoom the image around pixel (x,y). Normally the image displays one pixel of a cell of the image. With the –g option the average of the cell is computed and this value is display in the image instead of the value of the lower left corner of the cell. The –q option saves the images and quits the program. This option is used to pick known parts of an image using a batch file.

Name: `readmeteo`

Description: Reads filename and generates a meteorological profile that can be used by `low7gen`. The program is also compiled to produce a generated profile based on groundlevel data. The programs `genmeteo`, `genmeteo2` and `genmeteo3` generate a profile based on the model 1,2 and 3 of chapter 5. The input file consists of start height (km), end height (km), increment (km), pressure, temperature, RH and the unit identification string as used by lowtran card 2C1. The program produces an output file `filename.pcc` and replaces the extension of the input file.

Syntax: `readmeteo filename.`

Name: `octa`

Description: Uses the `filename.rm2` and `filename.bin` files to compute the cloudiness. If meteorological data is present radiance predictions using lowtran are calculated. Three output files with data are produced. `psele.psg` contains the minimum and maximum radiance values in the image. The units are in LSB values and with line numbers. Also the radiance curves predicted by the models are stored in this file. `clut.psg` is the RMS' histogram of the whole image. The slope of the tail of the distribution is also stored in this file. `cloud.psg`

contains 10 sets of RMS' histograms with elevations. The image is divided in blocks of 50 lines (18°). To show the histograms in one plot a increasing offset is added for each block. An example of such a plot is 6.6. For each block the slope is computed and stored in the file. Besides these three output files also the main results as the cloudiness and slope are added to the log file cloud.log.

Syntax: octa [-v #] [-t #] [-p #] [-r #] [-s] [-h] [-c] [-x] filename
The first 4 options are used to set the visibility (v) in km, the temperature (t) in K, the pressure (p) in mbar and the relative humidity (r) in %. These options are only necessary to compute the three radiance models. If the header of the image contains the meteorological data this information is used. The program can produce three output images which show the intermediate results of this calculation for each pixel. A measured meteorological profile can also be used with the –x option. With this option the file meteo.def is also used as a atmospheric profile to calculate a radiance curve. The –s option can be used to save the following images: filename.ocb is the difference in pixel value with the minimum radiance curve, filename.oct is the RMS' image divide in classes and filename.ocb is the final image for cloudiness calculations. Black indicates sky and white indicates dense clouds. –h shows the help menu. –c overrules the default adapting of the minimum curve with the model 1 curve.

Name: anal

Description: Analyze a cloud scanner image. It calculates the mask position, blanks the image, computes the average of cells and the RMS' of this cells using both a static as a dynamic average. By default a cell of 4x12 is used. The resulting images are 500x467x12bits in size. Each image has a header with important information (see table C.3).

Syntax: anal [-f #] [-s] [-m #] [-l] [-L #] filename
The filename is the name without the .dat extension. A filename.rm2 with the RMS' calculation and filename.bin with the image data are generated. The –l option is used to add the data to the log file. The last log number is increased with one and used as a reference number for the images. The log number is also stored in the image header. –L with a number can be used to set the log number. The RMS' computation is only done if the –s option is used. The computation of the RMS' requires about two hours on the Masscomp. A fast check of the programs operation can be made by not using the –s option. The RMS' is calculated

for a 4x12 cell and stored as a 2 bytes number. The –f option set the multiplication factor for the RMS'. The NEI of the absolute sensitivity with a ADC gain of 8 times is 2 LSB. Without this multiplication factor two spikes in the RMS' histogram would occur. A multiplication factor of 25 is used for all images obtained with the absolute sensitivity range and a ADC gain of 8. More details in the histogram can be observed due to this multiplication. The cell has a dimension of 4x12 pixels. The maximum multiplication is 48 with higher multiplication factors discretisation would occur. The mask position is calculated by the program in only two cases the wrong position was calculated. To set the correct mask position the –m option is available.

Name: `manip`

Description: `manip` shows image datafiles using the masscomp IP-512 video board. Interactive operations on the images are possible by pressing certain keys. The image is shown on a one to one pixel base so the maximum size is 512x512 pixels. The program can load 5 images which can be shown rapidly after each other using < Shift > and 1, 2, 3, 4 or 5. A cursor is moved by the 2 (down), 8(up), 4(left) and 6(right). The position of the cursor and the value of the pixel are displayed on the computer monitor. A part of the image can be selected with the cursor. To do this press 'b' of block mode. Place the cursor at the first corner and press return. Place the cursor on the opposite corner and press again return. The coordinates of the rectangular block are shown on the computer monitor. The operations which can be performed on (a part of) an image are: multiplication, offset, logical shift, split odd and even lines and compute average, minimum, maximum and rms. The result can be saved. More images can be loaded with 'l' up to a maximum of five. A help screen appears when pressing '?'.

Syntax: `manip [filename.ext ..]`. Maximum 5 filenames can be specified at the command line. If no filename is specified than the program will ask for one.

Name: `pic2ele`

Description: Makes a 2 dimensional histogram. The program calculates a histogram for a set of lines. The number of occurrences is stored in a file with the extra extension .ele. This program

is attended to make elevation distributions. These files can be printed using `mathematica` on the `felfs`. Two programs `linmath` and `logmath` are available to make a linear (see figure 3.9) or a logarithmic (see figure 3.10) plot of the data.

Syntax: `pic2ele [-x #] [-y #] [-r #] [-s #] [-a] [-t] [-n] filename.ext` A set of options controls the dimensions of the resulting filename.ext.ele. −x is the interval between the histogram classes (default 2). −y is the number of lines used for one histogram line (default 5). When using this program on an 512x512x12 bits image this can result in a (512/5)x(4096/2)x16bits image. The range of the histogram can be adapted using the command line options. With −a the range is truncated to 80 and the interval between the classes is adapted. −s gives the starting value of the histogram and −r the total range. Two options can be used to correct the image. −t corrects for the tilt and −n for the 50 Hz component at high elevations. The reason for these corrections is descriped in appendix A.4.

Name: `low7gen`

Description: Interactive generation of TAPE5 files for lowtran and modtran. The following parameters can be set: model, path type, atmosphere, wave length range, RH, temperature, pressure, windspeed, radiance mode. For a slant path the heights and the temperature of the boundary layer can be given. Three options can generate a range of datasets. A start, an end and an increment value are given for the angle, the visibility and the range. The program generates the succeeding datasets. Parameters which cannot be set by the program can be changed in the LOWTRAN7.CFG file.

Syntax: `low7gen [-q] [-m] filename`. Filename is at the moment not used. The −q option directly generates a TAPE5 file without interactive operation of the program. This is used to make a TAPE5 file for other programs as `octa`. The −m option writes in all parts of the TAPE5 file the complete meteorological profile. The automatic reread option of lowtran does not work correctly in some cases.

Remarks: Two shell scripts exists. `low7inter filename` which allows interactive use of low7gen. After generating a TAPE5 file lowtran7 and the programs `low7parse` and `low7take` are run. `low7parse` and `low7take` filter TAPE6 for radiance output and produce a file `filename.1st` which contains the radiance with elevation. `low7shell` operates the same as `low7inter` without the interactive use of `low7gen`. It is possible to read an atmospheric profile. The program

reads the file METEO.DAT. The file starts with the number of layers and 2 numbers. This can be compared with card 2C of lowtran. If the first number is 1 also a card 2C2 description is expected. If the second number is 1 then a card 2C3 description is expected. In either case a card 2C1 description should be present. The different fields have the same interpretation as in lowtran but for this file it is not necessary to place the values in the correct column. Also the fields should be separated with a space.

C.3   Header

The file filehdr.h defines the first 100 bytes of an image. It contains information about the dimension of the image, the time the original cloud scanner image was made and what kind of image it is. Table C.3 gives a complete overview. The first two bytes are used as an identifier. The version number is used to expand the header. The version number indicates which parameters are set. All programs that use the loaddata.c subprogram can read this files and use the correct dimensions. The latest update of loaddata.c also reads DT-IMAGE files.

```c
#define MAGICNR              0Xabcd    /* magic number to identify the file */
#define VERSIE_NO_TIME       0         /* version of header */
#define VERSIE_NO_MULTY      1
#define VERSIE_NO_TREF       2
#define VERSIE_NO_METEO      3
#define VERSIONNR            4
#define NOTYPE               0         /* image type */
#define IMAGE                1
#define HISTOEL              2
#define HISTOAZ              3
#define ZOOM                 4
#define CORR                 5

#define COMP_NOISE           0x01      /* compensated for 50Hz signal */
#define COMP_TILT            0x02      /* tilt corrected */

typedef struct filehdr
{
short magic;                          /* magic number */
short version;                        /* version header */
short x;                              /* x dimension */
short y;
short z;
short b;                              /* bytes pro pixel */
short type;                           /* type of image */
short subtype;                        /* sub type */
char name[14];                        /* file name */
short mask;                           /* mask position (5600 range) */
char mult;                            /* multiplication value x direction or general */
time_t time;                          /* production time */
short x_zoom;                         /* start x zoom pixel */
short y_zoom;                         /* start y zoom line */
short lognr;                          /* log number */
char mult_y;                          /* multiplication value y direction */
short tref;                           /* reference value on bar */
short comp;                           /* computations */
float rh;                             /* relative hum. */
float mbar;                           /* pressure */
float temp;                           /* temperature */
float vis;                            /* visibility */
float wind;                           /* wind speed */
short wind_direct;                    /* wind direction */
char unused[26];
};
```

IMAGE DATA

D.1   Images data

In this appendix tables of analysed images are presented. The description of the various columns in the data table is as follows. The Log Number is the number used as reference for that images and all its processed images. The time is the local time when the original image was recorded. The mask position is the position of the mask in the images. This position is related to the orientation of the cloud scanner. The RMS' image are multiplicated with a factor too show more details. The used factor is in the "RMS mult".

Log Nr.	time	mask pos.	RMS mult
5	Nov 5 1992 14:35:57	684	10
6	Nov 10 1992 15:30:16	732	10
7	Nov 10 1992 15:30:16	732	1
8	Nov 16 1992 13:05:34	1908	10
9	Nov 16 1992 13:10:53	1884	10
10	Nov 10 1992 15:30:16	732	2
11	Nov 10 1992 15:30:16	732	3
12	Nov 10 1992 15:30:16	732	5
13	Nov 10 1992 15:30:16	732	20
14	Nov 10 1992 15:30:16	732	10
15	Nov 24 1992 14:47:12	0	10
16	Nov 24 1992 14:52:27	0	10
17	Nov 24 1992 15:42:20	636	10
18	Nov 24 1992 15:37:05	636	50
19	Nov 24 1992 14:52:27	0	50
20	Nov 27 1992 09:46:07	1836	25
21	Nov 30 1992 14:44:10	708	25
22	Dec 1 1992 10:53:47	1536	25
23	Nov 30 1992 14:44:10	708	25
24	Dec 2 1992 10:10:55	1860	25
25	Dec 1 1992 11:01:42	0	25
26	Dec 8 1992 09:53:57	1848	25
28	Jan 13 1993 14:38:09	4066	25
29	Jan 15 1993 10:12:39	1632	25
30	Jan 15 1993 14:37:37	1644	25
31	Jan 18 1993 16:04:58	528	25
32	Jan 21 1993 09:37:01	1812	25
33	Jan 21 1993 10:06:00	1788	25
34	Jan 21 1993 17:05:38	1740	25
36	Feb 15 1993 14:18:54	1836	25
37	Jan 21 1993 13:11:25	1812	25
38	Feb 23 1993 11:02:00	1620	25
50	Feb 24 1993 12:00:11	1464	25
51	Feb 23 1993 11:12:40	1620	25
52	Feb 23 1993 12:05:53	1356	25
53	Mar 2 1993 13:18:46	1140	25
54	Mar 2 1993 13:34:32	1140	25
55	Mar 2 1993 13:00:21	1140	25
56	Mar 3 1993 15:08:19	552	25
57	Mar 3 1993 17:05:31	372	25

Log Nr.	time	mask pos.	RMS mult
58	Mar 8 1993 14:09:36	816	25
59	Mar 8 1993 12:00:03	1392	25
60	Mar 10 1993 14:37:26	684	25
61	Mar 10 1993 15:16:10	684	25
62	Mar 12 1993 09:48:42	1956	25
63	Mar 12 1993 09:48:42	1956	25
64	Mar 23 1993 13:27:35	972	25
65	Mar 19 1993 11:29:55	1656	25
66	Mar 29 1993 08:30:35	2280	25
67	Mar 29 1993 08:51:53	2280	25
68	Mar 29 1993 14:57:25	768	25
69	Mar 30 1993 09:19:46	2088	25
70	Mar 30 1993 12:43:05	1092	25
71	Apr 14 1993 14:27:59	1080	25
72	Apr 15 1993 13:27:39	1260	25
73	Apr 16 1993 16:00:03	528	25
74	Apr 16 1993 15:44:39	528	25
75	Apr 20 1993 10:38:34	2136	25
76	Apr 20 1993 11:55:53	1716	25
80	Apr 20 1993 10:38:34	2136	25
81	Apr 20 1993 11:55:53	1716	25
82	Apr 23 1993 15:10:08	660	25
83	Apr 23 1993 15:15:18	660	25
84	Apr 28 1993 12:53:23	1452	25
85	Apr 28 1993 13:06:14	1452	25
86	May 4 1993 09:25:38	2376	25
87	May 4 1993 09:33:44	2376	25
88	May 11 1993 14:12:15	948	25
89	May 11 1993 14:40:38	792	25
90	May 12 1993 14:15:57	1032	25
91	May 12 1993 14:23:44	1032	25
92	Aug 13 1993 09:30:	2436	25
93	Aug 13 1993 11:10:28	1968	25
94	Aug 13 1993 13:14:44	1356	25
95	Aug 13 1993 15:15:51	660	25

Log Nr.	time	mask pos.	RMS mult
100	Aug 18 1993 09:43:47	2400	25
101	Aug 18 1993 10:49:12	2088	25
105	Sep 6 1993 13:14:12	1308	25
106	Sep 6 1993 15:34:17	576	25
107	Sep 6 1993 09:41:34	2232	25
108	Sep 7 1993 12:49:45	1476	25
109	Sep 6 1993 13:14:12	1308	25
110	Sep 22 1993 10:42:09	672	25
111	Sep 22 1993 12:00:49	1704	25
112	Oct 28 1993 15:41:00	756	25
113	Oct 28 1993 15:54:00	576	25
114	Oct 28 1993 17:11:00	300	25
115	Oct 29 1993 12:32:00	1440	25
116	Oct 29 1993 11:25:00	1680	25
117	Oct 29 1993 11:57:00	1560	25
118	Oct 29 1993 12:32:00	1440	25
119	Oct 29 1993 13:49:00	1032	25

D.2   Meteorological conditions of the measurements

The meteorological data related to the images listed in appendix D.1 are given below.

Log. Nr.	Pressure (mbar)	Visibility (km)	RH (%)	Temperature (K)
26	1010	1.5	99	278.9
31	1028	20	80	280
32	1024	16	86	281.1
33	1024	16	86	281.1
34	1020	16	79	283.9
36	1035	3	86	277.5
37	1023	15	84	282.8
38	1030	27	77	274.2
50	1033	0.5	98	272.3
52	1030	28	72	275.2
53	1012	7	68	277.2
54	1012	7	68	277.2
55	1012	7	68	277.2
56	1021	6	78	274.6
57	1022	7	85	274.2
58	1024	15	60	281.4
59	1025	12	72	279.7
60	1022	11	80	282.2
61	1022	11	80	282.2
63	1022	2.3	87	281.7
64	1022	25	77	281.5
65	1022	17	86	280.2
66	1022	15	68	275.7
67	1022	15	68	275.6
68	1021	20	38	281.9
69	1021	20	62	278.9
70	1020	20	37	284.5
71	1010	5	83	284.9
72	1017	6	92	283.7
73	1021	10	66	286.4
74	1021	10	66	286.4

Log Nr.	Pressure (mbar)	Visibility (km)	RH (%)	Temperature (K)
80	1014	10	89	287.2
81	1014	11	79	289.7
82	1008	17	71	290.2
83	1008	17	71	290.2
84	1015	10	60	296.2
85	1015	10	60	296.2
86	1033	20	80	281.2
87	1033	20	80	281.2
88	1014	12	57	295.6
89	1014	12	57	295.6
90	1007	12	48	296.8
91	1007	12	48	296.8
92	1009	10	95	287.2
93	1011	13	94	288.7
94	1012	11	85	288.2
95	1013	12	76	288.7
100	1015	10	94	287.9
101	1015	10	93	288.1
106	1017	21	66	290.7
107	1019	20	83	285.2
108	1011	14	65	291.2
109	1018	20	70	290.2
110	1013	7	88	289
111	1013	7	83	289.9
112	1027	15	77	282.4
113	1027	15	77	282.4
114	1027	12	79	282.2
115	1031	18	90	282.7
120	1031	18	90	283.1
121	1031	18	90	283.2
122	1031	18	90	283.5
123	1031	15	83	284
125	1031	15	83	284

REPORT DOCUMENTATION PAGE
(MOD-NL)

1. DEFENCE REPORT NO. (MOD-NL)	2. RECIPIENT'S ACCESSION NO.	3. PERFORMING ORGANIZATION REPORT NO.
TD94-0886		FEL-94-A094

4. PROJECT/TASK/WORK UNIT NO.	5. CONTRACT NO.	6. REPORT DATE
20401	A87KM174	October 1994

7. NUMBER OF PAGES	8. NUMBER OF REFERENCES	9. TYPE OF REPORT AND DATES COVERED
105 (incl. 4 appendices, excl. RDP & distribution list)	6	Interim report

10. TITLE AND SUBTITLE

Longterm Infrared Cloud Clutter Research

11. AUTHOR(S)

A.C. Kruseman

12. PERFORMING ORGANIZATION NAME(S) AND ADDRESS(ES)

TNO Physics and Electronics Laboratory, P.O. Box 96864, 2509 JG The Hague, The Netherlands
Oude Waalsdorperweg 63, The Hague, The Netherlands

13. SPONSORING AGENCY NAME(S) AND ADDRESS(ES)

Royal Netherlands Marine, DMKM/WCS/EMDC

14. SUPPLEMENTARY NOTES

The classification designation Ongerubriceerd is equivalent to Unclassified.

15. ABSTRACT (MAXIMUM 200 WORDS (1044 BYTE))

An infrared all-sky mapper Scorpio has been developed at TNO-FEL. The system has been used to obtain 10 μm sky and cloud backgrounds for about one year. The data cover an area of -18° up to +72° in elevation and 340° in azimuth with a spatial resolution of 0.8 mrad. The system has an absolute calibration. Data recording with 12 bit resolution, and image analysis are done with a MASSCOMP computer. The image processing is done in several steps. Non-sky areas in the images are blanked. Clutter calculations are performed in cells of 4x12 pixels, with local RMS as a basis. The use of a moving average in the RMS calculations diminishes the content of high clutter values. Clutter and radiance distributions are studied with elevation. Lowtran 7 calculations are performed with a model based cloud structure. These are compared with real Scorpio measurements and show good agreement. The results are discussed for a measured atmospheric height profile as well as for assumed model height profiles, based on ground level data. Scorpio images of a single day have been analysed in much detail. Clutter slope calculations show that it is an important measure for the clutter content of the sky images. An algorithm for cloudiness calculations is discussed. The detection of point targets is discussed.

16. DESCRIPTORS	IDENTIFIERS
Infrared radiation	Cloud clutter
Sky radiation	Infrared search & track

17a. SECURITY CLASSIFICATION (OF REPORT)	17b. SECURITY CLASSIFICATION (OF PAGE)	17c. SECURITY CLASSIFICATION (OF ABSTRACT)
Ongerubriceerd	Ongerubriceerd	Ongerubriceerd

18. DISTRIBUTION AVAILABILITY STATEMENT	17d. SECURITY CLASSIFICATION (OF TITLES)
Unlimited Distribution	Ongerubriceerd